CATALYTIC MEMBRANE REACTOR FOR EXTRACTION OF HYDROGEN FROM BIOETHANOL REFORMING

A Dissertation

by

BHANU VARDHAN REDDY KUNCHARAM

Submitted to the Office of Graduate and Professional Studies of
Texas A&M University
in partial fulfillment of the requirements for the degree of

DOCTOR OF PHILOSOPHY

Chair of Committee,	Benjamin A. Wilhite
Committee Members,	Mark Holtzapple
	Perla Balbuena
	Jaime Grunlan
Head of Department,	M. Nazmul Karim

December 2013

Major Subject: Chemical Engineering

ABSTRACT

This research explores a novel application of catalytic membrane reactors for high-purity hydrogen extraction from bioethanol reforming. Conventional membrane systems employ hydrogen permselective materials such as palladium, polymer membranes, which present several material challenges including embrittlement, thermal degradation and poisoning by hydrocarbons when used for high-temperature hydrocarbon reforming. Thus, the present work is motivated by an interest in employing reactor design concepts to alleviate our reliance upon permselective materials. Catalytic membrane reactor with segregated reactant(s) is employed to demonstrate the hypothesis that high-purity hydrogen with competitive hydrogen recoveries can be achieved by manipulating the reaction and diffusion phenomena, and corresponding thermal gradients inside the catalytic membrane, in the absence of any permselective materials. The hypothesis is demonstrated in two designs: (1) a single functional layer design for water-gas-shift catalytic membrane reactor, and (2) a multi-layer design for bioethanol reforming. A two-dimensional model is developed to describe reaction and diffusion in the catalytic membrane coupled with plug-flow equations in the retentate and permeate volumes using shell and tube architecture. Simulation results for a typical diesel reformate mixture (9 mol% CO, 3 mol%CO_2, 28 mol% H_2 and 15 mol% H_2O) demonstrate that H_2:CO permselectivities of 90:1 to > 200:1 with permeate hydrogen recoveries of 20% to 40% can be achieved through appropriate catalytic membrane design. This single reaction simulation results are used to establish a clear rubric of design rules that are then used as a base for designing catalytic membrane reactor for extraction of hydrogen from bioethanol (16 mol% ethanol). The two-dimensional catalytic membrane reactor for bioethanol reforming is simulated, using a network of ethanol reforming reactions and a composite catalyst with unique catalytic

layers active for one or more reactions. The isothermal simulation results show that an apparent H_2:CO permselectivity of 100:1 with hydrogen recovery of 15% can be achieved at appropriate design and flow configuration. This model is extended to a non-isothermal design, which predicted a decrease in membrane performance owing to endothermic reforming reaction. An autothermal design with an additional combustion catalyst layer to counteract the endothermic thermal gradients enhanced the non-isothermal membrane performance. Experiments were conducted to validate the water-gas-shift catalytic membrane reactor model using a gas permeation system; results qualitatively agree with the modeling results and quantitively with an error. In conclusion, this research demonstrates the hypothesis that reaction-diffusion, thermal gradients within the catalyst can be manipulated to achieve selective removal of hydrogen bioethanol reforming without employing any expensive permselective materials. This also provides a new direction for designing permselective membranes for overcoming corrosion by removing the undesired gases using catalyst coating employing the design rules presented.

To my family

ACKNOWLEDGMENTS

I am grateful to my advisor Dr. Benjamin A. Wilhite for his constant support and motivation during the course of this research. Dr. Wilhite has been patient throughout the course of my Ph.D., without his encouragement, guidance and funding this thesis would not have been possible. I would also like to thank him for sharing his experiences and providing me with inspiration. I look forward to continuing a friendly relationship with him for years to come.

It is with great pleasure, I would like to thank Dr. Mark Holtzapple, Dr. Perla Balbuena and Dr. Jaime Grunlan for their precious time spent on reviewing my thesis and serving on thesis committee. I would like to thank Dr. Holtzapple for patiently reviewing my preliminary presentation, which I believe tremendously improved my writing/presentation skills.

I am very grateful to work in Dr. Wilhite research group and was able to meet wonderful people during the course of my Ph.D. I would like to acknowledge Dr. Daejin Kim for his friendship and providing training and guidance for conducting experiments. I would like to thank Shalini Dhamodharan for her friendship and patiently listening to my complaints.

I would like to thank other Dr. Wilhite group members for supporting during the course of my Ph.D.: Dr. Angela Moreno, Dr. Aravind Suresh, Haomaio Zhang, Elva Lugo, Xiahong Cui, Holly Butcher, Srikanth PVK, Greg Honda and Christine Duval. I am thankful to Holly for proof reading my thesis.

I would also like to thank professors at UCONN, Dr. William Mustain, Dr. Jeffrey McCutcheon and Dr. Ranjan Srivastava for support during initial phase of my Ph.D.

I would also like to thank Leah Winterberger and Susan Soucy at UCONN; Towanna

Arnold and Selina Garcia at TAMU for their support with paperwork and purchasing. I would also like to acknowledge Louis Muniz Jr., Randy Marek for technical support with experiments; Jeff Polasek and Joel James for their computer support.

I would like to thank staff at TAMU writing center, thesis office for helping me with writing my thesis. I gratefully acknowledge the following open source softwares used in preparation of this thesis document: MacTeX, LyX, Gimp and Inkscape.

I am very thankful to my friends who provided me with moral support, especially Sundeep Mora who inspired me to pursue graduate studies. I also want to thank my friends, Mahipal Reddy, Prashant Reddy, Sreekanth Reddy, Harsha Mallipelli, Dharma Maddala and Kartheek Reddy.

Finally, none of this would have been possible if it wasn't for support and patience of my family. I would like to dedicate my thesis to my family for their unconditional love.

TABLE OF CONTENTS

LIST OF FIGURES

LIST OF TABLES

1. INTRODUCTION

Hydrogen is a colorless, odorless and tasteless non-metallic, non-toxic, highly combustible diatomic gas, available abundantly in the universe about 75% on baryonic mass [Armaroli and Balzani, 2011; Mazloomi and Gomes, 2012]. Hydrogen remains a critically important commodity chemical in the chemical and petroleum industries [Ramachandran, 1998; Baade *et al.*, 2001], with primary uses ranging from ammonia production, petrochemical industry, oil and fat hydrogenation, metallurgical applications, alcohol synthesis, pharmaceuticals and the electronics industry. Recent renewal of interest in hydrogen production and purification technology has been driven by interest in clean, more sustainable chemical processing, fuels production and energy technologies [Dutta, 2013; Sherif *et al.*, 2005; Holladay *et al.*, 2009].

1.1 Industrial uses of hydrogen

Hydrogen has historically been an important commodity chemical in various industries, the ammonia industry being the largest consumer, followed by petroleum refining, metallurgical processing and the food industry. Figure 1.1 presents a breakdown of hydrogen consumption by industry. A detailed review of hydrogen usage and requirements by each industry is presented below.

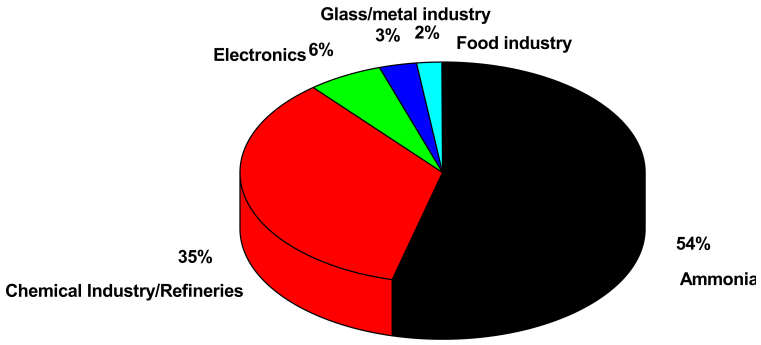

Figure 1.1: The percentages of global hydrogen consumption by industrial sector [Chaubey *et al.*, 2013; Armaroli and Balzani, 2011; Lan *et al.*, 2012].

1.1.1 Petroleum industry and petrochemical processing

Hydrogen is an indispensable utility in the petroleum refining industry, which accounts for approximately 35% of global hydrogen consumption [Lakeman and Browning, 2001; Ramachandran, 1998; Armaroli and Balzani, 2011; Chaubey *et al.*, 2013]. The demand for hydrogen in the petroleum industry has been steadily increasing because of stricter legislation for sulfur content in gasoline and diesel fuels for environmental protection, requiring more hydrotreating units. In the past decade crude oil has been getting heavier, prompting refineries to use an increasing number of hydroprocessing units [Hallale and Liu, 2001; Courty and Chauvel, 1996; Alves and Towler, 2002; Liao *et al.*, 2010; Liu and Zhang, 2004]. The growing hydrogen demand at the refinery presents several challenges to hydrogen production, purification, distribution and management to ensure an optimal plant economics [Mapiour *et al.*, 2009; Hallale and Liu, 2001; Hallale *et al.*, 2002; Alves and Towler, 2002]. Hydrogen is primarily used in petroleum processing in two ways: hydrotreating and hydrocracking.

1.1.1.1 Hydrotreating

Hydrotreating is a common unit process in petroleum refineries for removing sulfur, oxygen and nitrogen as well as metal impurities from crude oil streams (Table 1.1). Sulfur is the most abundant heteroatom impurity in crude oil, and its content as high as 2–5 wt% for 'sour' crudes or as low as 0.1 wt% for 'sweet' crudes [Topsoe *et al.*, 1996; Hsu and Robinson, 2006]. The low-boiling naptha fraction contains sulfur mainly in the form of thiols, sulfides, disulfides and thiophenes. Kerosene and gas oil middle distillate fractions predominantly contain thiophenic compounds containing benzo-and dibenzothiophene structures [Topsoe *et al.*, 1996]. The sulfur present in crude oil is removed via hydrodesulfurization process, in which hydrogenolysis reaction cleaves the C-S chemical bond to form H_2S. The by-product H_2S is subsequently converted to elemental sulfur for disposal via Claus process ($2H_2S+O_2 \longrightarrow S_2+2H_2O$). Crude oils also contain up to 0.1 wt% of nitrogen, which is removed as ammonia in a hydrodenitrogenation unit. The oxygen content in petroleum crudes is typically less than 0.1 wt%, which may be removed as water via hydrodeoxygenation. The most commonly used commercial catalysts for hydroprocessing reactions are sulfided nickel-molybednum and cobalt-molybednum supported on γ-alumina [Mapiour *et al.*, 2009].

Table 1.1: Summary of hydroprocessing reactions and their chemistry [Hsu and Robinson, 2006].

Reaction type	Chemistry
Hydrodesulfurization (HDS)	$R\text{-}S\text{-}R' + 2H_2 \longrightarrow RH + R'H + H_2S$
Hydrodenitrogenation (HDN)	$R{=}N\text{-}R' + 3H_2 \longrightarrow RH + R'H + 2NH_3$
Hydrogedeoxygenation (HDO)	$R\text{-}O\text{-}R' + 2H_2 \longrightarrow RH + R'H + H_2O$
Hydrodematallation (HDM)	$R\text{-}M + 1/2H_2 + A \longrightarrow RH + M\text{-}A$

R = alkyl group; M = Metal (Fe, Ni or V); A = Metal adsorbing material

The hydrogen purity is an important factor affecting the conversion in hydrotreating units. The presence of excessive light gas impurities (e.g., CH_4, CO) reduce hydrogen partial pressure and therefore reaction rates resulting in a decreased conversion. The decreased hydrogen partial pressure may be offset either by operating at a higher total pressure or employing a large makeup hydrogen to the process [Mapiour *et al.*, 2009; Ramachandran, 1998; Scherzer and Gruia, 1996]. However, both of these options present practical problems: operating at higher pressure than design limitation can lead to equipment failure, while using large makeup hydrogen greatly increases the operating costs.

1.1.1.2 Hydrocracking

Hydrocracking is one of the oldest hydrocarbon conversion processes, originally developed for cracking heavy oils and coal tars to liquid fuels in Germany between 1910 and 1945. Coal conversion to liquid fuels was a catalytic process operating at high temperatures (371 to 538 °C) and high pressures (207 to 690 bar) [Hsu and Robinson, 2006]. The modern hydrocracking process was invented by Chevron in 1959 and the first licensed unit was started in 1962 in United States. A two-stage isocracking plant was commissioned in 1966 in Richmond, California for upgrading vacuum gas oil to naptha and jet fuel [Hsu and Robinson, 2006; Wade *et al.*, 2009]. At the same time, a single-stage once-through unit was established to hydrocrack deasphalted oil [Hsu and Robinson, 2006; Wade *et al.*, 2009]. The cost of hydrogen production and purification accounts for 84% of the total operating cost in a typical hydrocracking unit [Long *et al.*, 2011].

Hydrocracking is a two-step process involving catalytic cracking followed by hydrogenation, thus converting higher boiling range hydrocarbons into more valuable low-boiling products such as gasoline, diesel and jet fuel [Mohanty *et al.*, 1990; Topsoe *et al.*, 1996; Hsu and Robinson, 2006]. Hydrocracking reaction involves the scission of C-C bonds to produce lower boiling products [Topsoe *et al.*, 1996]. Hydrocracking can process

a wide range of feedstocks, from naphthas to deasphalted vacuum residue [Mohanty *et al.*, 1990; Weitkamp, 2012]. It is mainly used for feedstocks that are difficult to process using catalytic cracking [Speight, 2010]. It can also be used to upgrade petrochemical feedstocks, improve gasoline octane number and produce high quality lubricants [Mohanty *et al.*, 1990].

The most commonly used design configuration is a single-stage system (shown schematically in Figure 1.2), with an amorphous oxide based catalyst employed for the production of middle distillate [Ward, 1993; Speight, 2010; Scherzer and Gruia, 1996]. In this configuration, the first reactor contains a high-activity hydrotreating catalyst and hydrocracking units with desired catalyst are followed. The main advantage of this configuration is that the hydrotreating effectively removes the organic sulfur and nitrogen compounds in the feedstock which are poison for hydrocracking catalysts.

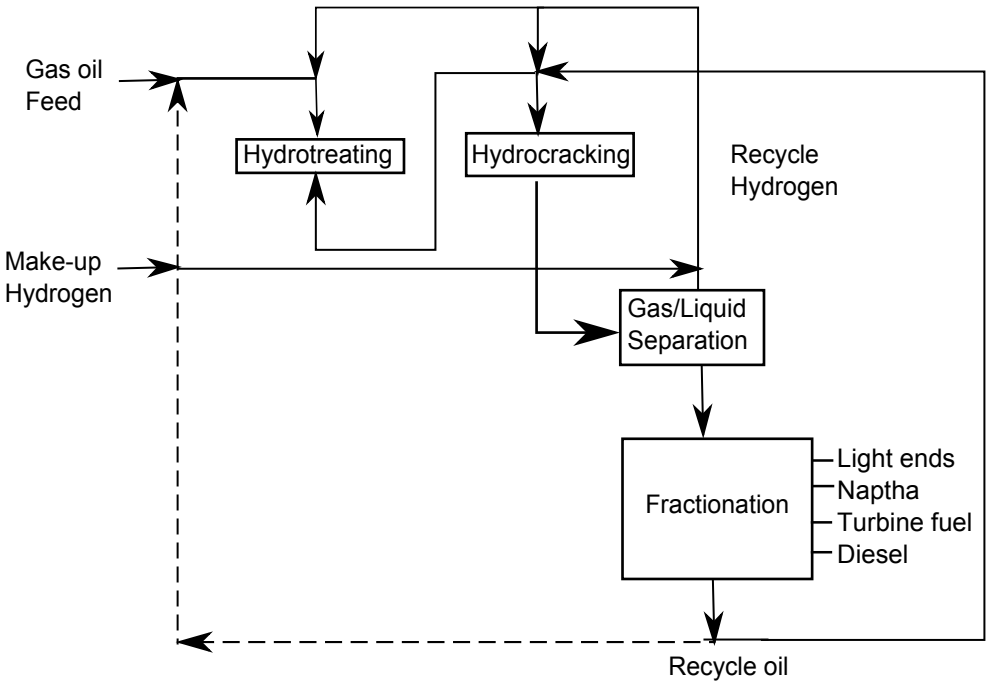

Figure 1.2: Flow chart of single-stage unicracking process [Ward, 1993].

Hydrocracking requires a hydrogen purity of about 70 to 80% with a minimal amount of CO and CO_2 [Shao *et al.*, 2009]. The CO is considered to be the worst impurity, because it can accumulate in the hydrocracking unit owing to its limited solubility in hydrocarbons and water. The presence of CO and CO_2 adversely affects hydrocracking in two manners; i) by decreasing hydrogen partial pressure and thus driving force for reaction, and ii) competitive chemisorption of CO on catalyst sites, reducing the number of sites available for reaction. The latter phenomena increases the risk of catalyst deactivation from coking. The CO and CO_2 in the hydrogen converts to methane and water on the active sites of hydrocracking catalyst. This methanation reaction of CO and CO_2 competes with the normal hydrocarbon reactions for active sites of the catalyst, prompting for higher catalyst temperatures to compensate for the decreased hydrocarbon conversion [Hsu and Robinson, 2006]. The decrease in hydrogen partial pressure also negatively affects the overall and saturation of aromatics yields. The decrease in hydrogen partial pressure and surface coverage can be improved in two ways, either by using makeup hydrogen or operating at higher system pressure; however, both result in higher operating costs. Thus, high-purity hydrogen purification is a challenge for overall optimal economics of a petroleum processing plant.

1.1.2 Ammonia industry

Ammonia has remained the backbone of the chemical industry for over a century, owing to its use in fertilizer, munition and fine chemical products. Fritz Haber was awarded the Nobel prize in 1920 for ammonia (NH_3) synthesis from its constituent elements (N_2 and H_2) [Haber, 2002; Erisman *et al.*, 2008]. Carl Bosch received the Nobel prize in 1930 for subsequently developing ammonia synthesis at an industrial scale [Erisman *et al.*, 2008]. The catalytic "Haber-Bosch" synthesis process is carried out at pressures of 200 to 350 bar and temperatures of 300 to 500 °C. The overall chemical reaction for ammonia

production is given by:

$$N_2(g) + 3H_2(g) \longleftrightarrow 2NH_3(g) \;\; \triangle H = -92\,\text{kJ}\,\text{mol}^{-1} \tag{1.1}$$

The catalysts used before 1950 were primarily iron oxide (Fe_3O_4) based with Al_2O_3, CaO and K_2O as promoters; modern catalysts are mainly promoted using natural magnites and potash (with low impurities) [Lloyd, 2011b]. The ammonia synthesis catalyst must be reduced prior to use at a pressure of 70 to 100 bar [Lloyd, 2011b]; this promotes absorption of molecular nitrogen, which in turn weakens the N-N bond prior to reaction with hydrogen. Thus, catalyst activity is sensitive to hydrogen partial pressure, with oxidizing impurities reducing activity and competitive adsorption of CO inhibiting reaction rates.

At present, ammonia manufacturing consumes about 54% of global hydrogen production and is a primary consumer in the chemical industry [Forsberg, 2007; Ramachandran, 1998; Funk and Reinstrom, 1966]. Ammonia is mainly used in manufacturing of fertilizers and therefore hydrogen consumption is expected to grow steadily, given the constant rise in world population [Ball *et al.*, 2005]. Ammonia also finds use in manufacturing explosives for mining and munition industries [Erisman *et al.*, 2008]. The low cost of ammonia shipping favors a very large ammonia production plant, thus a large demand for inexpensive hydrogen [Forsberg, 2007]. An ammonia plant is therefore usually located where an abundance of inexpensive hydrogen can be produced, i.e., where inexpensive natural gas is available.

1.1.3 Metallurgical processing

1.1.3.1 Nickel and Copper processing

Hydrogen is used in the wet reduction process wherein copper, nickel and cobalt are precipitated from a salt solution. This process is known as the Sherritt Gordon process, first used in Sherritt Gordon mines Limited in Canada. The pressure leaching technology has

been used since 1960s for recovering copper and nickel in sulfide concentrates. Hydrogen is used in the reduction stage to remove sulfate present in the solution and precipitate nickel and copper [Habashi, 2009; Ramachandran, 1998]. The Sherrit-Gordon process reaction for copper is as follows:

$$CuFeS_2 + \frac{3}{2}O_2 + 2H^+ \longrightarrow Cu^{2+} + FeOOH + 2S + H_2O \tag{1.2}$$

1.1.3.2 Iron ore processing

In the direct reduction of iron (DRI) process the iron ores are reduced to iron using synthesis gas (syngas) made from natural gas [Forsberg, 2007]. Hydrogen potentially has a significant market in iron production. However, for the DRI process to replace other processes low-cost hydrogen should be available near the iron ore source site [Forsberg, 2007]. The major chemical reactions involved in DRI process can be summarized as follows [Forsberg, 2007]:

$$Fe_3O_4 + CO \longrightarrow 3FeO + CO_2 \tag{1.3a}$$

$$Fe_3O_4 + H_2 \longrightarrow 3FeO + H_2O \tag{1.3b}$$

$$FeO + CO \longrightarrow Fe + CO_2 \tag{1.3c}$$

$$FeO + H_2 \longrightarrow Fe + H_2O \tag{1.3d}$$

It is evident from the above discussion that cheap, high-purity hydrogen has significant market in petroleum refineries, ammonia industry and metallurgical processing. Recently

significant interest in high-purity hydrogen has been due to its use as a fuel in alternative energy technology i.e., fuel cells. The following sections detail the hydrogen use in various fuel cell technologies.

1.2 Hydrogen as an alternative energy

Hydrogen is considered an ideal choice for generating clean, efficient and sustainable energy. Hydrogen has the highest energy density per kilogram relative to any other fuel, and when used in a fuel cell can be converted directly to electric energy. A comparison of energy density of various fuels is presented in Table 1.2 [Moreno, 2010].

Table 1.2: Summary of energy density of hydrocarbon fuels and batteries.

	$\mathrm{W\,h\,L^{-1}}$	$\mathrm{W\,h\,L^{-1}}$
Fuels		
Hydrogen (STP)	39,000	3
Liquid Hydrogen	39,000	2600
Methanol	5530	4370
Ethanol	7440	5885
Propane	12,870	6320
n-butane	12,700	7280
Isooctane	12,320	8504
Diesel	12,400	8700
Gasoline	9700	12,200
Primary Batteries		
Alkaline	35	70
Lithium/Sulfur Dioxide	170	190
Rechargeable Batteries		
Lead-acid	35–40	40
Nickel/Metal hydride	60–80	280
Lithium-ion	110–125	350

1.3 Fuel Cells

Fuel cells convert chemical energy directly into electrical energy via an electrochemical reaction of a fuel and an oxidizer. Fuel cells are not limited by the Carnot-cycle limit of thermodynamic efficiency, unlike combustion-based heat engines [Larmine and Dicks, 2000; EG&G Technical Services, 2004]. Fuel cells offer a better alternative to batteries because they can operate continuously, so long as fuel is replenished regularly. They can be operated on a variety of fuels, with hydrogen being the popular, ahead of syngas or natural gas. Oxygen which is supplied as air, remains the sole oxidant.

The basic unit of a typical fuel cell consists of three components: an anode, a cathode and an electrolyte. An oxidizable fuel (e.g., hydrogen, methanol) is fed continuously to the anode (negative electrode) while oxidant (e.g., air) is fed to the cathode (positive electrode). Electrons are produced at the anode by electrochemical oxidation reaction, while at the cathode an electrochemical reduction occurs to consume electrons. The half-cell potentials of each reaction dictate the maximum theoretical voltage generated by the cell. Electrolyte placement between the anode and cathode allows exchange of mobile ions between electrodes while forcing electrons through an external circuit to harness the power. Individual fuel cell units may be stacked together using suitable interconnect (e.g., bipolar plates) to connect multiple cells in series to achieve desired output voltage.

1.3.1 Types of fuel cells

Fuel cells are classified based on the electrolyte (in turn dictating the mobile ion) used and the fuel consumed. The main types of fuels cells are alkaline fuel cell (AFC), direct methanol fuel cell (DMFC), phosphoric acid fuel cell (PAFC), molten carbonate fuel cell (MCFC), solid oxide fuel cell (SOFC) and polymer electrolyte membrane fuel cell (PEMFC). A summary of main features of different fuel cells is presented in Table 1.3 [EG&G Technical Services, 2004; Larmine and Dicks, 2000]. The details of each fuel cell

Table 1.3: Summary of different types of fuel cells.

	PEMFC	AFC	DMFC	PAFC	MCFC	SOFC
Electrolyte	Hydrated polymeric ion exchange membrane	Mobilized or immobilized potassium hydroxide in asbestos matrix	Polymer membrane	Immobilized liquid phosphoric acid in SiC	Immobilized liquid molten carbonate in $LiAlO_2$	Perovskites (Ceramics)
Electrodes	Carbon	Transition metals	Methanol	Carbon	Nickel/Nickel Oxide	Pervoskite
Catalyst	Platinum	Platinum	Platinum	Platinum	Electrode material	Electrode material
Interconnect	Carbon	Metal		Graphite	Nickel or Stainless steel	Nickel, ceramic or steel
Operating temperature (°C)	40–80	65–220	50–120	205	650	600–1000
Charge carriers	H^+	OH^-	H^+	H^+	CO_3^-	O^{2-}
Sensitive impurities	CO, Sulfur and NH_3	CO, CO_2 Sulfur	Sulfur	CO, Sulfur	Sulfur	Sulfur

are presented below.

1.3.2 Alkaline Fuel Cells (AFC)

Alkaline fuel cells (AFC) were first described and patented by Reid in 1902 and Noel in 1904 [Gulzow, 2004; Larmine and Dicks, 2000; Bagotsky, 1997]. They were first proven viable by F.T. Bacon in 1960 and patents were sold to United Technology Corporation (UTC) [EG&G Technical Services, 2004; Bagotsky, 1997]. The AFCs were developed by UTC for application in the Apollo space program and used for 18 Apollo space flights [Bagotsky, 1997]. Polymer electrolyte membrane fuel cells are other modern fuel cell which were developed for the Apollo space program. The fuel cell developed by Bacon employs oxygen and hydrogen as fuel with KOH as an electrolyte. It is operated at a temperature range of 200 to 240 °C and pressure of 40 to 55 atm (to reduce the boiling of the electrolyte). The anode consisted of dual-porosity Ni electrolyte, two-layer structure with porous Ni (Raney-nickel) of 14 µm on electrolyte side and a pore diameter of 30 µm on the gas side. The cathode was a porous structure of lithiated NiO. The electrodes can also consist of double layer structure where a electrocatalyst layer is coated with a hydrophobic layer [McLean and Niet, 2002]. The hydrophobic layer prevents the electrolyte from leaking into the reactant gas flow channels and ensures the diffusion of reactant gases to reaction site [McLean and Niet, 2002]. This fuel cell has an advantage for giving quick start and has the capability to reach about 60–70% of theoretical energy efficiency [Kirubakaran *et al.*, 2009].

The schematic of AFC is shown in Figure 1.3. The overall chemical reactions can be summarized as follows:

Anode reaction:

$$2H_2 + 4OH^- \longrightarrow 4H_2O + 4e^- \tag{1.4a}$$

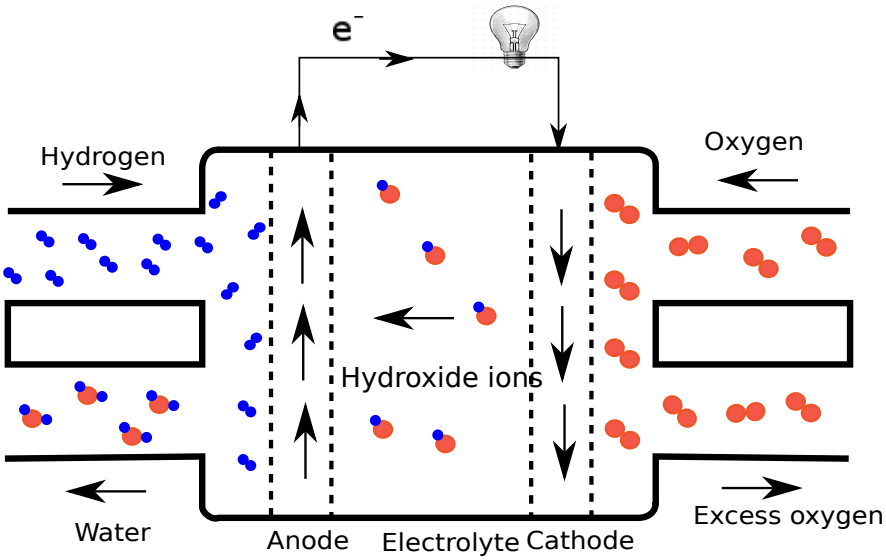

Figure 1.3: Schematic of a typical alkaline fuel cell.

Cathode reaction:

$$O_2 + 2H_2O + 4e^- \longrightarrow 4OH^- \tag{1.4b}$$

Overall cell reaction:

$$2H_2 + O_2 \longrightarrow 2H_2O \tag{1.4c}$$

The major disadvantage of these fuel cells is that they are highly sensitive to CO_2, as it reduces the concentration of electrolyte (KOH) by chemical reaction (Eq. 1.5a). The use of KOH electrolyte in the presence of CO_2 reduces the life span by corroding the electrodes. In the presence of CO_2, the hydroxyl ions precipitate as carbonates and block the electrode pores and electrolyte pathways [McLean and Niet, 2002]. The precipitated carbonate may also reduce the ionic conductivity of electrolyte. The carbon dioxide present in fuel can also react with electrolyte forming potassium carbonate (K_2CO_3). Therefore, CO_2 decreases the performance of the fuel cell. The poisoning reactions can be written as

follows:

$$CO_2 + 2OH^- \longrightarrow CO_3^{2-} + H_2O \tag{1.5a}$$

$$CO_2 + 2KOH \longrightarrow K_2CO_3 + H_2O \tag{1.5b}$$

The presence of CO in the fuel stream negatively affects the fuel cell performance due to poisoning of the anode by limiting the active sites for electrochemical reaction. This effect is reported to be entirely reversible at temperatures above 72 °C and partially reversible below that temperature [McLean and Niet, 2002]. The presence of CO and oxygen alters the surface properties of the electrode and significantly affects the polarization of an AFC [McLean and Niet, 2002].

1.3.3 Phosphoric Acid Fuel Cells (PAFC)

Phosphoric acid fuel cells are first type of fuel cells to be commercialized for civilian use, developed by UTC Fuel Cell in USA, and Fuji Electric company, Toshiba corporation and Mitubushi electric corporation in Japan. PAFC have been installed at 70 sites in USA, Europe and Japan. The 100 kW, 200 kW and 500 kW plants are currently available for stationary and heating applications [Kirubakaran *et al.*, 2009].

The PAFCs use liquid phosphoric acid (H_3PO_4) as the electrolyte, usually immobilized in polytetrafluoroethylene (PTFE) bonded carbide matrix. They operate at a temperature around 175 to 200 °C and are usually at atmospheric pressure. Low operating temperature require platinum catalysts supported on carbon black, to be used both as anode and cathode to ensure rapid reaction. Pt loadings are reported to be about 0.1 mg Pt/cm^2 in the anode and 0.5 mg Pt/cm^2 in the cathode [EG&G Technical Services, 2004]. The electrochemical reactions that occur in PAFC are same as that of PEMFC. The schematic of a typical PAFC

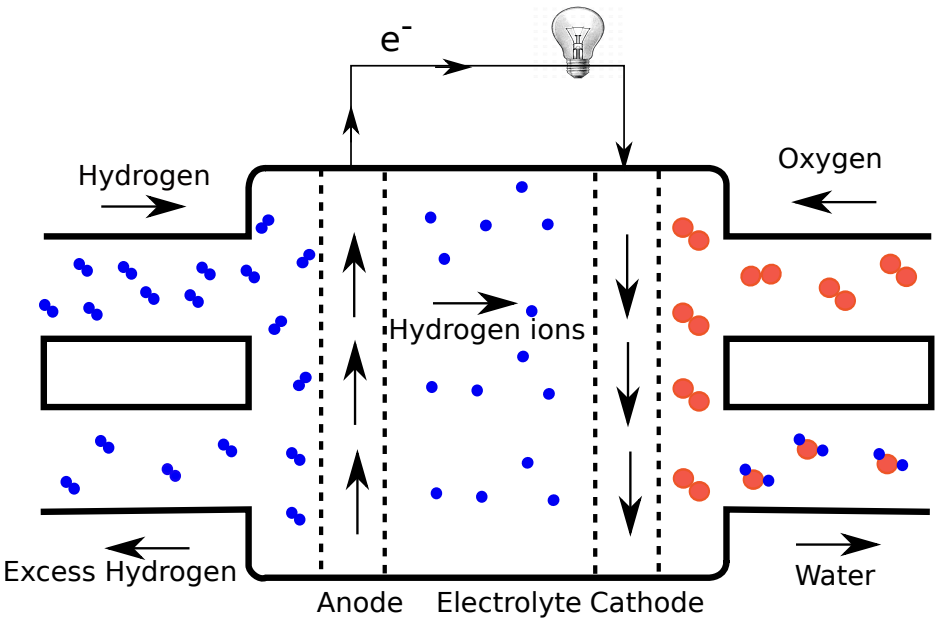

Figure 1.4: Schematic of a typical phosphoric acid fuel cell.

is presented in Figure 1.4.

PAFC power plant designs report electrical efficiencies around 36–42% based on Higher Heating Value (HHV), while higher efficiencies can be achieved by operating at a higher than atmospheric pressure [Nagamoto, 2001]. The main disadvantage of PAFCs is that the platinum electrode is expensive and prone to poisoning by CO. When compared to PEM and AFC, PAFCs have higher tolerance to impurities in reformed hydrocarbons due to higher operating temperature. CO presence in the fuel significantly affects the anode performance by poisoning the platinum catalyst. CO absorbs on the platinum by dual site replacement of one H_2 molecule by two CO molecules on active sites [EG&G Technical Services, 2004]. The acceptable CO concentration depends on the operating temperature of the cell, at 190 °C CO level up to 1% is acceptable and a target level of 0.5% is recommended [Larmine and Dicks, 2000].

1.3.4 Molten Carbonate Fuel Cell (MCFC)

Molten carbonate fuel cells (MCFC) were first reported in 1960s by G.H.J Broers and J.A.A. Ketelaar [Dicks, 2004]. MCFS are originally developed to operate directly on coal as fuel, where as they are now usually operated on coal-derived fuel gas or natural gas in industrial, electrical utility and military applications [Nagamoto, 2001; EG&G Technical Services, 2004; Zhu and Huang, 2012]. They are commercially developed in the United States by FuelCell Energy. MCFCs employ a molten carbonate salt mixture as the electrolyte, typically a liquid mixture of lithium carbonate (Li_2CO_3) and potassium carbonate (K_2CO_3) suspended in a porous, electrically insulating and chemically inert ceramic ($LiAlO_2$) matrix [Nagamoto, 2001; Friedrich *et al.*, 2008]. The fuel cell is usually operated around 600 to 700 °C, the temperature at which the electrolyte mixture is a liquid and a good ionic conductor. The advantage of operating at such a high temperature is that an expensive platinum electrode is not necessary to achieve high reaction rate, thus non-precious metal catalysts can be employed. Currently, Ni and its alloys are used as electrode materials; for example, Ni-Cr/Ni-Al/Ni-Al-Cr and lithiated NiO-MgO have been reported as anode and cathode materials respectively [EG&G Technical Services, 2004]. The schematic of a typical MCFC is presented in Figure 1.5.

The anodic reaction generates CO and water, releasing electrons to the anode. The cathode reaction consumes oxygen and CO_2 while generating carbonate ions. The electrode chemical reactions are as follows:

Anode:

$$H_2 + CO_3^{2-} \longrightarrow H_2O + CO_2 + 2e^- \tag{1.6a}$$

or

$$CO + CO_3^{2-} \longrightarrow 2CO_2 + 2e^- \tag{1.6b}$$

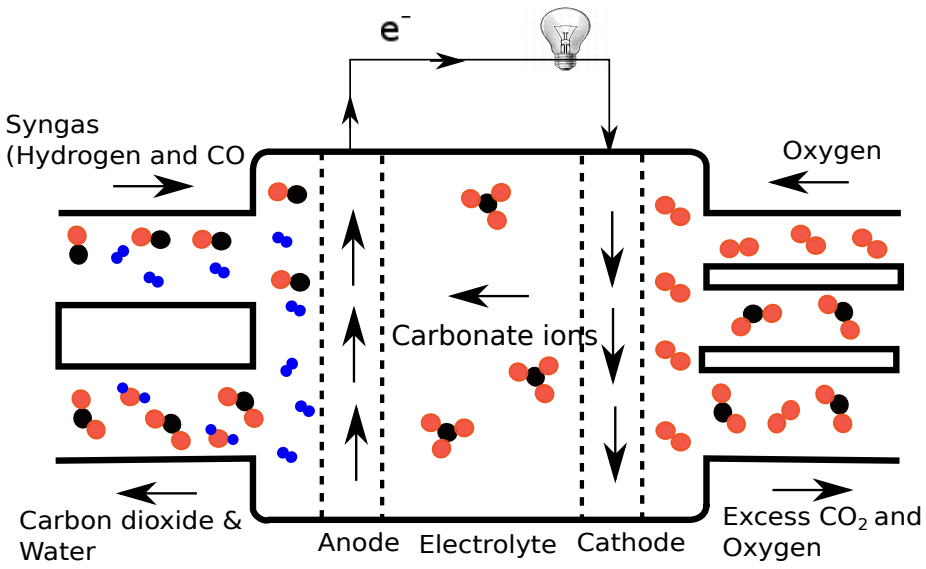

Figure 1.5: Schematic of a typical molten carbonate fuel cell.

Cathode:

$$\frac{1}{2}O_2 + CO_2 + 2e^- \longrightarrow CO_3^{2-} \tag{1.6c}$$

1.3.5 Direct Methanol Fuel Cell (DMFC)

The DMFCs employs a polymer membrane as electrolyte and methanol is used as fuel. In DMFC the anode extracts hydrogen from the liquid methanol without any reformer and reduces the overall cost of the fuel cell. The performance of the DMFC is limited by factors like, crossover of methanol from anode to cathode lowers system efficiency and the slow kinetics of the electrochemical oxidation of methanol [Kirubakaran *et al.*, 2009]. These fuel cells can supply only 0 3 to 0.5 V under loaded conditions and can be used to replace the batteries for cameras, use in notebook computers and other portable electronic applications. The schematic of a typical DMFC is presented in Figure 1.6. The electrochemical reactions that occur in DMFC are as follows:

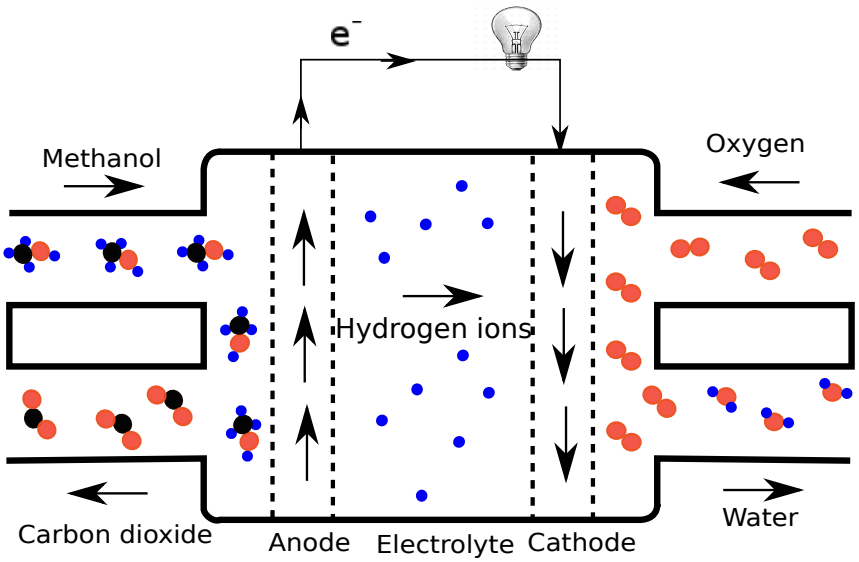

Figure 1.6: Schematic of a typical direct methanol fuel cell.

$$CH_3OH + H_2O \longrightarrow CO_2 + 2H^+ + 6e^- \tag{1.7a}$$

$$\frac{3}{2}O_2 + 6H^+ + 6e^- \longrightarrow 3H_2O \tag{1.7b}$$

1.3.6 Solid Oxide Fuel Cell (SOFC)

The SOFC employs a solid-phase ceramic electrolyte which requires operation at high temperature (600 to 1000 °C) to achieve adequate ionic conductivity. The electrolyte is usually a dense yttrium (Y_2O_3)-stabilized zirconia (ZrO_2), which is an oxygen ion conductor at a high temperature. The anode is typically a Nickel-ZrO_2 cermet and the cathode is strontium-doped lanthanum manganite ($LaMnO_3$) [Kirubakaran *et al.*, 2009; EG&G Technical Services, 2004; Friedrich *et al.*, 2008; Minh, 2004]. Like MCFCs, SOFCs can operate on wide variety of hydrocarbon fuels, because the mobile ion is also the oxi-

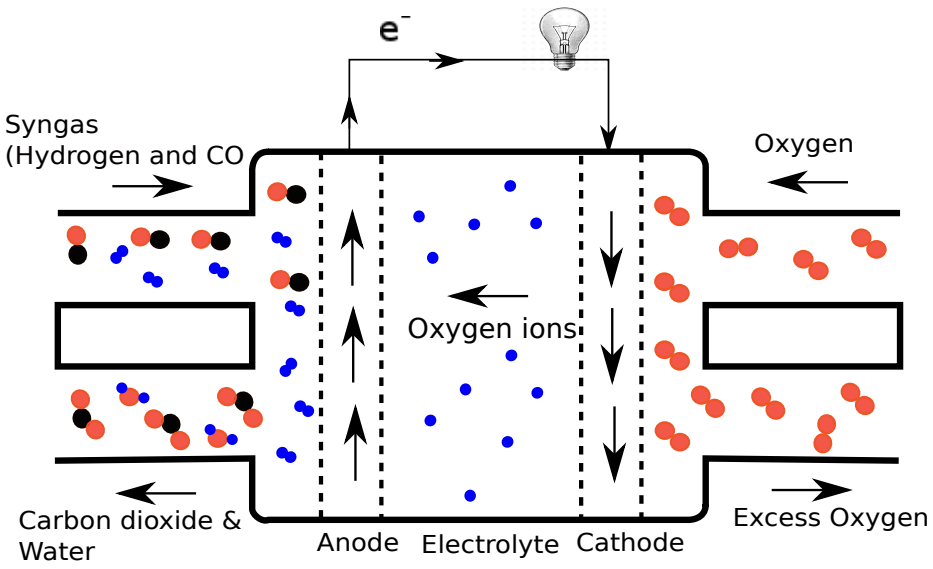

Figure 1.7: Schematic of a typical solid oxide fuel cell.

dizer. To date, cell operation from hydrogen, CO, natural gas and both conventional and bio-diesels. H_2 and CO remain the favored feedstock, to avoid the risk of coking or endotherms within the cell. Fuel reacts with oxide ions supplied by the electrolyte, producing water and CO_2 and electrons. The electrons pass through an external load circuit to the cathode, where they react with oxygen diatoms to produce oxide ions. The schematic of a typical SOFC is presented in Figure 1.7.

The electrode reactions that occur in SOFC are as follows:

Anode:

$$H_2 + O^{2-} \longrightarrow H_2O + 2e^- \tag{1.8a}$$

$$CO + O^{2-} \longrightarrow CO_2 + 2e^- \tag{1.8b}$$

Cathode:

$$\frac{1}{2}O_2 + 2e^- \longrightarrow O^{2-} \tag{1.8c}$$

The SOFCs are developed for a wide range from small (portable devices), medium (residential and automatic power units) and large (distributed generation power plants) power applications [Kirubakaran *et al.*, 2009; Minh, 2004]. The slow start up, high cost and intolerance to sulfur content in hydrocarbon fuel and brittleness of the ceramic electrolyte due to thermal cycling are some of the disadvantages of SOFC [Department of Energy, 2009].

1.3.7 Polymer Electrolyte Membrane Fuel Cells (PEMFC)

The PEMFCs were first developed in 1950s by General Electric (GE) and contracted for the Gemini space mission in 1960s [Wang *et al.*, 2011]. The basic operating principle of the typical PEMFC is presented in Figure 1.8. The first PEMFCs developed by GE employed platinum electrodes and Teflon as the electrolyte [Wang *et al.*, 2011], and had a limited lifetime of 500 hours [Larmine and Dicks, 2000].

The electrolyte used now is typically a proprietary Nafion membrane which was originally developed by E.I. Dupont de Nemours for space applications in 1967 [Larmine and Dicks, 2000; EG&G Technical Services, 2004]. Nafion consists of a perfluoro polymer backbone upon which hydrophillic sulfonic acid groups are chemically bonded. The main features of Nafion membrane are: highly chemical resistant, mechanically strong, acidic, absorbs large quantities of water and conducts H^+ ions freely (when well hydrated) [Larmine and Dicks, 2000; Smitha *et al.*, 2005]. Platinum supported on conducting carbon remainsmost commonly used catalyst for both electrodes, owing to its high catalytic activity at operating temperatures. The first Gemini fuel cell employed a platinum loading of 35 mg Pt/cm^2, while modern cells employ loading of 0.2 mg Pt/cm^2 owing to improvements in catalyst fabrication [Larmine and Dicks, 2000; Wang *et al.*, 2011].

Anode:

$$H_2 \rightarrow 2H^+ + 2e^- \tag{1.9a}$$

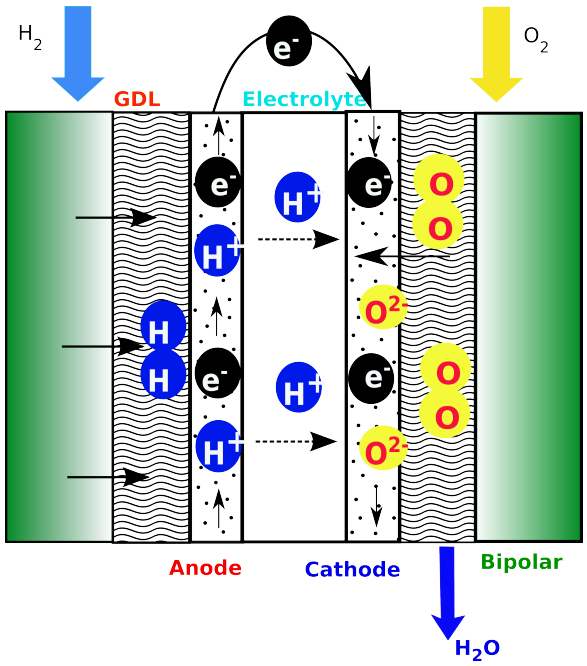

Figure 1.8: Schematic of a typical polymer electrolyte membrane fuel cell.

Cathode:

$$\frac{1}{2}O_2 + 2H^+ + 2e^- \rightarrow H_2O \tag{1.9b}$$

PEMFCs have several advantages over other fuel cells such as low-temperature operation, easy scale-up and high power density. They are highly suitable for portable power applications such as laptops, mobile phones and other electronic devices owing to low-temperature operation. They are also well suited for applications that require quick startup such as automobiles or forklifts. They have been commercially developed for automotive applications by several companies, and it is anticipated that commercial vehicles would be available for sale around 2014 to 2016 [Fuelcells.org, 2013; Wang *et al.*, 2011]. The PEMFC performance degrades when impurities such as CO and CO_2 in the fuel comes in contact with the anode. The details of effect of impurities on PEMFC is presented below.

1.3.7.1 Effect of CO on PEM fuel cell performance

The reduction in performance of PEMFCs is well documented in the literature. The CO in the H_2-rich fuel strongly binds by preferential adsorption to the platinum surface which results in the reduction of the active sites available for hydrogen adsorption and oxidation [Baschuk and Li, 2001; Cheng *et al.*, 2007]. Even trace amounts of CO as low as 10 ppm in dilution hydrogen is shown to cause severe degradation in performance [Cheng *et al.*, 2007]. It is reported that the CO concentration above 25 ppm causes a loss of 20–50% of performance at high current densities [Oetjen and Schmidt, 1996; Cheng *et al.*, 2007]. The effect of CO on the performance of a typical PEM fuel cell is shown Figure 1.9. Figure 1.9 shows the steady-state current-voltage plots of a PEM cell using a fuel of H_2 mixed with CO concentrations of 25 to 250 ppm at the cell temperature of 80 °C. The anode and cathode employed in this study were 30 wt% platinum on Vulcan XC 72 support. CO poisoning becomes more severe with increase in concentration and exposure time owing to accumulation on the platinum surface. The voltage losses of the cell is caused by competing adsorption of CO and H_2 on the platinum electrode. The CO poisoning can be reversed by operating the cell at open circuit voltage with pure hydrogen for a period of 2 to 3 hours [Baschuk and Li, 2001; Oetjen and Schmidt, 1996]. The following mechanism is reported to occur on the platinum electrode [Oetjen and Schmidt, 1996].

$$3\text{Pt} + \text{H}_2 + \text{CO} \longrightarrow \text{Pt-CO} + 2\text{Pt-H} \tag{1.10a}$$

$$\text{Pt} + \text{H}_2\text{O} \longrightarrow \text{Pt-OH} + \text{H}^+ + \text{e}^- \tag{1.10b}$$

$$\text{Pt-CO} + \text{Pt-OH} \longrightarrow \text{Pt} + \text{CO}_2 + \text{H}^+ + \text{e}^- \tag{1.10c}$$

A more detailed review on effect of CO on fuel cell performance can be found in the following references [Baschuk and Li, 2001; Oetjen and Schmidt, 1996; Bruijn and Papageorgopoulos, 2002].

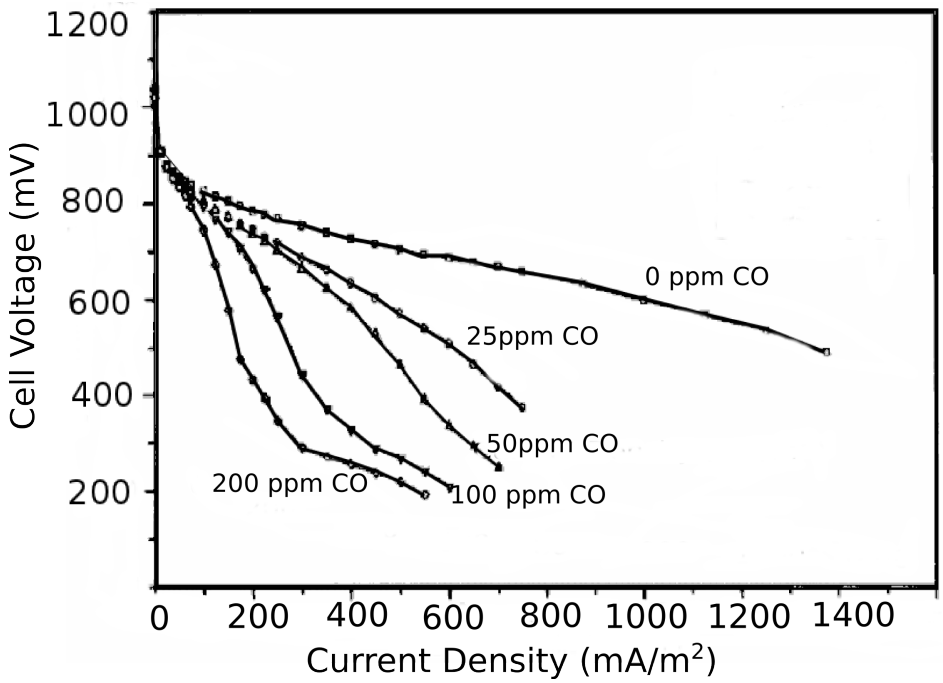

Figure 1.9: Effect of CO on a polymer electrolyte membrane fuel cell [Oetjen and Schmidt, 1996].

1.3.7.2 Effect of CO_2 on PEM fuel cell performance

The performance of a PEM fuel cell degrades rapidly in the presence of CO_2 in the fuel (Figure 1.10). This effect is more pronounced when a fuel cell electrode is exposed

for longer period of time and higher CO_2 concentrations [Rajalakshmi *et al.*, 2003; Bruijn and Papageorgopoulos, 2002; Cheng *et al.*, 2007]. It is reported that 20% CO_2 reduces the performance of the cell by 40% at a 0.5 V [Bruijn and Papageorgopoulos, 2002]. This voltage loss due to CO_2 contamination can be recovered, owing to the reverse water-gas-shift reaction taking place on the platinum electrode which converts CO_2 into CO and H_2. However, CO produced from the reverse water-gas-shift (WGS) reaction accumulates on the platinum electrode blocking the active sites available for hydrogen oxidation resulting in performance loss (as discussed previously). The following kinetic mechanism was proposed for adsorption and conversion of CO_2 to CO on the platinum surface [Cheng *et al.*, 2007]:

$$2\text{Pt} + \text{H}_2 \longrightarrow 2\text{Pt-H} \tag{1.11a}$$

$$\text{CO}_2 + 2\text{Pt-H} \longrightarrow \text{Pt-CO} + \text{H}_2\text{O} + \text{Pt} \tag{1.11b}$$

The major issue with commercialization PEMFCs is the poisoning of platinum catalyst by impurities (CO, CO_2) (as discussed previously) which increases the cost and decreases the lifetime/durability. Therefore, the on-board hydrogen production from cheap renewable sources and purification from CO becomes a critical factor for their commercialization.

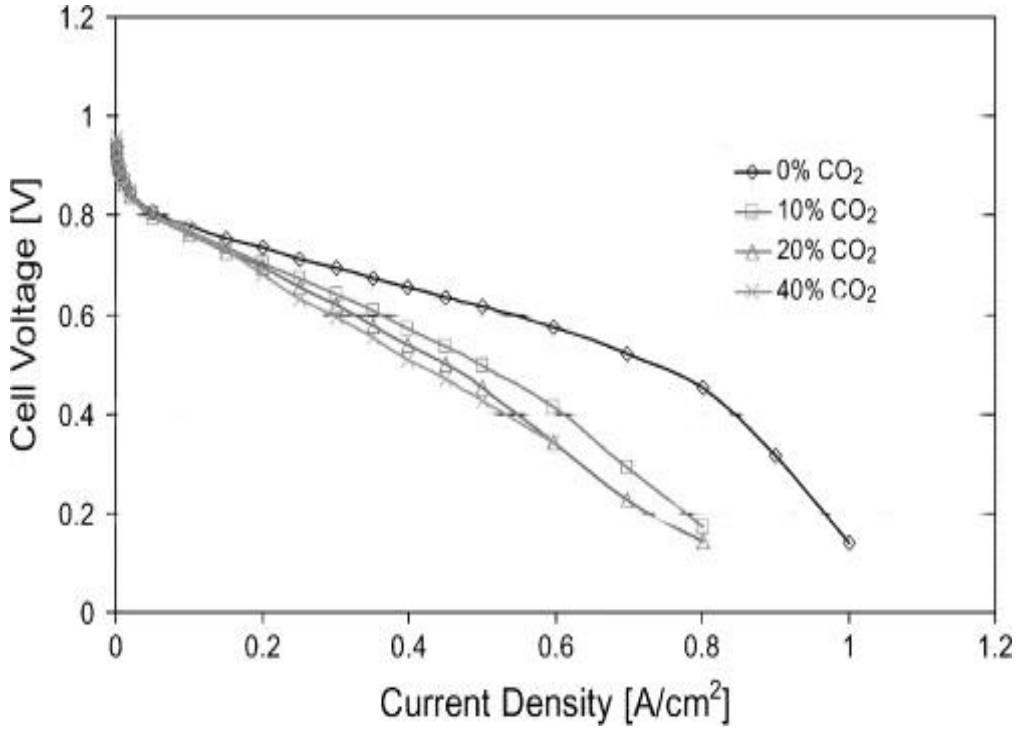

Figure 1.10: Effect of CO_2 on a polymer electrolyte membrane fuel cell: The polarization curve of a fuel cell at various CO2 concentrations (Anode, Cathode: 0.35 mg Pt/cm^2 E-TEK ELAT gas diffusion electrode; Electrolyte: Nafion 105; Cell and humidity temperature: 65 °C; Pressure: 1.5 bar) [Bruijn and Papageorgopoulos, 2002].

1.4 Hydrogen production

While hydrogen is the most abundant element occurring in nature, it is only available in a bonded form. It must therefore be harvested from raw materials. It can be harvested from diverse raw materials such as coal, oil or natural gas, or renewable (biomass and alcohols) sources [Holladay *et al.*, 2009]. Figure1.11 shows current sources of global hydrogen production. Hydrogen can be produced using various technologies namely, hydrocarbon (natural gas and liquid) reforming, electrolysis and coal gasification. Hydrogen can also be produced using lesser efficient processes such as photobiological technology and solar electrolysis. The details of these technologies are described below.

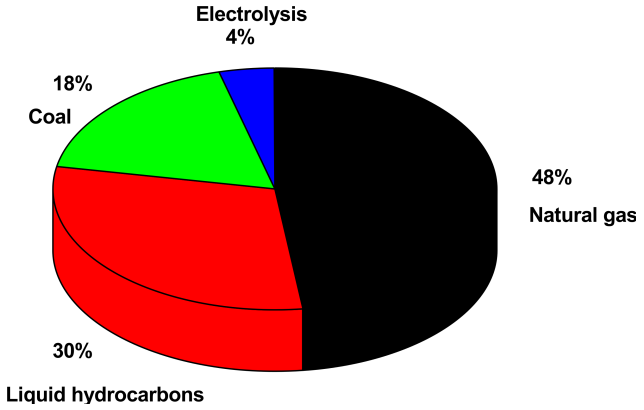

Figure 1.11: Current sources of global hydrogen production [Armaroli and Balzani, 2011].

1.4.1 Electrolysis of water

Electrolysis of water is commercial and mature technology used to produce hydrogen. Electrolysis was discovered in 1800s and electrolyzer industry grew substantially in 1920s and 1930s. Electrolyzer consists of no moving parts and can use direct current making it a simplest technology to produce hydrogen. Electrolysis process is capable of achieving 99.999% hydrogen purity. It is only technology that can produce large quantities of hydrogen without emitting byproducts of hydrocarbon reforming such as CO, CO_2 and CH_4. Commercial electrolyzers are capable of achieving 50–70% efficiency. This electrolysis process is energy intensive, requiring energy in the range of 70.1 to 53.4 $\mathrm{kW\,h\,kg^{-1}}$ [Turner *et al.*, 2008; Turner, 2004; Haryanto *et al.*, 2005]. A schematic of a basic electrolysis cell is shown in Figure 1.12. Electrolysis of water uses two basic types of low-temperature processes, alkaline and polymer electrolyte membrane (PEM).

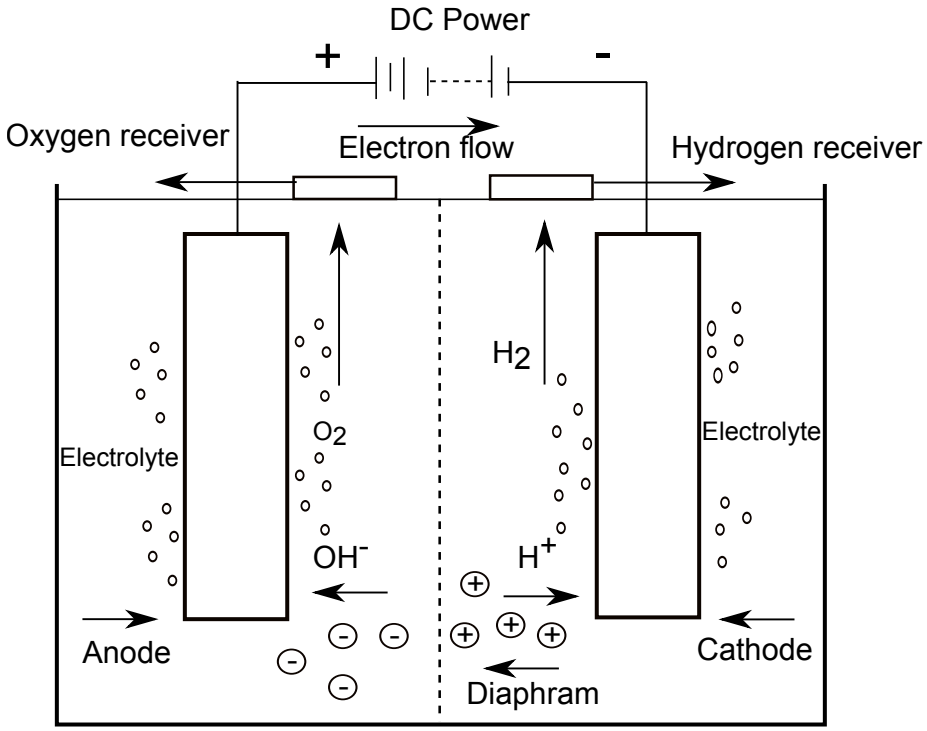

Figure 1.12: Schematic of a basic electrolysis process.

1.4.2 Hydrocarbon reforming

Hydrocarbon reforming to H_2, CO, CO_2 and CH_4 can be accomplished using combination of endothermic steam reforming, exothermic partial oxidation, water-gas-shift reaction and autothermal reforming. Hydrocarbon reforming of natural gas and light oil fraction represents 90% of present hydrogen production [Haryanto *et al.*, 2005]. Hydrocarbons reforming to H_2, CO, and CO_2 is endothermic, as cleavage of C-H and O-H bonds is required. However, when a suitable catalyst is used it requires only modest temperatures.

1.4.2.1 Steam reforming

Hydrocarbon steam reforming represents 95% of present hydrogen production in United States [Haryanto *et al.*, 2005]. Steam reforming is an endothermic process limited by thermodynamics, which requires an external heat source. The catalyst for reforming are

primarily based on two types namely, i) non precious metals such as Ni, Fe, Cu and Co, ii) group VIII elements such as platinum and rhodium. There are many catalyst suggested in the literature; the best performing catalysts are Co/ZnO, Rh/Al_2O_3, ZnO, $RhCeO_3$ and Ni/La_2O_3-Al_2O_3 [Holladay *et al.*, 2009]. In practice, hydrocarbon steam reforming generates other byproducts comprising significant amounts of CO (by pyrolysis), CO_2 (by reverse water-gas-shift reaction) and CH_4 (by methanation) along with hydrogen. The general chemistry of hydrocarbon steam reforming is as follows:

$$C_nH_mO_z + (n-z)\,H_2O \longleftrightarrow nCO + 6\left(n + \tfrac{m}{2} - z\right)H_2 \;\; \triangle H_r > 0 \tag{1.12}$$

1.4.2.2 Partial oxidation (POX)

Partial oxidation (POX) utilizes O_2 as oxidant enabling exothermic reforming at reduced H_2 yields. Partial oxidation can be divided into non-catalytic and catalytic processes, the former requires a high flame temperature of 1300 to 1500 °C to ensure complete conversion of carbon, and the latter employs a catalyst, thus require only modest temperatures [Holladay *et al.*, 2009]. The carbon to oxygen ratio dictates the heat of reaction and hydrogen yield [Moreno, 2010]. The catalysts for partial oxidation are primarily based on nickel and rhodium when using natural gas as the feed. The problems associated with this process are soot formation and poisoning of catalyst by sulfur present in the hydrocarbons. The general chemistry of hydrocarbon partial oxidation can be written as follow:

$$C_nH_mO_z + {}^{n}/_{2}O_2 \longleftrightarrow nCO + {}^{m}/_{2}H_2 \;\; \triangle H_r < 0 \tag{1.13}$$

1.4.2.3 Water-gas-shift reaction (WGS)

Significant amounts of CO is present in steam reforming and partial oxidation reactions, water-gas-shift reaction is used as a unit operation for cleanup and increase the

overall hydrogen yield. WGS reaction is mainly used since 1960s for various industrial applications in ammonia production, hydrotreating of petroleum and coal processing [Shoko *et al.*, 2006]. It is exothermic, typically requires a high temperature to achieve fast kinetics but results in carbon monoxide selectivity and low hydrogen production. Catalysts such as copper oxide, molybdenum carbide, platinum based catalysts and Fe-Pd alloys are employed to increase the rate of reaction. A high-temperature shift reactor is followed by a low-temperature shift reactor to achieve high hydrogen selectivity and fast reaction kinetics. Cu/ZnO/Al_2O_3 is used as the catalyst for low-temperature shift reaction and Fe_2O_3-Cr_2O_3 catalyst is used for the high-temperature reactor [Shoko *et al.*, 2006]. The reaction is as follows:

$$CO + H_2O \longleftrightarrow CO_2 + H_2 \quad \triangle H^0_{298} = -42\,\mathrm{kJ\,mol^{-1}} \tag{1.14}$$

1.4.2.4 Autothermal reforming

Autothermal reforming combines the heat of reaction of three reactions, steam reforming, partial oxidation and water-gas-shift reaction. In this type of reforming, the feed is a mixture of hydrocarbon and steam, which is combined with oxygen. The autothermal reforming can be used to convert both lighter and heavier hydrocarbons, the endothermic heat of hydrocarbon reforming is negated by the partial oxidation heat of reaction. Thermal management is achieved by adjusting the ratio of hydrocarbon to steam and oxygen. The reaction takes place in presence of a catalyst such as CuO/ZnO/Al_2O_3, which dictates the reaction pathway and overall hydrogen yield. The problems associated with autothermal reforming are this type of design are: a) the manipulation of optimal ratio of hydrocarbon to oxygen in the feed is difficult under zero enthalpy conditions, b) it is difficult to find a catalyst that is efficient for both steam reforming and oxidation. The general chemistry of

autothermal reforming of hydrocarbon is:

$$C_mH_nO_z + (2n - 2x - z)\,H_2O + xO_2 \longleftrightarrow nCO_2 + (2n - 2x - \frac{1}{2}m)H_2 \;\; \triangle H_r < 0 \quad (1.15)$$

1.5 Bioethanol as a fuel

Bioethanol is an attractive fuel for hydrogen production given that it is renewable and can be produced from myriad of agricultural and waste biomass in dilute concentration (12 wt%) [Ni *et al.*, 2007; Sánchez and Cardona, 2008; Goldemberg, 2007]. Bioethanol is also biodegradable, easy to transport, low in toxicity, and has the advantage of being able to produce without trace of sulfur or metals (unlike other hydrocarbons). It is miscible with water to create multiple steam reforming blends for different applications. Bioethanol can be converted into hydrogen by hydrocarbon reforming techniques: i) steam reforming, ii) partial oxidation, iii) water-gas-shift reaction, and iv) autothermal reforming.

Bioethanol is produced from fermentation process of several biomass and agricultural products such as sugar cane, switchgrass, potatoes, corns and other starch-rich materials [Ni *et al.*, 2007; Lin and Tanaka, 2006; Turner, 2004; Balat and Kırtay, 2010; Winter, 2009]. The wood residues are the largest source for bioethanol production for energy production [Lin and Tanaka, 2006; Galbe and Zacchi, 2002]. The glucose in biomass materials is converted into ethanol and carbon dioxide through the anaerobic (insufficient availability of oxygen) respiration of yeast. Figure 1.13 shows a general flowchart of conversion of biomass feedstock to ethanol.

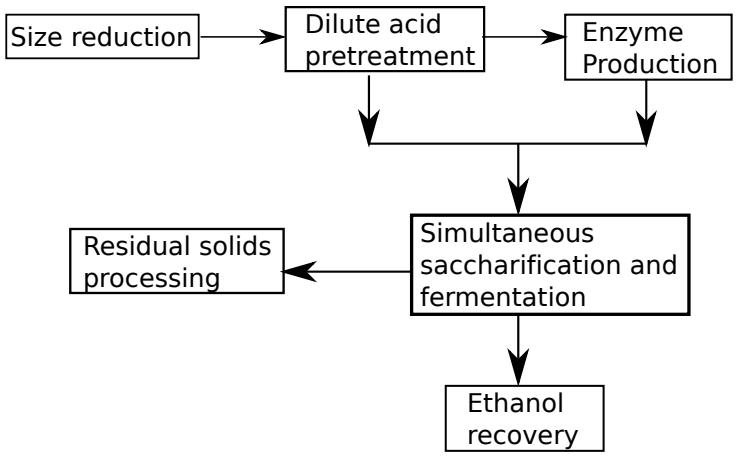

Figure 1.13: Schematic of the conversion of biomass feedstock to ethanol [Lin and Tanaka, 2006].

1.6 Hydrogen purification

Reforming of hydrocarbons generates hydrogen-rich reformate mixtures containing significant amounts of carbon monoxide, carbon dioxide and steam. Further hydrogen purification from reformate mixtures is warranted for its use in industrial and portable applications. A summary of hydrogen purity requirements in various applications is presented in Table 1.4. This can be achieved via pressure swing adsorption (PSA), cryogenic distillation and gas separation membranes.

Table 1.4: Summary of hydrogen purity requirements in various applications [Ockwig and Nenoff, 2007].

Application	Hydrogen purity (%)
Rocket engine fuel	99.999999
Semiconductor	99.999999
PEM fuel cell	99.99
Hydrodesulfurization	90
Hydrocracking	70–80
Fuel gas	54–60

1.6.1 Pressure swing adsorption (PSA)

Pressure swing adsorption (PSA) is a well-established commercial gas separation process used for several applications including air separation, noble gas separation, gas drying and hydrogen purification [Adhikari and Fernando, 2006; Biegler *et al.*, 2004]. PSA process is based on the capacity of a porous solid adsorbent, such as activated charcoal or zeolite material of large surface area to adsorb impurities (N_2, CO, CO_2, water vapor and hydrocarbons) at a high pressure (generally $> 10\,\text{MPa}$). A typical PSA unit is shown in Figure 1.14 [Grande, 2012]. The process is carried out in swings of adsorption and desorption; impurities are adsorbed at a higher gas partial pressure until an equilibrium is reached and then it is desorbed at a lower partial pressures [Sircar and Golden, 2000; Grande, 2012]. PSA process can achieve hydrogen purities up to 99.99% at high recoveries. Hydrogen recovery is dependent on several factors such as inlet pressure, purge gas pressure, level of impurities and hydrogen concentration in the feed [Adhikari and Fernando, 2006; Biegler *et al.*, 2004]. PSA process can be operated in both continuous or batch-wise. A detailed review of PSA process can be found elsewhere [Grande, 2012; Sircar and Golden, 2000; Adhikari and Fernando, 2006].

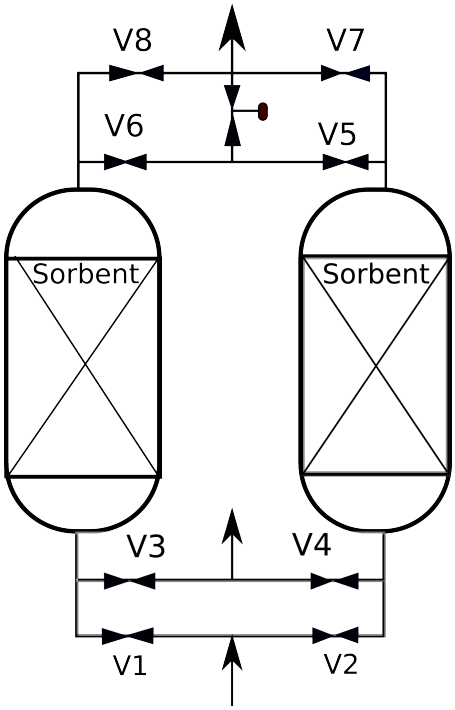

	Feed	Evacuation	Purge	Pressurization
Column 1	V1, V7	V3	V5, V3	V1
	Purge	Pressurization	Feed	Evacuation
Column 2	V6, V4	V2	V2, V8	V4

Figure 1.14: Schematic of a two-column pressure swing adsorption unit and valve sequencing for different steps in the cycle [Grande, 2012].

1.6.2 Cryogenic distillation

Cryogenic distillation process is another widely used industrial gas separation process [Koros and Mahajan, 2000; Hinchliffe and Porter, 2000; Shao *et al.*, 2009]. It is a low-temperature process which takes advantage of high relative volatility of hydrogen compared to hydrocarbon gas mixtures [Adhikari and Fernando, 2006]. The simplest and most commonly used cryogenic distillation is partial condensation process in which im-

purities in feed are condensed against warmer product and tail gases [Miller and Stöcker, 1989]. Cryogenic distillation is capable of producing hydrogen purities up to 95% at hydrogen recoveries of 92–97% [Miller and Stöcker, 1989; Shao *et al.*, 2009]. However, if significant amounts of CO and CO_2 are present in the feed stream, it requires a methane wash column to remove these gases and achieve a high hydrogen recovery [Adhikari and Fernando, 2006]. Cryogenic distillation is an energy intensive process, consuming considerable amount of energy to maintain very low operating temperature [Adhikari and Fernando, 2006].

1.7 Hydrogen permselective membranes

Although pressure swing adsorption and cryogenic distillation are commercially well established technologies, membrane systems are particularly desirable owing to low capital costs, low energy consumption and higher energy efficiency, continuous operation and ease of operation for portable and high-capacity applications [Ockwig and Nenoff, 2007; Shao *et al.*, 2009]. For the present review, hydrogen permselective membranes are divided into the following categories based on the material properties namely, i) metallic membrane, ii) polymer membranes, iii) carbon membrane, iv) silica membranes, and v) ceramic membranes.

1.7.1 Metallic membranes

Metallic membranes are thin, dense sheets made up of pure elements such as palladium, niobium, vanadium, platinum and tantalum [Ockwig and Nenoff, 2007; Adhikari and Fernando, 2006]. The dense metallic films should possess the following properties to be suitable for hydrogen separation: i) ability to dissociate and reassociate surface-chemisorbed hydrogen, ii) high hydride ion solubility in the metal, and iii) stability against formation of native oxides on the metal surface [Paglieri and Way, 2002; Ockwig and Nenoff, 2007].

Palladium and its alloys are extensively investigated in the literature owing to high hydrogen permeability and solubility [Gallucci *et al.*, 2013; Ockwig and Nenoff, 2007]. Palladium dissociates hydrogen and the hydride ions are transported across the membrane and reassociated into hydrogen on the product side. Palladium rejects large atoms and molecules such as CO, CO_2, O_2, N_2, etc. Pure palladium membranes show infinite inherent theoretical permselectivity, capable of achieving hydrogen separation for practical purposes up to a purity of 99.99% and high hydrogen selectivity ($>$ 1000:1) [Ockwig and Nenoff, 2007; Adhikari and Fernando, 2006].

They are plagued by numerous problems such as prone to corrosion by hydrocarbon and sulfur compounds, embrittlement and degradation at temperatures $\sim$ 300 °C owing to significant difference in lattice constants [Paglieri and Way, 2002; Gallucci *et al.*, 2013; Adhikari and Fernando, 2006; Ockwig and Nenoff, 2007]. Embrittlement and degradation of palladium membranes can be alleviated by alloying with metals such as Ag, Cu, Au and Ru [Paglieri and Way, 2002], but at the cost of decrease in hydrogen permeability. Hydrocarbon poisoning can be placated by operating at sufficiently high temperatures to minimize competitive adsorption effects. Palladium is prohibitively expensive to be considered for hydrogen separation for use in fuel cells for portable applications.

1.7.2 Silica membranes

Microporous silica membranes with pore size $<$ 1 nm have been successfully employed for hydrogen purification [Ockwig and Nenoff, 2007; de Vos and Verweij, 1998; Wei *et al.*, 2008; Tsuru *et al.*, 2001]. Silica membranes have several advantages for hydrogen separation such as ease of production, low-cost fabrication and scalability [Ockwig and Nenoff, 2007]. These membranes are also not susceptible to hydrogen embrittlement and are less expensive, as compared to palladium and its alloys. Microporous silica membrane are produced using either sol-gel dip coating or chemical vapor deposition, with

reported H_2/N_2 selectivities exceeding 10,000:1 [Ockwig and Nenoff, 2007; Adhikari and Fernando, 2006]. They show poor chemical stability when exposed to water vapor, which is either a product or a reactant in hydrocarbon reforming [Wei *et al.*, 2008; Ockwig and Nenoff, 2007]. It is also reported that the hydrogen flux decreases when exposed to high temperatures and water vapor, owing to the deterioration of pore structures [Wei *et al.*, 2008]. These drawbacks limit the use of silica membranes for reformate cleanup or reformer membrane reactors.

1.7.3 Carbon membranes

Carbon membranes are another class of size-selective membranes [Ockwig and Nenoff, 2007; Ismail and David, 2001]. Carbon-based membranes were first synthesized in the 1970's, and they can be classified into two classes: molecular sieving (CMS) and surface diffusion membranes. Carbon nanotube membranes consist of single-walled pores of 1 nm pore diameter which facilitate selective surface diffusion of hydrogen. The former have pore diameters in the range of 3 to 5 Å, while kinetic diameters of H_2, CO, CO_2, N_2 are 2.89, 3.73, 3.3 and 3.64 nm respectively. Carbon based membranes can be used in non-oxidizing environments and temperatures in the range of 773 to 1173 K [Adhikari and Fernando, 2006]. The hydrogen selectivity for molecular sieve membranes is in the range of 4 to 20 [Kluiters, 2004]. Carbon-based membranes while promising, requires costly fabrication methods and possess poor mechanical properties leading to embrittlement when exposed to water vapor (H_2O) [Bernardo *et al.*, 2009; Kluiters, 2004; Ockwig and Nenoff, 2007].

1.7.4 Polymer membranes

Gas separation technologies employing polymer membranes are in industrial use today for purifying hydrogen from gas mixtures consisting of nitrogen, carbon monoxide and hydrocarbons [Adhikari and Fernando, 2006; Paglieri and Way, 2002; Alexander Stern,

1994; Koros and Mahajan, 2000; Koros and Fleming, 1993]. Polymer membranes for hydrogen separation are available commercially from several companies including Air Products, Linde, BOC and Air Liquide [Kluiters, 2004]. Polymer membranes compete with other technologies for separation of hydrogen from synthesis-gas (syngas) and to recover hydrogen from purge or off-gas streams in petrochemical industries [Paglieri and Way, 2002].

Polymer membranes employ dense thin polymeric films, capable of selectively transporting gas species based upon a solution-diffusion mechanism, wherein gaseous molecules are absorbed on to the surface, dissolved into bulk material (solution) and transported across the membrane (diffusion). Dense polymer membranes may be broadly classified into glassy and rubbery polymer materials, with former having higher selectivity and lower permeability, and latter providing higher higher permeability at reduced selectivity [Ockwig and Nenoff, 2007]. Polymer membranes can also be divided as H_2 selective and H_2 rejective. The H_2 selective polymers exploit the small kinetic diameter of hydrogen compared to any other gases, therefore high diffusivity in the material. The H_2 rejective polymers exploit the lowest critical temperature (T_c) of hydrogen and therefore low solubility compared to other gases. H_2 rejective polymer membranes incorporate polar groups such as poly(propylene oxide), poly(ether oxide), poly(ester-ether), or poly(urethane-ether) which solubilize the polarizable molecules such as CO, CO_2 and NO_x [Ockwig and Nenoff, 2007], thus purifying hydrogen from gas mixtures.

Polymer membranes are capable of achieving high hydrogen fluxes at permselectivities of 50 to 200 [Ockwig and Nenoff, 2007; Adhikari and Fernando, 2006; Koros and Fleming, 1993; Koros and Mahajan, 2000]. They have good ability to cope with high pressure drops for gas separation [Adhikari and Fernando, 2006]. However, they have disadvantages such as limited mechanical strength, relatively high sensitivity to swelling and compaction, and susceptibility to corrosion by CO_2, sulfur oxides (SO_x) and the limited

operating temperature due to thermal decomposition $> 100\,^{\circ}$C [Ockwig and Nenoff, 2007; Paglieri and Way, 2002; Adhikari and Fernando, 2006].

1.7.5 Ceramic membranes

Ceramic membranes are porous or dense materials made up of a metal combined with non-metal in the form of oxide, nitride or carbide [Adhikari and Fernando, 2006; Kluiters, 2004]. Porous ceramic membranes consist of two structures, a chemically inert support material (alumina, zirconia, silica or titania) and gas separation material. Dense ceramic membranes are proton conducting materials made up of $SrCeO_{3-\delta}$ and $BaCeO_{3-\delta}$, transport hydrogen in the form of hydride ions through solution-diffusion mechanism [Kluiters, 2004]. Ceramic membranes can be fabricated using Chemical Vapor Deposition (CVD), sol-gel, or electroless techniques [Adhikari and Fernando, 2006]. A high performance of ceramic membrane is reported with H_2/N_2 selectivities up to 1000 [Adhikari and Fernando, 2006] and promising hydrogen fluxes. The major disadvantage of ceramic membranes is chemical stability in the presence of CO_2 (leading to carbonate formation), traces of sulfur (leading to sulfide or sulfate formation), and H_2O (leading to hydride formation and traces of sulfur) [Kluiters, 2004].

1.7.6 Composite catalytic permselective membranes

Composite membrane designs have been reported to overcome above stated problems of the permselective materials and enhance the separation performance [Wilhite *et al.*, 2004, 2006]. Addition of a porous catalytic layer to the permselective material can modify the gas composition reducing the corrosive nature or undesired permeate content, resulting in enhancement of desired product permeance and selectivity [Kim *et al.*, 2012; Wilhite *et al.*, 2004]. This concept of mitigation of corrosion in palladium thin-film membranes by methanol are experimentally demonstrated in a miniaturized membrane reformer [Wilhite *et al.*, 2004]. Wilhite in [Wilhite, 2011] reported a theoretical analysis elucidating the

design rules for the case of hydrogen purification by a water-gas-shift reaction. Kim et al. [Kim *et al.*, 2012] experimentally demonstrated the composite membrane concept using a porous stainless steel (PSS) electroless plated with palladium membranes in contact with a catalyst active for water-gas-shift reaction. As will be discussed, this concept of enhancement of permselective materials separation performance will be extended in this Thesis for hydrogen separation without employing any permselective materials.

1.7.7 Summary of H_2 permselective materials

A summary of properties and performance of H_2 permselective materials is presented in Table 1.5. Figure 1.15 shows the trade-offs between membrane stability, permeability and permselectivity.

Table 1.5: Summary of H_2 permselective materials and their properties [Kluiters, 2004; Adhikari and Fernando, 2006].

	Dense polymer	Porous ceramic	Dense metallic	Carbon	Dense ceramic
Temperature range	$<$373 K	473–873 K	573–873 K	773–1173 K	873–1173 K
H_2 selectivity	50–200	5–139	$>$1000	4–20	$>$1000
Flux (10^{-3} mol m^2 s)	low	60–300	60–300	10–200	6–80
Stability issues	HCl, SO_x		H_2S, HCl, CO	Water vapor	H_2S, CO_2, H_2O
Transport mechanism	solution-diffusion	molecular sieving	solution-diffusion	surface-diffusion or molecular sieving	solution-diffusion

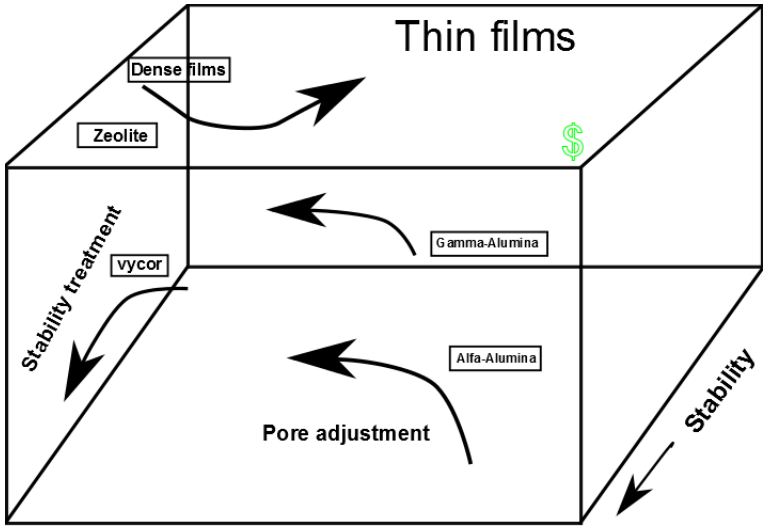

Figure 1.15: The trade-offs between membrane stability, permeability and permselectivity [Dixon, 1999].

1.8 Membrane reactors

Catalytic reactions and subsequent separation of the desired reaction product are traditionally performed in two separate unit operations within a chemical process. Membrane reactors combine these two unit operations into a single processing unit resulting in enhanced product yield and selectivity which improves overall process economics and minimizes waste. Membrane reactors are highly advantageous for equilibrium-limited chemical reactions, as the permselective removal of one or more products shifts the thermodynamic equilibrium to achieve higher conversions and product yields than conventional reactors. This strategy is also useful for manipulating parallel/series reaction networks to enhance the desired product yield.

This is typically accomplished in two main configurations, either as a separate unit operation or in tandem with a catalytic reaction. The latter configuration which is also known as a membrane reactor has been widely investigated over the years, as it allows a parallel integration of separation technology and catalytic reaction. In early years of membrane reactor research, the separation unit is followed by the reactor unit in series and classified as membrane reactor. However, in later years these two distinct unit operations are combined into a single unit operation employing different configurations depending on application. While there are several membrane reactor configurations reported in the literature (as shown in Table 1.6), three most commonly employed configurations are shown in Figure 1.16.

Table 1.6: Classification of membrane reactors [Marcano and Tsotsis, 2002].

Acronym	**Description**
CMR	Catalytic membrane reactor
CNMR	Catalytic non-permselective membrane reactor
PBMR	Packed-bed membrane reactor
PBCMR	Packed-bed catalytic membrane reactor
FBMR	Fluidized-bed membrane reactor
FBCMR	Fluidized-bed catalytic membrane reactor

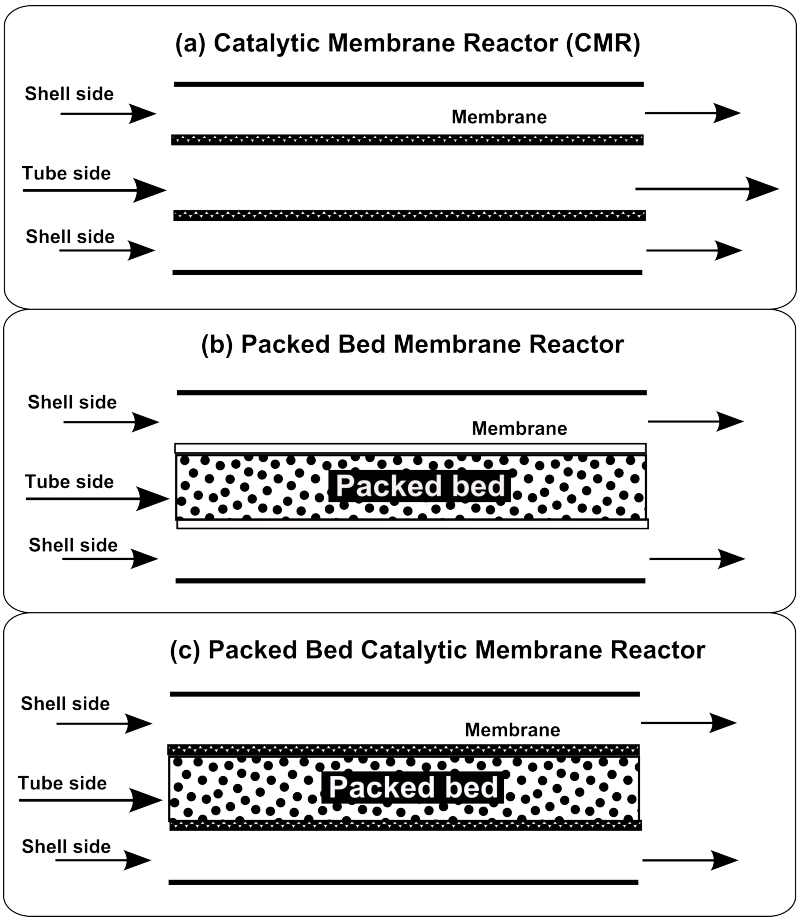

Figure 1.16: Schematic of the three membrane reactor configurations [Dixon, 1999].

1.8.1 Packed bed membrane reactor (PBMR)

In a PBMR, catalyst material is packed in a tube/shell and a permselective membrane is coated/deposited on the shell/tube such that reaction and separation occur in parallel. A typical PBMR consists of a retentate and permeate volume in which reactants and sweep gases are fed respectively. Permeate volume is maintained at a lower pressure than that of retentate volume, thus maintaining a driving force required for permeation of gas species.

Packed bed membrane reactors have been extensively studied for equilibrium limited

reactions, including dehydrogenation of cyclohexane [Itoh, 1990], ethylene [Itoh *et al.*, 1995], propane, isobutane and n-butane [Roh *et al.*, 1999] and also, methane steam reforming water-gas-shift reactions [Dixon, 1999]. A detailed review of PBMR and its derivative configurations are presented by Dixon in [Dixon, 1999].

1.8.2 Catalytic membrane reactor (CMR)

A catalytic membrane reactor in which reactant(s) are segregated between retentate and permeate volumes has been investigated in the literature for various applications and reactions. Catalytic membrane reactors offer high flexibility for varying retentate/feed and permeate/sweep flow rates independently, thus, providing an easier manipulation of reaction-diffusion phenomena within catalytic membrane. These catalytic membrane reactors have been previously investigated for overcoming the equilibrium limitation of reversible reactions upon conversion, manipulating stoichiometry and desired product selectivity.

A catalytic membrane reactor with segregated reactants was first investigated by Sun and Khang in 1988 [Sun and Khang, 1988, 1990], who employed a vycor glass membrane impregnated with Pt/Al_2O_3 catalyst for cyclohexane dehydrogenation. They reported the theoretical and experimental demonstration of achieving conversion in excess (twice) of equilibrium limitation. In this paper a comparison between a catalytic membrane reactor and an inert membrane reactor with catalyst pellets in feed-side chamber. It was concluded that a catalytic membrane reactor shows superior performance to that of the inert membrane reactor. Champagnie et al. [Champagnie *et al.*, 1992, 1990] employed a Pt-impregnated alumina catalytic membrane to study ethane dehydrogenation. They demonstrated a six-fold increase in conversion over the equilibrium-limit of conversion, which was attributed to the selective removal of hydrogen owing to Knudsen selectivity of the membrane. Itoh et al. [Itoh *et al.*, 1988] used a microporous glass tube with Knudsen

selectivity to demonstrate cyclohexane dehydrogenation conversions in excess of thermodynamic equilibrium. Zaspalis et al. [Veldsink *et al.*, 1992; Zaspalis and Burggraaf, 1992; Zaspalis *et al.*, 1991] also used a catalytically active membranes for NO_x reduction and methanol dehydrogenation reactions. Zaspalis et al. studied different feed strategies for methanol dehydrogenation on γ-Al_2O_3/α-Al_2O_3 and Ag/γ-Al_2O_3/α-Al_2O_3 catalysts. They have also studied the effect of different types of operation of the reactor (premixed or separated feed) on selectivity.

Catalytic membrane reactor offers good controllability of fast, highly exothermic, heterogenous reactions which require strict stoichiometric ratio [Sloot, 1991; Sloot *et al.*, 1990; Veldsink *et al.*, 1992]. Sloot et al. [Sloot *et al.*, 1990; Sloot, 1991] demonstrated this by employing the highly exothermic Claus reaction in an α-Al_2O_3 membrane with a mean pore diameter of 350 nm impregenated with γ-Al_2O_3 catalyst. The Claus reaction for reduction of hydrogen sulfide is shown below:

$$2H_2S + SO_2 \longrightarrow \frac{3}{8}S_8 + 2H_2O \tag{1.16}$$

The authors employing a numerical model showed that by applying a pressure difference across the membrane, the flux of reactant and product can be directed preferentially to the permeate side of the membrane [Veldsink *et al.*, 1992; Sloot *et al.*, 1990].

In this CMR configuration, the reactants are fed to opposite sides of the catalytic membrane (segregation of reactants), such that the highly exothermic chemical reaction takes place inside the membrane while the products may diffuse out through both sides of reactor. Specifically, a narrow reaction zone is formed within the membrane which is capable of maintaining strict stoichometry via reaction and diffusion phenomena. If the rate of reaction is faster than diffusion, there will be an increase in molar fluxes of reactant species. If the permeation rate of species is faster than reaction rate, there will be an increase in

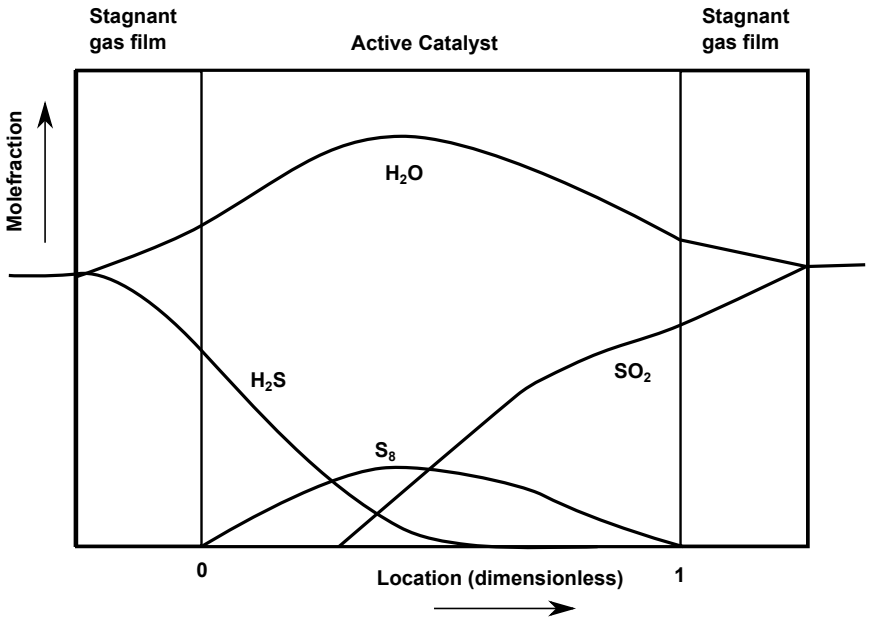

Figure 1.17: Typical concentration profiles inside the catalyst in a CMR for Claus reaction [Sloot *et al.*, 1990].

rate of reaction. Thus, the molar ratio of reactants will always remain strict stoichiometric ratio. Figure 1.17 shows typical concentration profiles inside the catalyst in a CMR for Claus reaction.

Segregation of reactants to opposite sides of catalytic membrane is also investigated for consecutive and parallel reactions to enhance the intermediate desired product yield and demonstrated that it can prevent the crossover of reactants to either side of membrane. Saracco et al. [Saracco and Veldsink, 1995b,a] conducted a pilot plant study for the combustion of propane in a CMR with segregated reactants in presence and absence of trans-membrane pressure gradients. They employed a porous alumina tube membrane activated by inserting Pt/γ-Al_2O_3 catalyst and studied the operating conditions for optimal performance of the reactor. They further demonstrated that application of pressure difference over the membrane increases the conversion up to 300%.

Harold et al. [Harold *et al.*, 1993] used a CMR to study a consecutive-parallel reaction

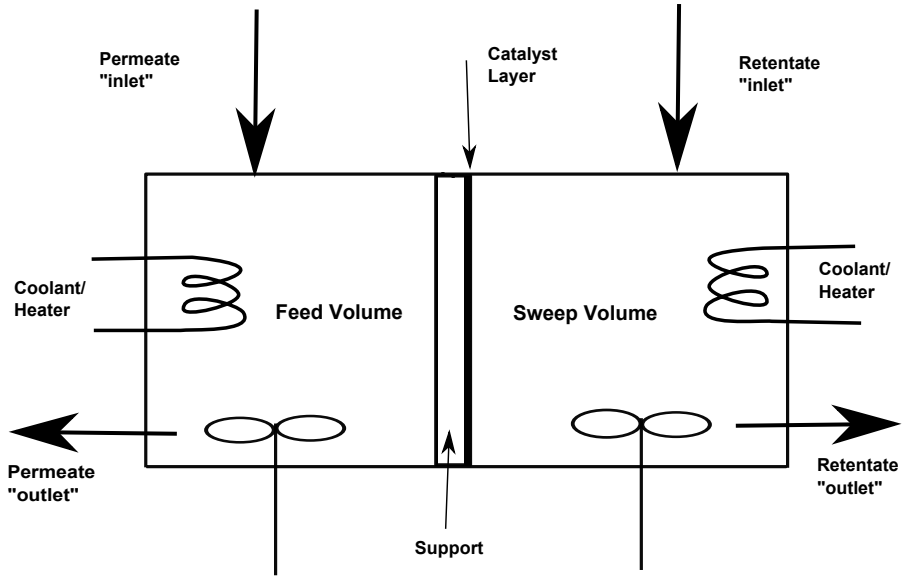

Figure 1.18: Schematic of a catalytic membrane reactor (CMR) model, taken from [Harold *et al.*, 1993; Harold and Lee, 1997]

in which intermediate species is a desired product. They specifically focused on modeling CMR for a case of parallel reaction in the following form:

$$\begin{aligned} A + \vartheta_B B &\longrightarrow \vartheta_{R1} R \; ; \; r_1 = k_1 p_A^{\alpha_{A1}} p_B^{\alpha_B} \\ A + \vartheta_{R2} R &\longrightarrow \vartheta_P P \; ; \; r_2 = k_2 p_A^{\alpha_{A2}} p_B^{\alpha_R} \end{aligned} \tag{1.17}$$

They studied different conditions that can potentially enhance the intermediate product (R) yield using the segregation of reactants A and B. It was concluded that reactant segregation can have significant effect on the intermediate product yield when these three requirements are met, i) $\alpha_{A1} < \alpha_{A2}$, ii) k_1 and k_2 are sufficiently large and iii) catalytically active layer is sufficiently thinner than the support layer.

Harold and Lee in [Harold and Lee, 1997] have shown that both reactant conversion and intermediate yield are sensitive to the degree of segregation as well as, (i) the intrinsic kinetics, catalytic activity and apparent order of the reactions, (ii) The degree of mixing

(as shown in Figure 1.18) of the reactants between the feed and sweep chambers. This is dependent on the characteristic flow, transmembrane diffusion and reaction time, (iii) the proximity of the reactants tot the catalytically active layer, and (iv) the stoichiometries of the two reactions and the relative extent of the reaction.

It is evident from the above discussion that CMRs with segregated reactants offer several advantages. In this thesis, CMR concept is extended for gas separation without employing any permselective materials. The following section describes the modeling of membrane reactors.

1.9 Modeling of membrane reactors

Theoretical modeling of membrane reactors involves mathematically describing the retentate, permeate and the catalyst volumes employing appropriate design equations. Permeate and retentate volumes are described by using plug flow or mixed flow equations. A general model describing membrane reactors can be found in [Marcano and Tsotsis, 2002]. The following sections detail the diffusion models used to describe the gas transport in porous membranes.

1.9.1 Gas transport in porous membranes

Porous membranes are classified according to their pore diameter as (a) macroporous for pore diameter > 50 nm, (b) mesoporous pore diameter between 2 nm, 50 nm, and (c) microporous for porediameter < 2 nm. The gas transport mechanism is dependent on pore diameter (d_p) and free mean path of gas molecules (l). The viscous and Knudsen transport mechanisms can be distinguished using Knudsen number defined as, $K_n = d_p/l$ [Hoff and Poplsteinova, 2002].

i) Molecular diffusion or viscous flow, when $K_n < 1$

ii) Knudsen diffusion, when $K_n > 1$

iii) Molecular sieving effect, when diameter of molecule = diameter of pore.

These transport mechanisms are illustrated in Figure 1.19 [Hoff and Poplsteinova, 2002].

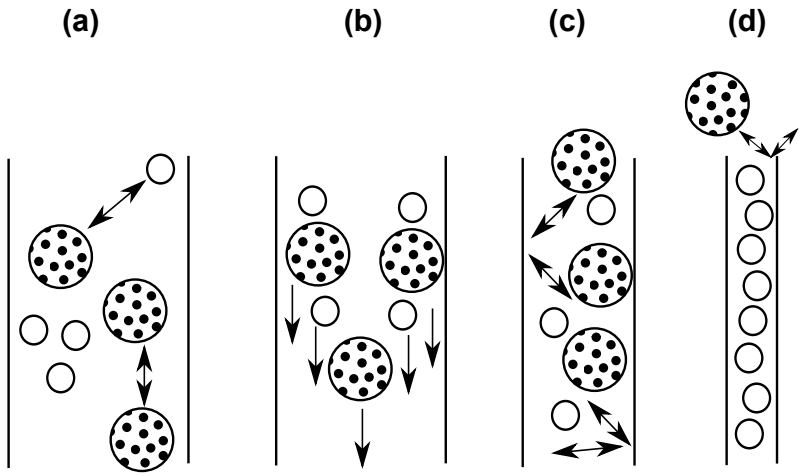

Figure 1.19: Gas transport mechanism in porous media, (a) molecular diffusion, (b) Viscous diffusion (c) Knudsen diffusion (d) Molecular sieving.

1.9.1.1 Molecular diffusion

Molecular diffusion dominates gas transport through a porous media when the pore diameter is much greater than free mean path of molecules, such that molecular collisions occur predominantly between to unlike molecules. The resulting exchange of species-specific momentum is described using an effective binary diffusivity for each gas pair, which is modified by the tortuosity and porosity of the porous material.

$$D_{ij}^{eff} = \frac{\varepsilon}{\tau} D_{ij} \tag{1.18a}$$

where D_{ij} is the binary diffusivity of the gas species i in j ($m^2\,s^{-1}$), ε is the tortuosity of the material and τ is the porosity of the material.

The binary diffusivity D_{ij} can be determined from kinetic theory of gases (a detailed derivation by Taylor and Krishna can be found in [Taylor and Krishna, 1993]) and can be written as follows:

$$D_{ij} = \frac{CT^{3/2}\left(\frac{1}{M_i}+\frac{1}{M_j}\right)^{1/2}}{P\sigma_{ij}^2\Omega_D} \tag{1.18b}$$

where the value of C is 1.88×10^{-2}, σ is the characteristic length (Å), P is the pressure (Pa), Ω_D is the diffusion collision integral, and M_i is the molecular weight of component i ($g\,mol^{-1}$). The diffusion collision integral is a function of k_BT/ε, where k_B is the Boltzmann constant and ε is the molecular energy parameter. The values of these parameters for different gas components are well documented [Bird *et al.*, 2007; Taylor and Krishna, 1993].

There are a number of semi-empirical correlations for estimating the gaseous diffusion coefficients, the method of Wilke and Lee [Taylor and Krishna, 1993] is given by,

$$C = 0.02199 - 0.00507\sqrt{\frac{1}{M_i}+\frac{1}{M_j}} \tag{1.18c}$$

A more commonly recommended semi-empirical correlations developed by Fuller and Giddings [Fuller *et al.*, 1966] as detailed in [Geankoplis, 1993; Taylor and Krishna, 1993] is as follows:

$$D_{ij} = \frac{1.013\times10^{-7}T^{1.75}\left(\frac{1}{M_i}+\frac{1}{M_j}\right)^{1/2}}{P\left[\left(\sum v_i\right)^{1/3}+\left(\sum v_j\right)^{1/3}\right]^2} \tag{1.18d}$$

where $\sum\vartheta_i$ and $\sum\vartheta_j$ are the sum of structural volume increments, M_i and M_j are molecular weights of species i, j, P is the total pressure, (atm), T is the temperature of the system (K).

Fairbanks and C.R. Wilke in 1950 [Fairbanks and Wilke, 1950] proposed an equation for evaluating the diffusivity of each species in a gas mixture, it is as follows:

$$D_{i,m} = \frac{1 - y_i}{\sum_{j=1, j\neq i}^{n} \frac{y_j}{D_{ij}}} \tag{1.18e}$$

where, D_{ij} is the binary diffusivity of species i and j, $y_{i,j}$ is the mole fraction of species i, j.

The mass flux of gas species for the case of a binary mixture, using Fick's law of diffusion can be written as follows:

$$J_i = \frac{-D_{i,m}^{eff}}{RT} \frac{\partial \left(y_i P\right)}{\partial z} \tag{1.18f}$$

where, J_i is the mass flux of species i (mol m^{-2} s^{-1}), D_{ij} is the binary diffusivity of species i (m^2 s^{-1}) and j, R is the ideal gas constant (J mol^{-1} K^{-1}), P is the total pressure (Pa).

1.9.1.2 Viscous flow

Viscous flow dominates when the effect of a gas viscosity become predominant due to the fluid-phase pressure gradient across the porous media [Krishna and Wesselingh, 1997]. While viscous flow does not contribute to the separation by the membrane, it plays an important role in fluid transport [Hoff and Poplsteinova, 2002]. The mass flux of the gas species can be described by Darcy's law which can be obtained from the Hagen-Poiseuille equation, can be written as follows:

$$J_v = -\frac{P}{RT} \frac{B_o}{\eta} \nabla p \tag{1.19a}$$

The permeability coefficient B_o for cylindrical pore can be determined using the following equation,

$$B_o = \frac{\varepsilon}{\tau}\frac{d_p^2}{32} \tag{1.19b}$$

where η is the viscosity of the gas species (Pa s), d_p is the pore diameter (m), τ is the tortuosity and ε is the porosity of the porous medium.

1.9.1.3 Knudsen diffusion

Knudsen diffusion dominates when the pore diameter of the material is comparable to that of free mean path of gas molecules. In this mechanism, the gas molecule collisions with pore walls dominate the collision between molecules, therefore the gas transport is directly related to the pore diameter.

Application of kinetic theory of gases to a single, straight and cylindrical pore, the Knudsen diffusion coefficient can be given by the following equations:

$$D_{i,K} = \frac{1}{3} d_{pore} \sqrt{\frac{8RT}{\pi M_i}} \tag{1.20a}$$

or it can be written in a more general form accounting for tortuosity and porosity of material as:

$$D_{i,K}^{eff} = \frac{1}{3}\frac{\varepsilon}{\tau} d_{pore} \sqrt{\frac{8RT}{\pi M_i}} \tag{1.20b}$$

The mass flux of gas species due to Knudsen diffusion can be written as follows:

$$J_{i,K} = \frac{-D_{i,K}^{eff}}{RT}\frac{\partial\left(y_i P\right)}{\partial z} \tag{1.20c}$$

1.9.1.4 Wilke-Bosanquet equations

The gas transport in the porous media can be described using either molecular diffusion, Knudsen diffusion or both combined. The molecular and Knudsen diffusions are combined in series to determine the overall diffusion coefficient. This can be given by:

$$\frac{1}{D_i^{eff}} = \frac{1-\alpha J_i}{D_{i,M}^{eff}} + \frac{1}{D_{i,K}^{eff}} \tag{1.21a}$$

where α is the ratio of molar masses given according to Graham's law, $1 - \frac{J_i}{J_j} = 1 - \sqrt{\frac{M_j}{M_i}}$. For an equimolar diffusion, α is zero and the above equation is transformed into an equation known as Wilke-Bosanquet law:

$$\frac{1}{D_i^{eff}} = \frac{1}{D_{i,M}^{eff}} + \frac{1}{D_{i,K}^{eff}} \tag{1.21b}$$

1.9.2 Gas transport models in porous media

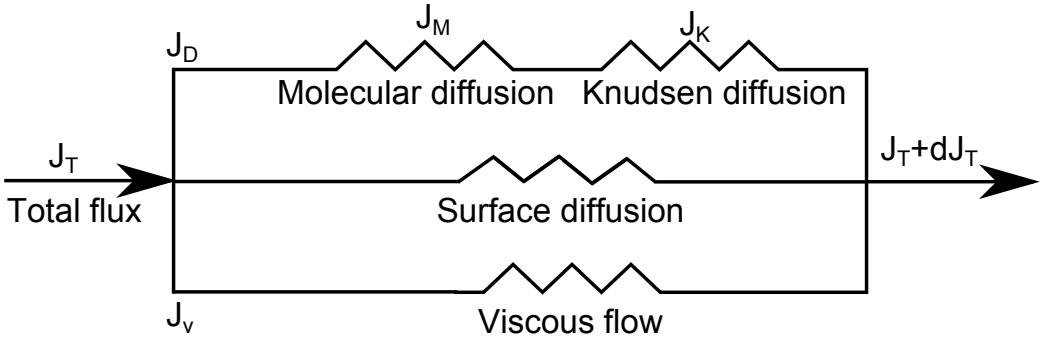

Figure 1.20: Gas transport in porous media illustrated as an electrical analog [Mason and Malinauskas, 1983].

The gas transport in porous medium can be described using three models: i) Ficks diffusion model (FM) [Fick, 1855], ii) Stefan-Maxwell multicomponent diffusion [Maxwell, 1866; Stefan, 1871] and iii) Dusty-Gas-Model [Mason and Malinauskas, 1983; Jackson, 1977]. Figure 1.20 shows the gas transport in porous media illustrated as an electric analog. These three models are briefly discussed here. A more thorough review on multicomponent diffusion can be found in [Taylor and Krishna, 1993; Krishna and Wesselingh, 1997].

1.9.2.1 Fick's diffusion model (FM)

The Fick's law of gas diffusion was developed by Adolf Fick in 1855 [Fick, 1855]. It is the simplest and the most commonly employed model to describe the gas transport in a porous media. The Fick's law postulates a linear dependence of flux with respect to average mixture velocity of each chemical species [Krishna and Wesselingh, 1997].

The Fick's law is strictly valid when the following conditions are met [Krishna and Wesselingh, 1997; Taylor and Krishna, 1993; Bird *et al.*, 2007]:

i) Diffusion of binary gas mixtures,

ii) Dilute gas diffusion in multicomponent mixtures,

iii) Absence of centrifugal or electrostatic force fields,

iv) The gas mixtures are thermodynamically ideal at low to moderate pressures.

This law can be written in the following form:

$$J_i = c_i\,(u_i - u) = -c_t D_{ij} \nabla y_i \tag{1.22a}$$

where u_i is the velocity of species i, u is the average velocity of gas mixture, c_i is the concentration of species i, and y_i is the mole fraction of species i.

The extended Fick's model which accounts for convective transport and diffusion of gas in porous media can be written as follows [Veldsink and Damme, 1995]:

$$J_i = \frac{1}{RT}\left(-D_{i,m}^{eff}\frac{\partial\left(y_i P\right)}{\partial z} + \frac{B_0 y_i P}{\mu}\frac{dP}{dz}\right) \tag{1.22b}$$

where, B_0 is the permeability of the porous media, $D_{i,m}^{eff}$ is the effective molecular diffusivity of a gas species, and μ is the viscosity of gas. When the pressure difference in the pores is insignificant, therefore, the convective term can be ignored. The above equation therefore transforms into the following equation.

$$J_i = \frac{-D_{i,m}^{eff}}{RT}\frac{\partial\left(y_i P\right)}{\partial z} \tag{1.22c}$$

1.9.2.2 Stefan-Maxwell Model (SMM)

Stefan-Maxwell diffusion equations for multicomponent systems takes into account the collisions between molecules of different species [Maxwell, 1866; Stefan, 1871] . These equations are named after Scottish physicist James Clerk Maxwell and Austrian scientist Josef Stefan, who were responsible for their development. The Stefan-Maxwell model neglects the Knudsen diffusion term and the equation can be given by:

$$\sum_{j=1,j\neq i}^{n}\frac{y_j J_i - J_j y_i}{D_{ij}^{eff}} = -\frac{P}{RT}\frac{dy_i}{dz} \tag{1.23}$$

Where, J_i is the mass flux of species i, $D_{i,j}^{eff}$ is the effective binary molecular diffusivity of a gas species i and j, $y_{i,j}$ is the mole fraction of species i and j and P is the total pressure.

For convenience of numerical methods, SMM equations for n-component can be writ-

ten in matrix form as follows:

$$(J) = -c_t \left[B\right]^{-1} (\nabla x) \tag{1.24a}$$

where the (B^{-1}) is the matrix equivalent of effective diffusivity which can be determined from following equations,

$$B_{ii} = \frac{x_i}{D_{in}} + \sum_{k=1, i\neq k}^{n} \left(\frac{x_k}{D_{ik}}\right) \tag{1.24b}$$

$$B_{ij} = -x_i \left(\frac{1}{D_{ij}} + \frac{1}{D_{in}}\right) \tag{1.24c}$$

The SMM equations reduces to Fick's law for binary component diffusion for ideal gas transport in porous media, this can be demonstrated quite easily. SMM equation for binary component diffusion can be written as,

$$(J) = -c_t \left[B\right]^{-1} (\nabla x) \tag{1.25}$$

For component 1:

$$J_1 = -c_t B^{-1} \nabla y_1 \tag{1.26}$$

where $\left[B\right]^{-1}$ is equal to binary diffusivity D_{12}. It can be easily inferred that Eq. 1.26 is same as that of Fick's law for binary diffusion for component 1. Fick's diffusivity and Maxwell-Stefan diffusivity are related as $B^{-1}\Gamma = D$, where the term Γ is the thermodynamic nonideality. For ideal system, the nonideality constant is unity, thus Fick's diffusivity and Maxwell-Stefan diffusivity are equal [Taylor and Krishna, 1993].

1.9.2.3 Dusty-Gas-Model (DGM)

Dusty-Gas-Model which accounts for molecular diffusion, Knudsen diffusion and viscous flow was developed independently multiple times [Hoff and Poplsteinova, 2002; Taylor and Krishna, 1993; Krishna and Wesselingh, 1997] by i) Deriagin and Bakanov in 1957, ii) Evans, Watson and Mason in 1962, iii) Mason, Malinauskas and Evans in 1957 and iv) Mackey in 1971. This model is an application of Stefan-Maxwell diffusion equations. The model considers the porous media as composed of giant molecules (dust particles) that are uniformly fixed in the space and treated as one more component in addition to gas mixture in the frame of Stefan-Maxwell approach. The DGM equations are given by the following form:

$$\frac{J_i}{D_{i,K}^{eff}} + \sum_{j=1, j\neq i}^{n} \frac{y_j J_i - J_j y_i}{D_{ij}^{eff}} = -\frac{1}{RT}\left(P\frac{dy_i}{dz} + y_i \frac{dP}{dz}\left(1 + \frac{B_o P}{D_{i,K}^{eff}\mu}\right)\right) \tag{1.27}$$

where, B_0 is the permeability of the porous media, $D_{i,j}^{eff}$ is the effective binary molecular diffusivity of gas species, μ is the viscosity of gas, $D_{i,K}^{eff}$ is the effective Knudsen diffusivity, $y_{i,j}$ is the mole fraction of species i and j, P is the total pressure.

It is also reported that the dusty-gas-model can be extended to also include thermal diffusion effects, non-ideal fluid flow behavior, surface diffusion and selective viscous flow [Taylor and Krishna, 1993; Hoff and Poplsteinova, 2002; Bird *et al.*, 2007].

1.10 Thesis scope and approach

The primary goal of this research is to explore the hypothesis that high hydrogen selectivities (separation) can be achieved using catalytic membranes without employing any hydrogen permselective material. This concept is demonstrated in two catalytic membrane designs, (1) a design for water-gas-shift reaction (Chapter 2) and (2) a design for hydrogen extraction from ethanol steam reforming (Chapter 4). The first design of water

gas shift catalytic membrane establishes a clear rubric of design rules that can be used to achieve permselective removal of hydrogen from a single reaction. Experiments are conducted to demonstrate the water-gas-shift CMR model using a modified gas permeation experimental system. A porous stainless steel (PSS) tube coated with catalyst active for water-gas-shift reaction is used as the substrate for the experiment. The experimental results demonstrating the water-gas-shift CMR is presented in Chapter 3. The water-gas-shift CMR design rules are then used for designing catalytic membrane for extraction of hydrogen from bioethanol (16 mol% ethanol) steam reforming through composite catalytic membrane using multiple catalytic layers, active for one or more reactions. In subsequent designs, addition of catalytic layers for exothermic oxidation reactions or application of external thermal gradients is also investigated to achieve the auto-thermal catalytic membrane reactor.

2. DESIGN OF WATER-GAS-SHIFT CATALYTIC MEMBRANE REACTOR*

2.1 Introduction

This chapter presents a theoretical design of catalytic membrane reactor with a single catalyst layer active for water-gas-shift reaction of a typical diesel reformate gas mixture (CO 9 mol%, CO_2 3 mol%, H_2 28 mol%, H_2O 15 mol%). The design rules developed in this chapter will be used in Chapter 4 for designing composite catalytic membrane reactor for bioethanol reforming.

The proposed single catalytic membrane layer design for water-gas-shift reaction is shown in Figure 2.1. The simulated gas mixture is fed to the retentate volume and pure steam is fed to the permeate volume. The segregation of pure steam to permeate side of catalytic membrane maintains a high equilibrium conversion of CO to H_2 and allows manipulation the reaction zone in the catalyst. The steam to carbon ratio is maintained 9:1 to maintain excess steam for shifting the equilibrium. The external pressure difference across the membrane is not applied, thus, the focus of the study is solely on manipulating diffusion phenomena and neglect the convectional transport of gas species. This catalytic membrane reactor is also operated in counter current flow mode to maintain high concentration driving force along the length of membrane.

Simulation results indicate that apparent CO:H_2 permselectivities of 90:1 to $>$ 200:1 at H_2 recoveries of 20% to up to 40% may be achieved through appropriate design. A parametric analysis identified two design criteria, i) Thiele modulus = 7.6, and ii) separation factor $<$ 0.4. Adiabatic and isothermal simulations comparison indicated that accumula-

*Part of this chapter is reprinted with permission from "Theoretical investigation of a water-gas-shift catalytic membrane for diesel reformate purification" by Kuncharam, B.V.R. & Wilhite, B.A., 2013., AIChE Journal, p.n/a-n/a., http://doi.wiley.com/10.1002/aic.14188

tion of reaction heat reduces the apparent permselectivities, it is shown this reduction can mitigated by external imposition of a countering thermal gradient.

2.2 Theoretical

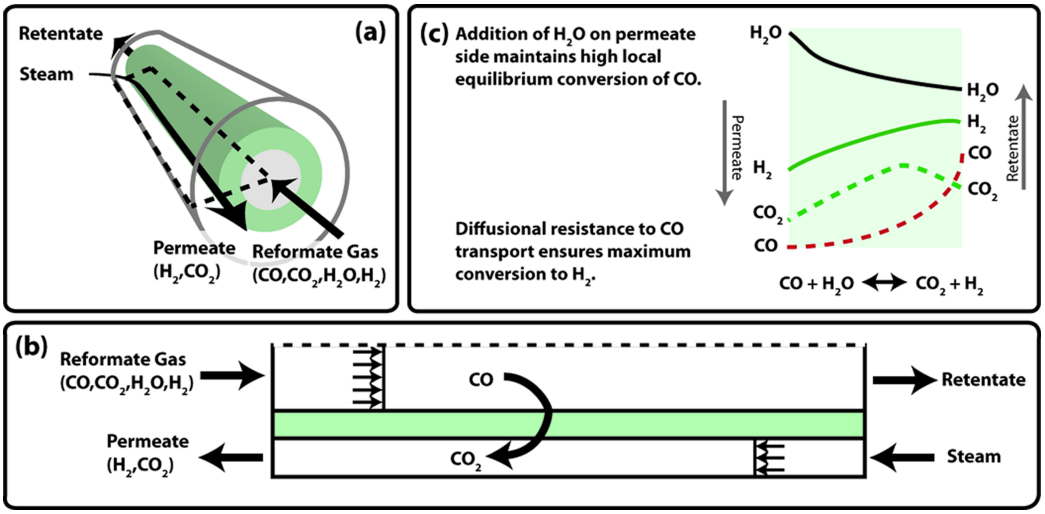

Figure 2.1: Schematic of water-gas-shift catalytic membrane reactor.

2.2.1 Model description and assembly

A steady state two dimensional model is formulated to describe the reaction, diffusion and heat conduction in the shell-tube catalytic membrane reactor describe above. The same model is used to study the isothermal and adiabatic performance of the catalytic membrane. Reaction and diffusion is described by single component Fick's diffusion model assuming Knudsen diffusion regime (nominal pore diameter of 10 nm).

$$\nabla^2 \left(D_{i,K}^{eff} C_i \right) = -r_i \tag{2.1a}$$

where

$$C_i = \frac{Px_i}{RT} \tag{2.1b}$$

The Knudsen diffusivities are obtained from kinetic theory of gases assuming a porosity of 45% and tortuosity of 2 [Neurock *et al.*, 1993], the effective Knudsen diffusivity is then estimated using

$$D_{i,K}^{eff} = \frac{\varepsilon}{\tau}\frac{d_p}{3}\left[\frac{8RT}{\pi M_i}\right]^{\frac{1}{2}} \tag{2.1c}$$

Heat conduction in the catalyst membrane is described by the following equation

$$\nabla\left(k_{cat}\nabla T^{cat}\right) = \left(-\triangle H_{rxn}^{o}\right)\left(-r_{CO}\right) \tag{2.2a}$$

where

$$k_{cat} = \varepsilon^2 k_{gas} + \left(1-\varepsilon\right)k_{solid} \tag{2.2b}$$

Water-gas-shift reaction is modeled using the power-law rate expression described by Mizsey et al. in [Mizsey *et al.*, 2001] for a CuO/Al_2O_3 (5% Copper on Alumina) catalyst, assuming a density of $1000\,\mathrm{kg\,m^{-3}}$.

$$r_{CO} = \delta \cdot k_f \left[p_{CO}^{cat} p_{H_2O}^{cat} - \frac{p_{CO_2}^{cat} p_{H_2}^{cat}}{K_{eq}}\right] \tag{2.3a}$$

where δ represents a catalyst activation factor. The rate constant and equilibrium constants are defined using the following equations.

$$k_f = 2.25 \times 10^{-3} exp\left[\frac{-50,000}{RT^{cat}}\right] \tag{2.3b}$$

$$K_{eq} = 9.543 \times 10^{-3} exp\left[\frac{-39,876}{RT^{cat}}\right] \tag{2.3c}$$

Retentate and permeate fluid volumes are modeled assuming perfect plug flow behavior with no axial dispersion and back mixing. Both volumes are assumed to isobaric and at a total pressure of 1 atm and temperature to be 773 K for the isothermal case.

One-dimensional plug flow models describing individual species molar flow along the axial length of the membrane are employed, assuming mass appearance in the bulk fluid volume occurs via gas-solid mass transfer. This is implemented with the following equations:

$$\frac{1}{A_C^F}\frac{dF_i^F}{dz} = -k_{gs}\tilde{a}^F\left(p_i^F - p_i^{cat}\right) \tag{2.4a}$$

$F_i^F = F_{i,o}^F$@ z=0

$$\frac{1}{A_C^S}\frac{dF_i^S}{dz} = -k_{gs}\tilde{a}^S\left(p_i^S - p_i^{cat}\right) \tag{2.4b}$$

$F_i^S = F_{i,o}^S$@ z=0.15

The fluid and catalyst volume models are linked through boundary conditions equating mass fluxes normal to the fluid-catalyst boundary of individual species, which is represented by Eq. 4.2c.

$$\left(\nabla D_{K,i}^{eff} C_i\right)\cdot\tilde{n} = k_{gs}\left(p_i^{F,S} - p_i^{cat}\right)M_i \tag{2.4c}$$

The thermal gradients in the catalyst and fluid volumes are studied with adiabatic system at 773 K and varying the average adiabatic temperature. The fluid-wall heat transfer at catalyst boundary to retentate and permeate volumes are described using equations 2.5a

and 2.5b.

$$\frac{\left(\sum C_{p,i} N_{i,o}^{F}\right)}{A_C^F} \frac{dT^F}{dz} = -h^F \tilde{a}^F \left(T^{cat} - T^F\right) \tag{2.5a}$$

with initial condition at $z = 0$, $T^F = T_o^F$,

$$\frac{\left(\sum C_{p,i} N_{i,o}^{S}\right)}{A_C^S} \frac{dT^S}{dz} = -h^S \tilde{a}^S \left(T^{cat} - T^S\right) \tag{2.5b}$$

with initial condition at $z = 0.15$, $T^S = T_o^S$.

The fluid-wall heat transfer coefficient for Reynold's number between 40 and 2000 is defined by Eq. 2.6a [Dixon and Cresswell, 1979].

$$Nu_{fw} = \frac{h_{fs} d_p}{k_g} = 0.24 Pr^{1/3} Re^{0.8} \tag{2.6a}$$

Where the Reyond's number (Re) and Prandtl number (Pr) are defined as

$$Re = \frac{d_t \rho u}{\mu_{mix}} \tag{2.6b}$$

and

$$Pr = \frac{C_{P,mix} \mu_{mix}}{k_{cat}} \tag{2.6c}$$

respectively.

The dynamic viscosity of the gas mixture is evaluated using the semi-empirical formula developed by C. R. Wilke in [Wilke, 1950].

$$\mu = \sum \frac{x_i \mu_i}{x_i + \sum x_j \varphi_{ij}} \tag{2.6d}$$

where

$$\varphi = \frac{\left[1 + \left[\frac{\mu_i}{\mu_j}\right]^{\frac{1}{2}} \left[\frac{M_j}{M_i}\right]^{\frac{1}{4}}\right]^2}{\sqrt{8}\left[1 + \frac{M_i}{M_j}\right]^{\frac{1}{2}}} \tag{2.6e}$$

and

$$\mu_i = 2.67 \times 10^{-5} \frac{\sqrt{M_i T}}{\sigma^2 \Omega_\mu} \tag{2.6f}$$

in which Lennard-Jones parameters are taken from [Bird *et al.*, 2007].

2.2.2 Design parameter & specifications

A comprehensive two dimensional model is developed to describe the above shown shell-and-tube catalytic membrane reactor in counter current mode with a tube inner radius of 4.75 mm and shell outer radius calculated based on catalytic membrane thickness ensuring identical retentate and permeate volumes with tube length of 0.15 m. Catalyst dilution factor and thickness are selected such that membrane performance is investigated over a range of modified Thiele modulus (Φ) and separation factor (ζ). The catalyst membrane performance is then simulated over a range of dimensionless Damkohler number (varying the feed flow rates).

The normalized Thiele modulus is determined from Eq. 2.7 employing shape-and 2$^{\text{nd}}$-order kinetics normalizations following Aris [Aris, 1975] and accounting for reaction reversibility following Carberry [Carberry, 1962]. This modified Thiele modulus represents a dimensionless ratio of the rate of CO reaction within the membrane to the permeation

rate of undesired permeate CO across the membrane.

$$\Phi = t_{cat}\left[\frac{r_o\left(p^F_{CO,o},T\right)}{D^{eff}_{CO}\,p^F_{CO,o}}\right]^{1/2}\left(\frac{1}{2}\right)\left(\frac{2}{3}\right)^{\frac{1}{2}}\left(\frac{K_{eq}+1}{K_{eq}}\right)^{\frac{1}{2}} \tag{2.7}$$

A dimensionless separation factor, ζ, is defined as the ratio of desired permeate hydrogen across the membrane to the rate of CO conversion by water-gas-shift reaction within the membrane,

$$\zeta = \frac{A_{mem}}{V_{mem}}\frac{\left(\frac{D^{eff}_{H_2}}{t_{mem}}\right)\left(\frac{p^F_{H_2,O}}{t_{mem}}\right)}{\eta_o r_o\left(p_{i,o},T\right)} \tag{2.8}$$

2.2.3 Simulation strategy

The model is simulated over a range of feed flow rates to predict the performance of membrane. The sweep flow rates are calculated such that steam to carbon ratio of 9:1 is maintained across the membrane. A dimensionless Damkohler number defined based on initial rate of water-gas-shift reaction and reactant residence time is given by Eq. 2.9.

$$Da = \left[\frac{\eta\left(\Phi\right) r_o\left(p^F_{CO,o},T\right)RT}{p^F_{H_2,o}}\right]\left[\frac{F^F_{CO,o}}{V^F}\cdot\frac{RT}{P}\right]^{-1} \tag{2.9}$$

2.3 Numerical solution

The resulting two-dimensional model was implemented using the commercial COMSOL Multiphysics v3.5 environment equipped with the Chemical Engineering Module, employing separate convection and conduction physics modules in 2-D radial symmetry mode to describe mass and heat transport within the catalyst volume. Separate coefficient-form PDE modules are employed to describe convective heat and mass transport in retentate and permeate volumes. Weak boundary form equations are used to describe the solid-fluid heat transfer at the boundaries. Finite element meshes employed in the present

work consisted of approximately 30,000 triangular elements, resulting in 4×10^5 degrees of freedom. All numerical solutions met overall and atomic mass balances within 0.01% error. Further refinement in mesh size resulted in negligible change in solution accuracy. Solutions were obtained using the prepackaged stationary Direct UMFPACK solver (v4.2) written by Timothy A. Davis, which employs an unsymmetric multifrontral method for solving sparse, unsymmetric linear systems [Davis, 2004, 1995]. All simulations were carried out on a Dell Precision Workstation T7500 with Intel® Xeon®CPU X5670 @2.93GHz equipped with 24GB of RAM, with a typical solution time of 1200 seconds.

2.4 Simulation results analysis

Simulation results at each Damkohler number are characterized in terms of metrics to evaluate the performance of catalytic membrane reactor as a gas purification system. The performance is characterized in terms of percentile hydrogen recovery and effective apparent gas permselectivities. These effective gas permselectivities are compared to reference gas permselectivities that can be achieved in an infinite packed bed reactor for (I) when the feed compositions are allowed to reach equilibrium and (II) when feed and sweep gas compositions are blended and allowed to reach equilibrium. The performance of catalytic membrane as a conventional reactor is characterized in terms of overall carbon monoxide conversion which is then compared to the equilibrium conversion that can be achieved in an infinite packed bed reactor. Three reactor configurations are presented in Figure 2.2. These unique metrics provide an appropriate comparison of the performance of catalytic membrane to traditional catalytic membrane and packed-bed reactor designs for the purpose of CO removal from reformate mixtures. Table 2.1 presents summary of the unique performance metrics.

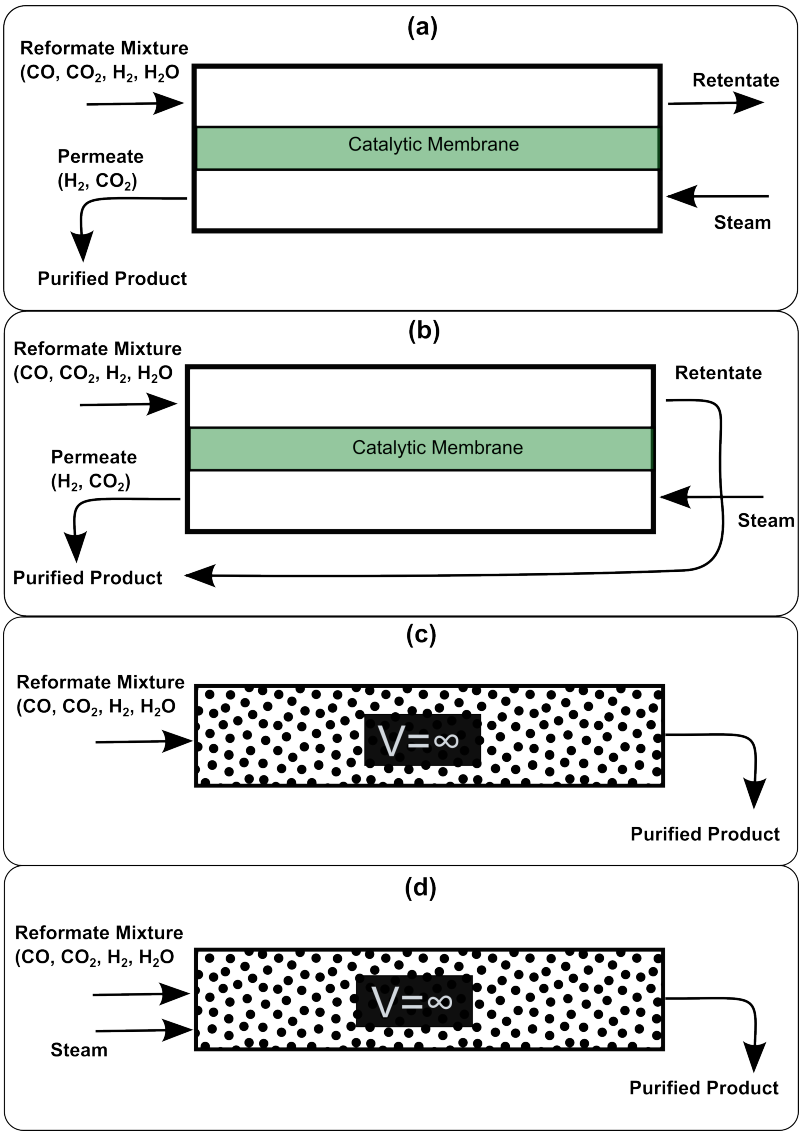

Figure 2.2: Schematic presenting the different configurations of reactors studied in this study.

Table 2.1: Definitions of performance metrics used in the present study.

Performance metric	Definition
CO Conversion	$X_{CO} = \frac{F^F_{CO,o} - \left(F^F_{CO,e} - F^S_{CO,e}\right)}{F^F_{CO,o}}$
GPM mode H_2/CO permselectivity	$S^{GPM}_{H_2/CO} = \left[\frac{F^S_{H_2,e}}{F^S_{CO,e}}\right] / \left[\frac{F^F_{H_2,e}}{F^F_{CO,e}}\right]$
PBR H_2/CO permselectivity	$S^{GPM}_{H_2/CO} = \left[\frac{F^{I,II}_{H_2,e} + X^{I,II}_{CO,eq} \cdot F^{I,II}_{CO,o}}{F^{I,II}_{CO,o} - X^{I,II}_{CO,eq} \cdot F^{I,II}_{CO,o}}\right] / \left[\frac{F^{I,II}_{H_2,o}}{F^{I,II}_{CO,o}}\right]$
Hydrogen Recovery (HR)	$HR = \frac{F^S_{H_2,e}}{F^F_{H_2,e} + F^S_{H_2,e}} \times 100$

2.5 Results and discussion

2.5.1 Initial design case $\zeta = 0.1$ and $\Phi = 7.6$ at 773 K

Simulations were first carried out for the design case corresponding to $\zeta = 0.1$, $\Phi = 7.6$ at 773 K. This initial design conditions are selected as a first approximation to establish the design criteria and provide insight into further parametric analysis. Thiele modulus of 7.6 corresponds to an estimated 99.9% of theoretical maximum modification of species partial pressure via reaction at the centerline, while the separation factor is selected such that water-gas-shift reaction is the dominant phenomena within the membrane system. Figure 2.3 presents the overall carbon monoxide conversion achieved in the catalytic membrane reactor as a function of Damkohler number, Da. The equilibrium carbon monoxide conversion corresponding to feed (reformate) composition ($X^I_{CO,Eq} = 0.474$) and a blend of reformate and sweep gases ($X^{II}_{CO,Eq} = 0.875$) are provided for reference. As Da increases from zero, carbon monoxide conversion rapidly increases towards the upper limit of $X^{II}_{CO,Eq}$, followed by a moderate reduction in conversion with further increases in Da

before returning to the upper limit of $X^{II}_{CO,Eq}$. This local reduction in CO conversion at intermediate values of Da is the result of axial mass dispersion within the catalytic film which dilutes the driving force for water-gas-shift reaction. This is illustrated in Figure 2.4 which presents contour maps of CO and H_2O partial pressures at increasing values of Da. Inspection of volume integrals and maximum values of water-gas-shift rates confirm a reduction of overall reaction rate owing to increased diffusive mixing at intermediate values of Da. Figure 2.3 also identifies a first operating point [†] at which carbon monoxide conversion within the catalytic membrane reactor is equal to the equilibrium conversion corresponding to the reformate composition ($X^{I}_{CO,Eq}$). Thus, at operating point [†], the CO conversion achieved by the catalytic membrane reactor is equal to that expected for reference case II.

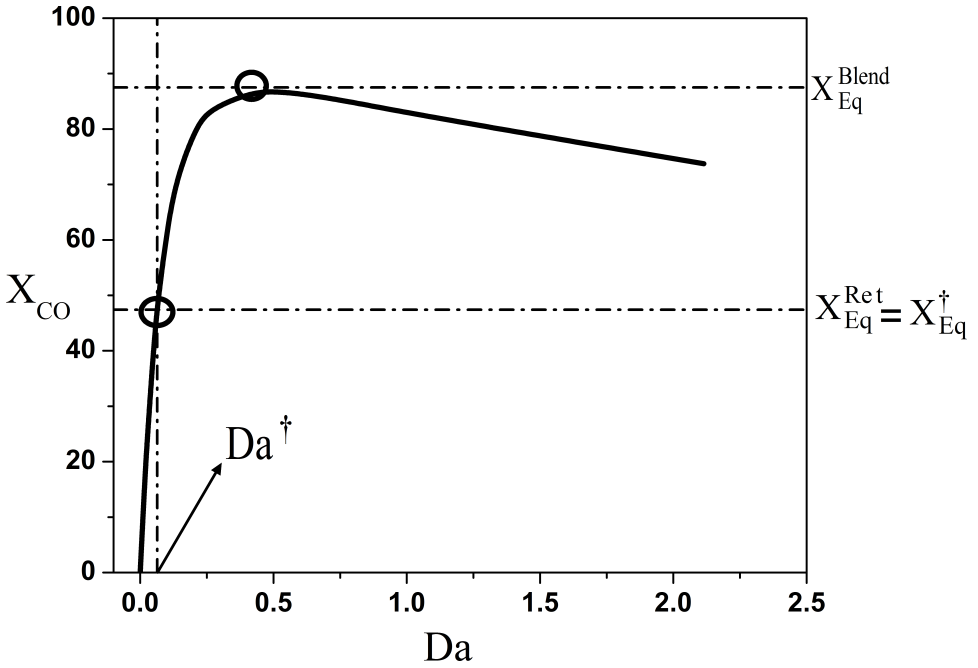

Figure 2.3: Carbon monoxide overall conversion vs. Da for water-gas-shift catalytic membrane reactor at $\Phi = 7.6$, $\zeta = 0.1$.

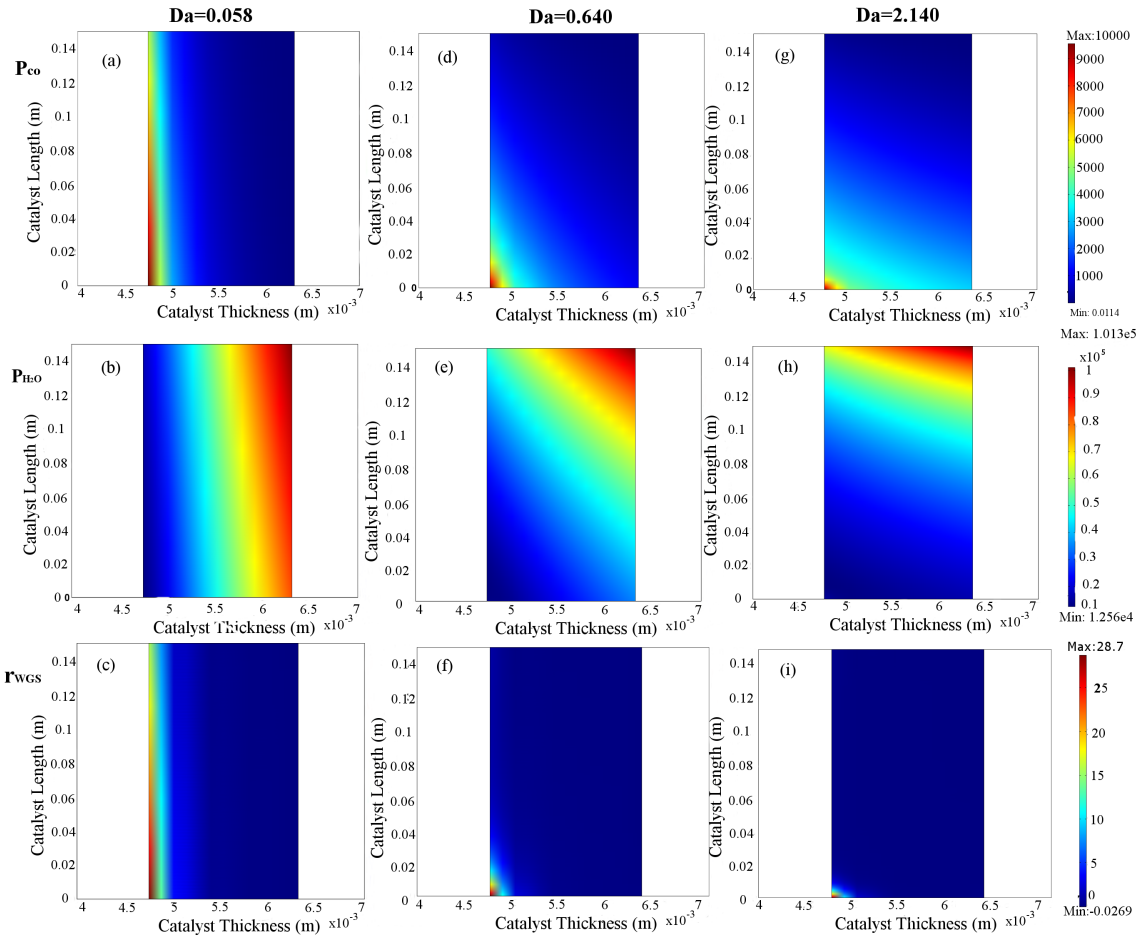

Figure 2.4: Influence of increasing residence time upon mixing in the catalytic membrane, $\Phi = 7.6$, $\zeta = 0.1$. At (a-c) Da = 0.058, (d-f) 0.640 and (g-i) 2.140, (a,d,g) CO partial pressure, (b,e,h) H_2O partial pressure and (c,f,i) local rate of water-gas-shift reaction are plotted as function of position within the catalytic membrane.

Figure 2.5a presents H_2:CO apparent permselectivities based upon the permeate effluent composition for the design case of $\zeta = 0.1$, $\Phi = 7.6$ at 773 K. At very high

flowrates (i.e., Da approaching zero), catalytic contributions to gas separation become negligible such that observed H_2:CO selectivity is equal to the inherent permselectivity of the catalytic film (3.3:1). Slight increases in Da result in significant increases of apparent H_2:CO permselectivity to a maximum value of 459:1 (shown in inset), followed by an asymptotic decline in selectivity towards the intrinsic Knudsen selectivity of the membrane ($S^K_{H_2/CO} = 3.3$) as Da approaches infinity. A second operating point [**] is identified corresponding to this maximum in achievable H_2/CO separation. Figure 2.5a further allows identification of a third operating point [*], corresponding to $S^{II}_{H_2/CO}$ = 10.22:1 at 773 K. This third operating point [*] thus represents the maximum Da at which the catalytic membrane reactor is capable of achieving greater CO mitigation in the product stream than a conventional packed-bed reactor. Figure 2.5b presents the blended H_2:CO apparent permselectivity as a function of Da. The observed trend in blended permselectivity matches that for carbon monoxide conversion, with a local maximum approaching the aforementioned limit of 10.22:1 coinciding with a maximum conversion approaching the upper limit of $X^{II}_{CO,Eq} = 0.875$.

Figure 2.6 presents the apparent H_2:CO_2 permselectivities based upon permeate effluent composition (GPM) and a blended composition of both retentate and permeate streams (CMR). In both cases, apparent permselectivities are consistently $<$1:1, owing to the generation of additional carbon dioxide via water-gas-shift reaction. It should be noted, however, that the gas purification mode of operation (i.e., H_2:CO_2 permselectivity based upon permeate gas composition) results in a higher ratio of H_2:CO_2 product partial pressures, as compared to the catalytic membrane reactor mode of operation (i.e., H_2:CO_2 permselectivity based upon blended effluent composition).

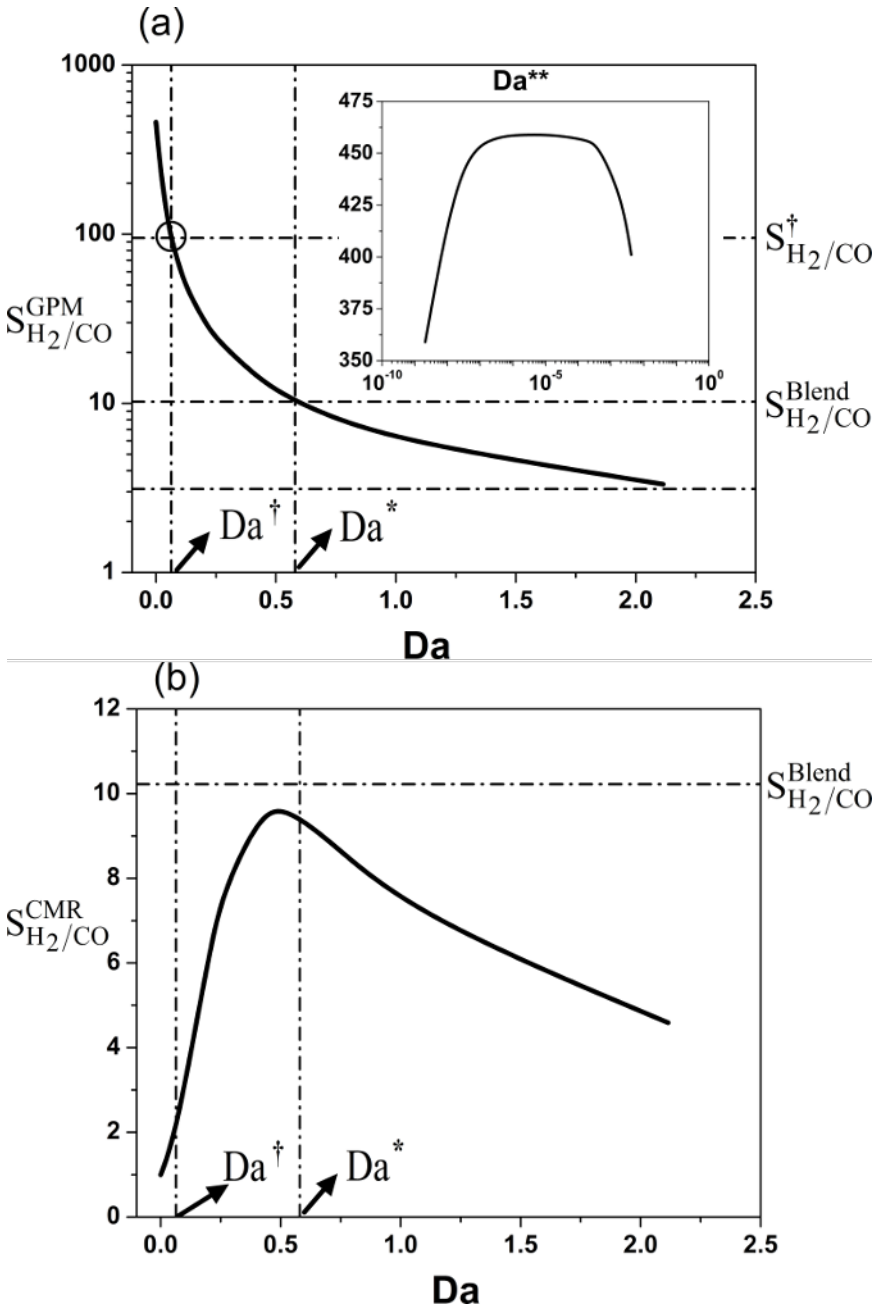

Figure 2.5: Apparent H_2:CO permselectivity based upon (a) permeate effluent composition, and (b) blended composition of retentate and permeate streams presented as a function of Da at $\Phi = 7.6$, $\zeta = 0.1$.

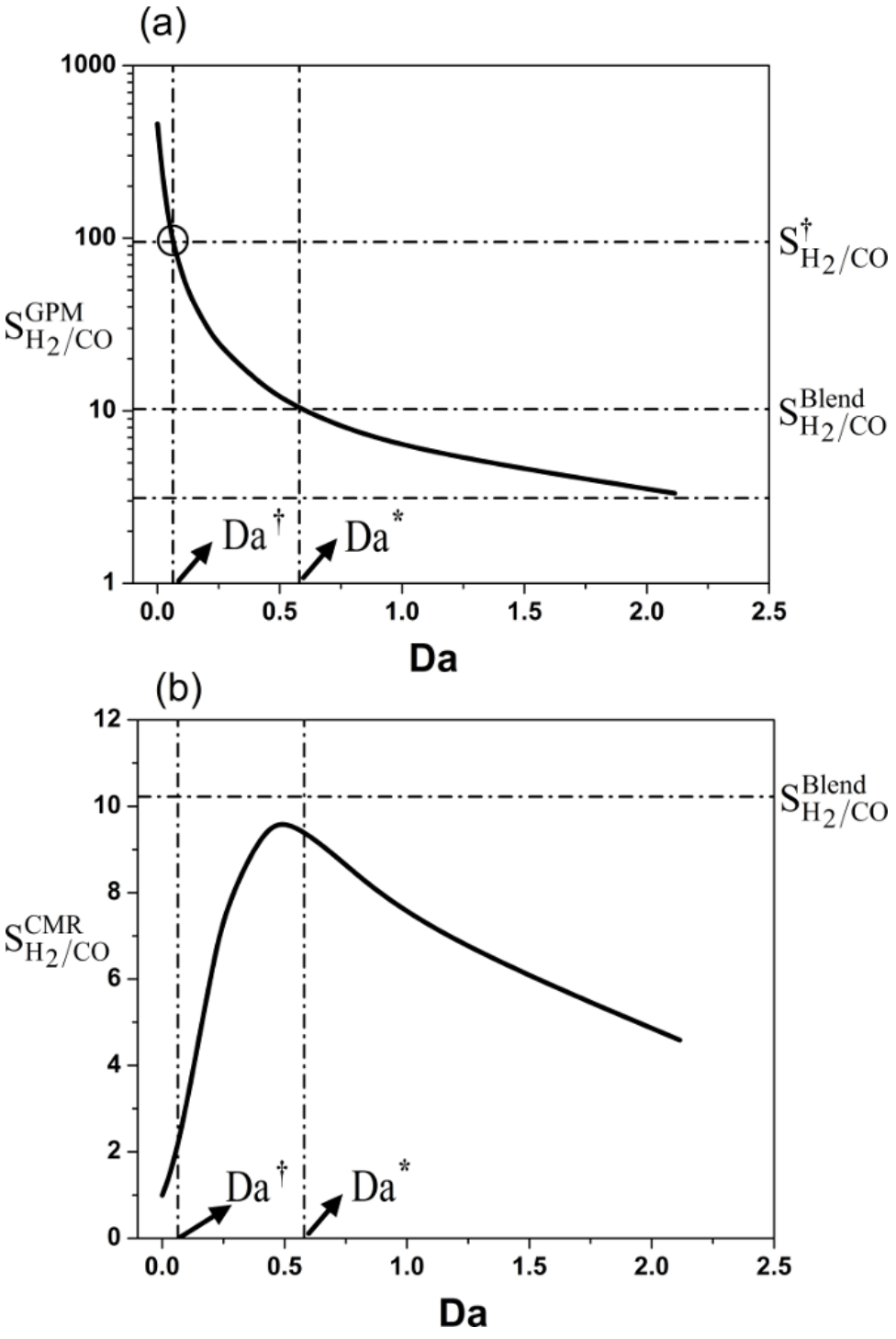

Figure 2.6: Apparent H_2:CO_2 permselectivity based upon (a) permeate effluent composition, and (b) blended composition of retentate and permeate streams presented as a function of Da at $\Phi = 7.6$, $\zeta = 0.1$.

Figure 2.7 summarizes the performance of the catalytic membrane system for gas purification by directly comparing H_2 recovery and apparent H_2:CO selectivity. The resulting curve is bounded by the intrinsic Knudsen permselectivity of the catalytic film (3.3:1) both as Da approaches zero (corresponding to HR approaching zero), and at Da approaching infinity, corresponding to HR = 66%. The three operating points identified in Figures 2.3 and 2.5 provide appropriate boundaries for identifying (I) an unfavorable region of operating space wherein greater removal of CO may be achieved using a conventional packed-bed reactor, (II) a region of high CO removal at the expense of low H_2 recovery, and (III) an intermediate region achieving a combination of favorable CO removal and H_2 recoveries. Based upon this analysis, an "optimal" operating point [†], corresponding to an overall CO conversion equal to the equilibrium conversion achievable with the reformate composition (i.e., $@X = X^I_{Eq}$), is selected as the most appropriate operating point for employing the catalytic membrane reactor as a gas purification membrane. For the case of $\zeta = 0.1$ and $\Phi = 7.6$, this design point corresponds to a hydrogen recovery of 24.3% at an apparent H_2:CO permselectivity of 94.7:1.

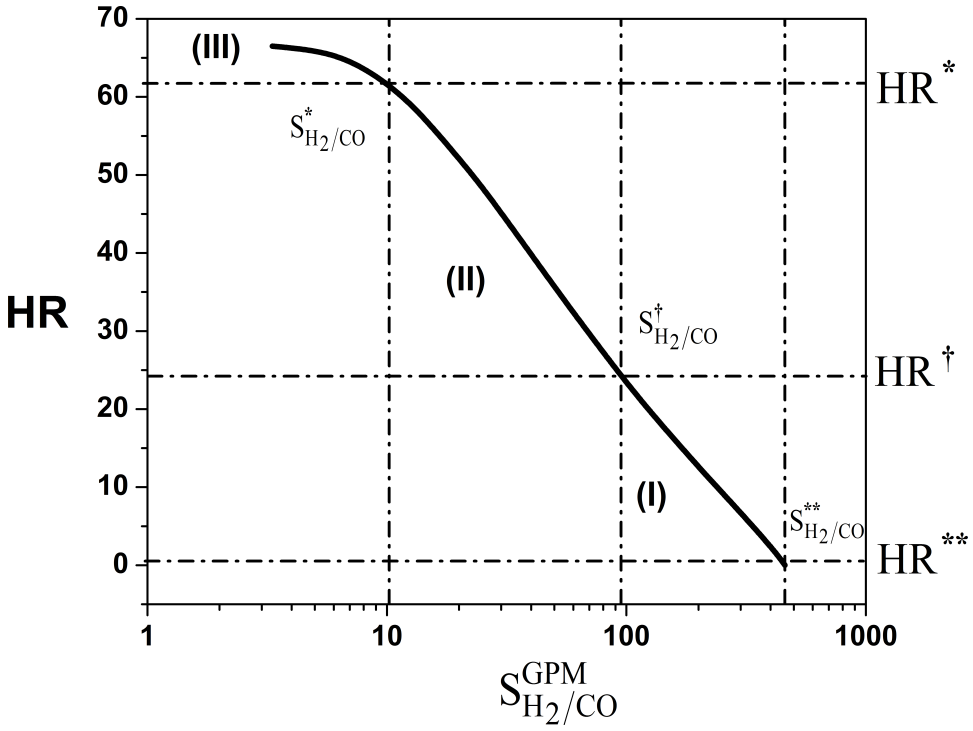

Figure 2.7: H_2 recovery vs. effective H_2:CO permselectivity, $\Phi = 7.6$, $\zeta = 0.1$.

Table 2.2: Summary of design parameters employed in the present study.

$\zeta = 0.1$		
Φ	t_{mem} (mm)	δ
7.6	1.56	0.23
5.24	1.32	0.13
2.99	1.01	0.086
2.5	0.96	0.077
2.3	0.89	0.065
1.7	0.77	0.048
1.3	0.68	0.036

$\Phi = 7.6$		
ζ	t_{mem} (mm)	δ
0.1	1.56	0.23
0.2	1.13	0.44
0.3	0.93	0.65
0.4	0.81	0.86
0.5	0.73	1.06
1	0.52	2.08
2	0.37	4.09
5	0.24	10.1
10	0.17	20.0

2.5.2 Comparison of CMR performance, varying ζ at $\Phi = 7.6$.

The above analysis is repeated for a sequence of membrane designs (summarized in Table 2.2) spanning separation factor (ζ) values of 0.1 to 10 while maintaining a constant value for Φ of 7.6. For each membrane design, performance is evaluated at each of the three design points discussed in Section 2.5.1.

Figure 2.8a presents the apparent H_2:CO permselectivity obtained under gas purification membrane mode of operation (GPM) as a function of separation factor, ζ. Two distinct regions ($\zeta < 0.4$, and $\zeta > 0.5$) are observed for the operating points corresponding to (**) a maximum in H_2:CO apparent permselectivity and (†) the aforementioned "optimal" operating point. Starting at the lowest value of $\zeta = 0.1$, negligible loss in permselectivity is initially observed with increasing ζ (increasing the hydrogen permeance relative to rate of water-gas-shift and/or carbon monoxide permeance) up to a limit of $\zeta < 0.4$. At values of $\zeta > 0.5$, apparent permselectivities are significantly reduced. For the case of the (*) operating point corresponding to CO removal by an infinite packed-bed reactor, selectivity remains constant as the latter value is not a function of ζ.

Figure 2.8b presents the percentile hydrogen recovery as a function of ζ for all three operating points. For the case of (*) and (†) operating points, slight increases in hydrogen recovery are observed with increasing ζ, which reflects a relative increase in hydrogen permeability. For the case of (**) operating point, a significant increase in hydrogen recovery is observed between $0.4 < \zeta < 0.5$, coinciding with a drop-off in corresponding maximum H_2:CO apparent permselectivity (Figure 2.8a). Overall, the results presented in Figure 2.8a confirm that the best gas purification performance is achieved by the (†) operating point under conditions wherein $\zeta < 0.4$.

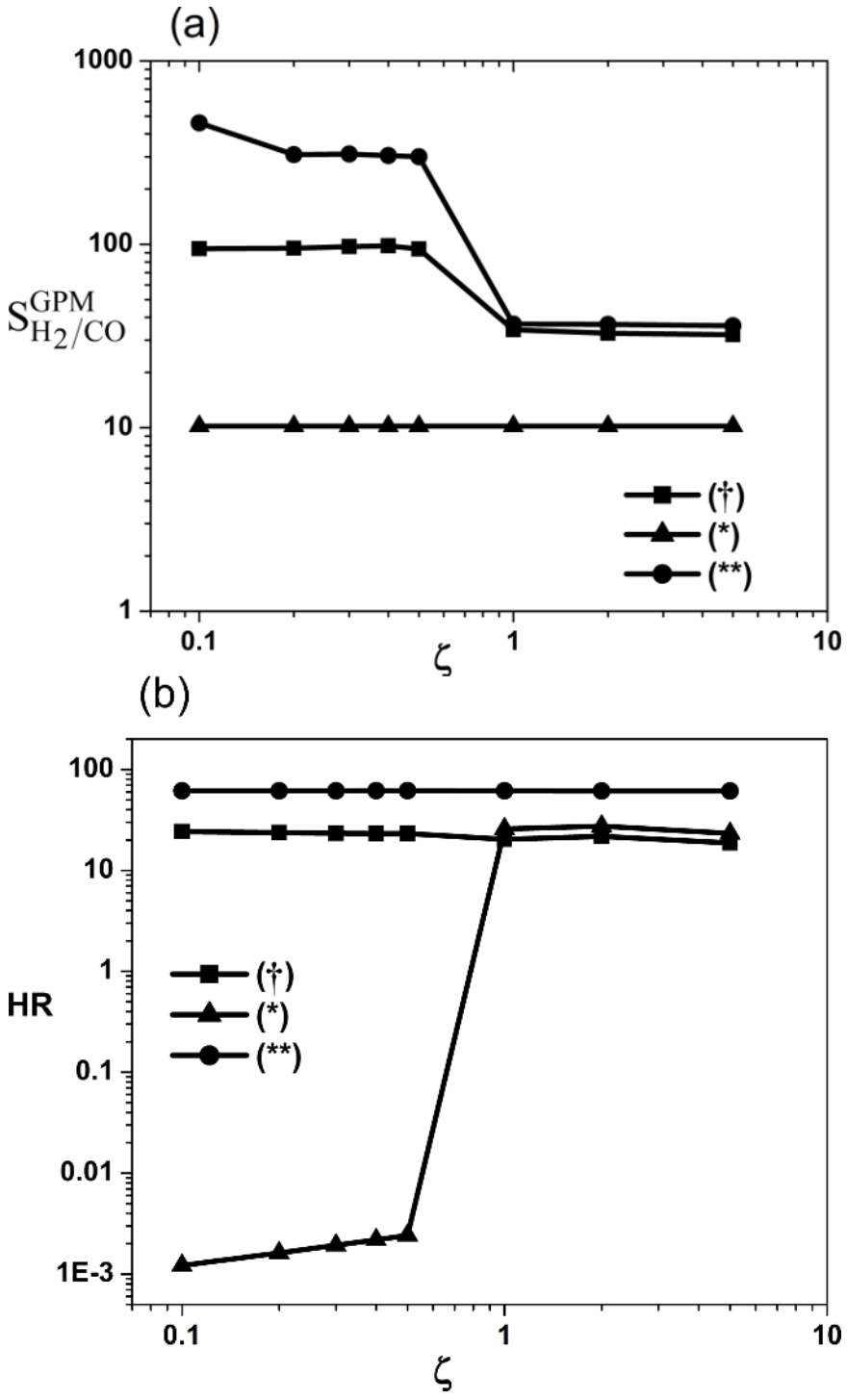

Figure 2.8: Comparison of membrane design performance at $\Phi = 7.6$, (a) Apparent H_2:CO permselectivity based on permeate effluent composition as function of ζ; (b) Hydrogen Recovery (HR) as function of ζ.

2.5.3 Comparison of CMR performance, Varying Φ at $\zeta = 0.1$.

Analysis is repeated for a sequence of membrane designs (summarized in Table 2.2) spanning normalized Thiele moduli (Φ) of 7.6 to 1 while maintaining a constant value of $\zeta = 0.1$, in terms of the three operating points discussed above.

Figure 2.9a presents the influence of decreasing Thiele moduli upon apparent H_2:CO selectivity at each operating point. As discussed above, the selectivity corresponding to an infinite packed bed (*) is invariant to the catalytic membrane design. The maximum (**) apparent selectivity decreases to a value of 10.2 (corresponding to the aforementioned reference case of an infinite packed bed) as Φ approaches unity, while the apparent selectivity corresponding to the (†) operating point falls below this minimum value at $\Phi < 1.5$. Figure 2.9b presents the influence of decreasing Thiele moduli (Φ) upon hydrogen recovery at $\zeta = 0.1$. Increasing trends in hydrogen recovery are observed for both (†) and (**) operating points, which indicates that as Thiele moduli is decreased, lower selectivities are achievable by the membrane as the impact of water-gas-shift reaction upon gas composition is reduced. This in turn alleviates the need for maintaining high concentration gradients across the membrane via low residence times (or values of Da), which limits hydrogen recovery rates. Thus, decreasing Thiele moduli results in poor maximum selectivities, which may nevertheless be achieved at higher residence times and therefore greater hydrogen recovery rates. Overall, the results in Figure 2.9 indicate that a design criteria of $\Phi = 7.6$ is sufficient to achieve high permselectivities for both (†) and (**) operating points, while further increases in Thiele moduli represent a diminishing return on selectivity at the cost of further reduction in recovery rates.

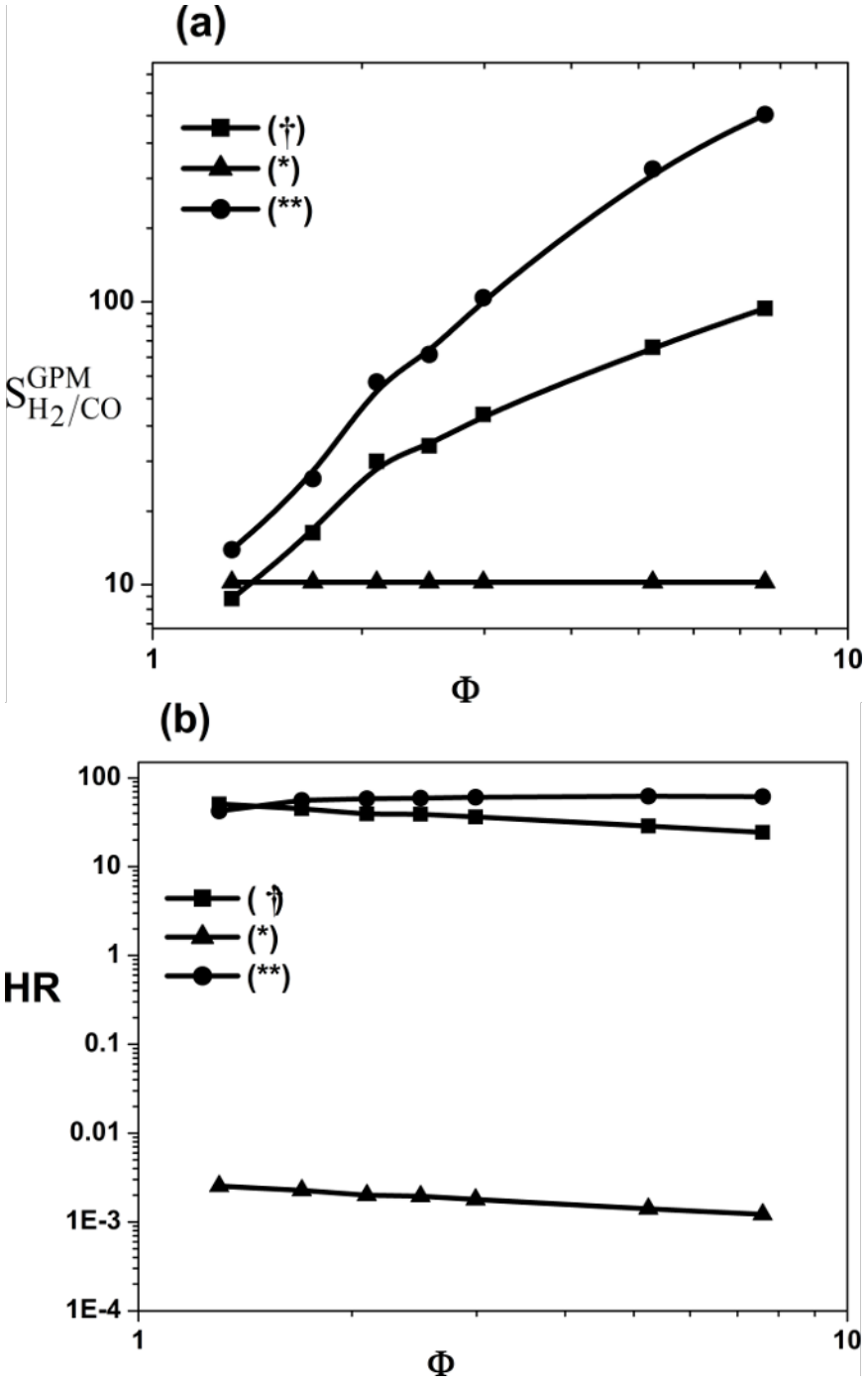

Figure 2.9: Comparison of membrane design performance at $\zeta = 0.1$. (a) Apparent H_2:CO permselectivity based on permeate effluent composition as function of Φ, (b) H_2 Recovery (HR) as function of Φ.

2.5.4 Comparison of isothermal CMR performance, varying temperature

Based upon the above analysis, a design point of ($\Phi = 7.6$, $\zeta = 0.1$) and the (†) operating point are selected as a basis for comparing catalytic membrane performance for gas purification over a range of five isothermal operating temperatures. Figure 2.10 shows the permeate hydrogen recovery versus apparent H_2:CO permselectivity obtained over a range of Da at each isothermal operating temperature studied. In all cases, hydrogen recovery and H_2:CO permselectivity follows the same trend discussed in Section 2.5.1. Permeate hydrogen recovery and apparent H_2/CO separation increase with decreasing temperature as reaction equilibrium shifts towards CO_2 and H_2 formation.

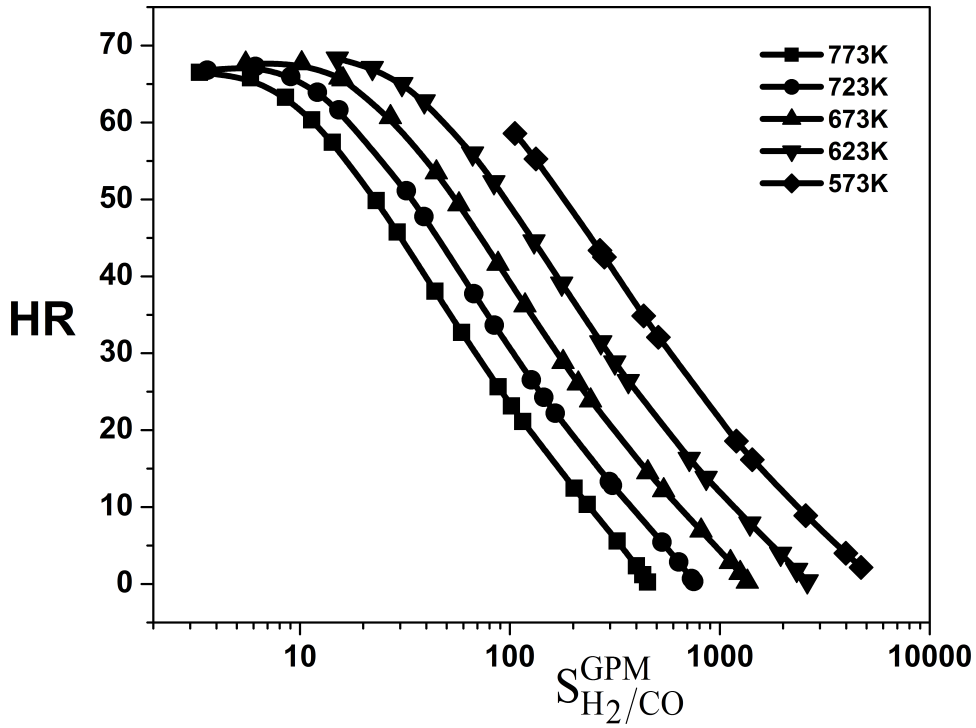

Figure 2.10: Comparison of GPM design performance as function of temperature at corresponding Damkohler number, Hydrogen recovery (HR) vs. effective H_2:CO permselectivity, $\Phi = 7.6$, $\zeta = 0.1$.

Table 2.3 summarizes both membrane dimensional design parameters (t, δ) and performance in terms of hydrogen recovery and apparent selectivities achieved by gas purification membrane operation mode (GPM) over the range of isothermal operating temperatures studied. The corresponding selectivities for the two infinite packed bed reactor cases are provided for comparison. Results indicate that as reaction temperature decreases, the achievable H_2:CO permselectivity increases owing to removal of equilibrium limitations upon the catalytic conversion of CO to CO_2. As reaction rates decrease with temperature, the residence time necessary to achieve sufficient reaction for design point (†) increases, which corresponds to an increase in hydrogen recovery rate. Thus, as temperature is decreased, both the H_2:CO apparent selectivity and H_2 recovery rate are improved.

Table 2.3: Summary of design parameters and results for varying temperature at $\Phi = 7.6$, $\zeta = 0.1$.

T (K)	t (mm)	δ	$S_{H_2/CO}$	$S_{H_2/CO}$	HR (%)
773.15	1.56	0.23	94.7:1	0.92:1	24.3
723.15	2.07	0.24	112.7:1	0.9:1	27.3
673.15	2.78	0.28	136.3:1	0.87:1	31.0
623.15	3.88	0.32	215:1	0.83:1	35.2
573.15	5.67	0.35	298.4:1	0.76:1	41.6

Table 2.4: Summary of membrane performance results for varying temperature at $\Phi = 7.6$, $\zeta = 0.1$.

	Feed (-)	Retentate (-)	Sweep (-)	Permeate (-)
y_{CO}	0.09	1.31×10^{-2}	0.0	2.22×10^{-4}
y_{CO_2}	0.03	9.25×10^{-2}	0.0	2.89×10^{-2}
y_{H_2}	0.28	2.23×10^{-1}	0.0	2.06×10^{-1}
y_{H_2O}	0.15	2.84×10^{-1}	1.0	6.45×10^{-1}

Further details of the (†) operating point for the design case of (573 K, $\Phi = 7.6$, $\zeta = 0.1$) are presented to provide additional assessment of this novel application of catalytic membranes to gas purification. For a catalytic membrane of 5.67 mm thickness and catalyst activity factor (δ) of 0.30, the apparent H_2:CO permselectivity is 298.4:1 at a H_2 recovery rate of 41.6%, with corresponding feed and effluent compositions summarized in Table 2.4. The Permeate gas produced with above conditions has a CO content of 0.022% and H_2 content of 20.6%, or 0.06% CO and 58% H_2 on a dry-gas basis. For a single tube-and-shell membrane with inner radius of 4.75 mm, outer radius of 10.42 mm and length of 150 mm, these conditions correspond to a feed (reformate) molar flowrate of 5.15×10^{-5} mol s^{-1} and sweep (steam) molar flowrate of 3.4×10^{-6} mol s^{-1} (Da = 0.1) at a hydrogen flux across the membrane of 8.49×10^{-4} mol H_2 per m^2 of membrane, or 0.038 mol H_2/s per kg of catalyst/membrane. Hydrogen compositions entering and exiting both permeate and retentate volumes allow determination of a log-mean driving force ($LMDP_{H_2}$) of 20 000 Pa, which combined with a membrane thickness of 5.67 mm yields an apparent hydrogen permeability of 2.37×10^{-10} mol m^{-1} Pa^{-1} s^{-1} and hydrogen permeance of 4.24×10^{-8} mol m^{-2} Pa^{-1} s^{-1}. This value compares favorably against that of palladium membranes, which are capable of typical hydrogen permeability of $\sim 2 \times 10^{-11}$ mol m^{-1} Pa^{-1} s^{-1} [Paglieri and Way, 2002; Gallucci *et al.*, 2013], which would require a thickness of 472 µm in order to achieve the equivalent hydrogen permeance predicted in this study.

2.5.5 Adiabatic operation: Influence of reaction heat and imposed thermal gradients

The performance of the catalytic membrane for gas purification was investigated under adiabatic conditions in order to ascertain the impact of reaction heat accumulation upon gas purification. Solutions to the adiabatic membrane reactor model detailed in Section

1.2 were obtained over a range of reactor Damkohler number for a membrane design corresponding to $\zeta = 0.1$ and $\Phi = 7.6$ at 773 K. Three adiabatic cases were studied; (i) membrane operation with matched feed and sweep inlet temperatures of 773 K, (ii) membrane operation with feed and sweep temperatures of 890 K and 623 K, respectively, and (iii) membrane operation with feed and sweep temperatures of 679 K and 930 K, respectively. For the latter two cases, temperatures were selected such that the normalized temperature gradient, ψ was ~ 0.3 [Romero and Wilhite, 2012] while ensuring an averaged inlet temperature of 773 K, as calculated from Eq. 2.11:

$$\psi = \frac{T_o^F - T_o^S}{T_o^F} \tag{2.10a}$$

$$\psi = \frac{T_o^S - T_o^F}{T_o^S} \tag{2.10b}$$

for adiabatic case (ii) and for adiabatic case (iii) respectively.

$$T_{ave} = \frac{C_{p,F} F_o^F T_o^F + C_{p,S} F_o^S T_o^S}{C_{p,F} F_o^F + C_{p,S} F_o^S} \tag{2.11}$$

Figure 2.11a presents a comparison of overall carbon monoxide conversion obtained for isothermal operation with the three adiabatic cases described above. Results show that overall carbon monoxide conversion for all four cases follow the trend previously described in Section 2.5.1. A comparison of membrane apparent H_2:CO permselectivity for the isothermal and adiabatic cases (Figure 2.11b) indicates H_2:CO permselectivities obtained from isothermal operation are higher than the adiabatic case of uniform inlet temperatures. Operation with an externally-imposed, sweep-to-feed thermal gradient further reduces achievable H_2:CO apparent permselectivity, while an externally-induced feed-to-sweep thermal gradient reduces the loss in apparent selectivity from adiabatic operation.

A comparison of hydrogen recoveries (Figure 2.11c) indicates a negligible effect of non-isothermality on hydrogen transport rates. These trends combine to indicate a shift in H_2:CO selectivities with negligible change in recovery rates when reaction heat produced by the equilibrium-limited water-gas-shift reaction is allowed to accumulate within the membrane reactor. Simulations indicate that this negative impact of reaction heat accumulation may be partially mitigated by imposition of an opposing thermal gradient.

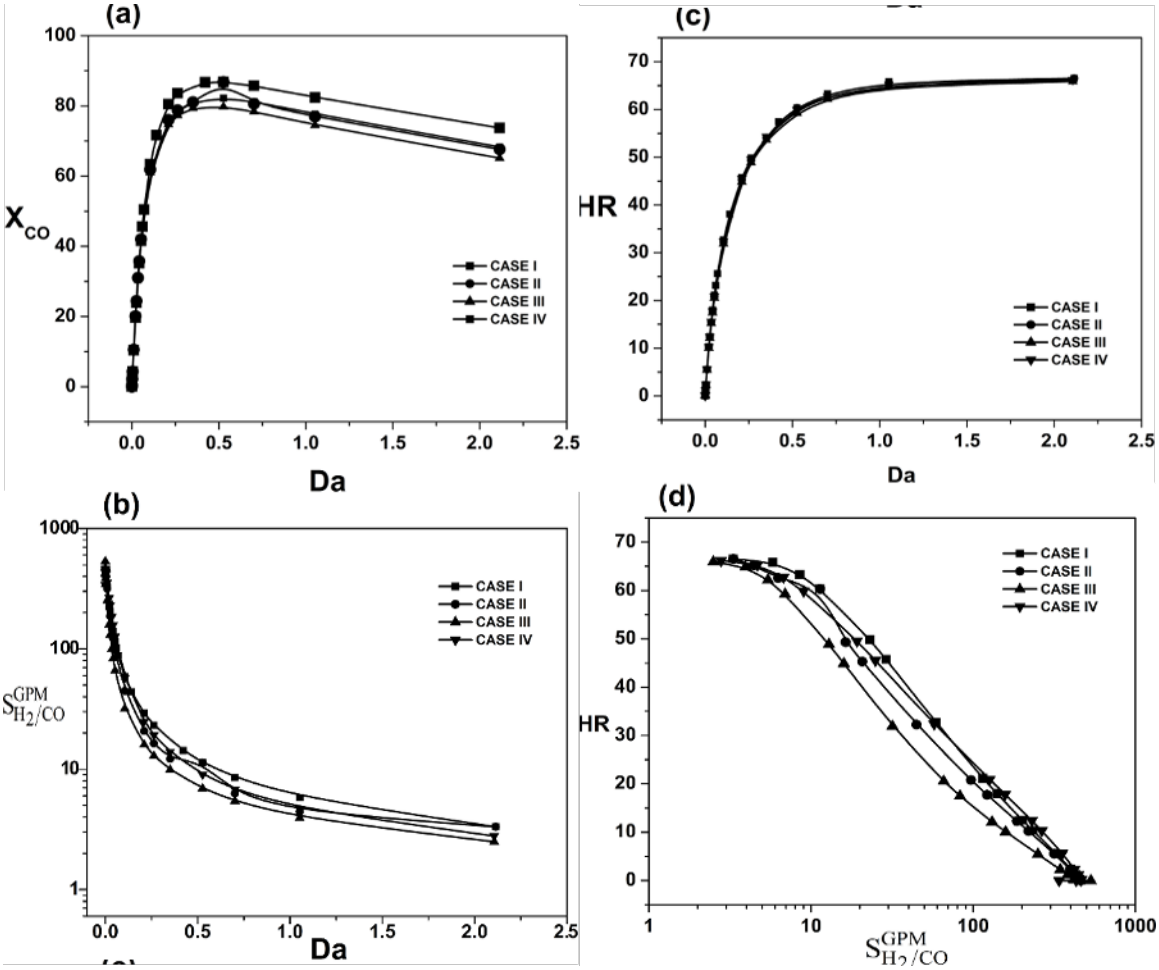

Figure 2.11: Comparison of GPM design performance as function of temperature at corresponding Damkohler number, (a) CO conversion (b) apparent permselectivity of H_2/CO based on permeate effluent composition (c) H_2 Recovery (HR) (d) apparent permselectivity of H_2/CO vs H_2 Recovery, at $\zeta = 0.1$.

2.6 Conclusions

In this chapter we have developed a two dimensional model of a shell-and-tube membrane reactor employing a typical reformate mixture (9 mol%-CO, 3 mol%-CO_2, 28 mol%-H_2, 15 mol%-H_2O) and a overall H_2O:CO ratio of 9:1. Simulations indicate that apparent CO:H_2 permselectivities of 90:1 to $>$200:1 at H_2 recoveries of 20% to upwards of 40% may be achieved through appropriate design of the catalytic membrane and selection of operating conditions. Two design criteria are identified for achieving selective removal of CO from H_2-rich reformate mixtures, in terms of the catalytic film Thiele moduli ($\Phi = 7.6$) and a dimensionless ratio of H_2 permeation to CO conversion rates ($\zeta < 0.4$). A methodology for identifying a suitable range of operating parameters is presented, based upon a target operating point corresponding to a CO conversion equal to the equilibrium conversion calculated using the reformate feed composition.

At an isothermal membrane reactor temperature of 573 K corresponding to a catalytic membrane thickness of 5.56 mm, this operating point results in a H_2:CO apparent permselectivity of 298.4:1 at a H_2 recovery of 41.6%; permeate gas produced under these conditions has a CO content of 0.022% and H_2 content of 20.6%, or 0.06% CO and 58% H_2 on a dry-gas basis. Comparison of adiabatic and isothermal simulations indicates that accumulation of reaction heat reduces apparent permselectivities; however this may be mitigated by external imposition of a countering thermal gradient. The design rules developed in this chapter are extended to selective separation of hydrogen from ethanol steam reforming in Chapter 4.

3. EXPERIMENTAL DEMONSTRATION OF WATER-GAS-SHIFT CATALYTIC MEMBRANE REACTOR MODEL

3.1 Introduction

This chapter presents an experimental demonstration of the concept of selective hydrogen purification from a typical diesel reformate mixture (4.5 mol% CO, 1.5 mol% CO_2, 14 mol% H_2, 7.5 mol% H_2O) by manipulating reaction and diffusion in total absence of permselective materials, employing a 13 wt% Cu(II)O/$\gamma-Al_2O_3$ catalytic membrane reactor for water-gas-shift (WGS) reaction. In chapter 2, this concept was demonstrated using an isothermal and non isothermal WGS catalytic membrane reactor model with a catalyst pore diameter of 10 nm. The simulation results predicted that an apparent H_2:CO permselectivities of 90:1 to >200:1 and hydrogen recoveries ranging from 20 to 40% can be achieved at appropriate design conditions. A parametric analysis was also performed to study the effect of Thiele modulus (Φ) and separation factor (ζ), an optimum value of 7.6 for Thiele modulus and separation factor < 0.4 was found. The model was also simulated to study the non isothermal affects of WGS reaction varying the isothermal temperature. In this chapter, the isothermal model is experimentally demonstrated using a gas permeation system.

A gas permeation system originally developed by Kim and Wilhite [Kim *et al.*, 2012] was used for experimental demonstration of the model. The original experimental system was modified to include steam (H_2O) in both feed and sweep and to allow effluent feed and sweep gas stream analysis using a Gas Chromatography (GC 3000A-Agilent technologies). The analysis of resulting catalytic membrane reactor results show the feasibility of cost effective high-purity hydrogen purification in the absence of a H_2-permselective material.

A literature review of the preparation on microporous membranes is first presented, followed by a detailed description of the catalyst preparation method employed in this experiment. Finally, the experimental results are discussed and compared with modeling results at the same pore diameter.

3.1.1 Porous substrates

Inorganic microporous membranes of desired pore structure and thickness are prepared using an inert mesoporous substrate to provide mechanical support for the thin film membranes. A disk or a shell-tube of the following mesoporous substrates are commonly employed in the literature: porous stainless steel (PSS), ceramic inert material, porous vycor glass, alumina (Al_2O_3) and zirconia (ZrO_2) [Lin *et al.*, 2002; Hsieh *et al.*, 1988; Uhlhorn *et al.*, 1989]. These mesoporous supports are inert with large pore diameter and no specific selectivity for a single gas species.

Several techniques are available for fashioning the cylindrical shell-tube catalytic membrane described by theoretical model namely, i) slurry or dip coating, ii) sol-gel coating and/or iii) catalyst impregnation. The choice of microporous preparation technique is dependent on the pore size needed and desired membrane thickness. The thickness of the film prepared using these techniques varies from nanometers to a few microns. The details of each of these techniques are briefly presented here.

3.1.2 Slip casting or dip coating

Slip casting or dip coating is the most commonly used method to coat a microporous catalyst layer on porous support substrate (either tubular or a disk structure). The support substrate is cleaned prior to the dip coating to remove any dirt or grease, which can create pinholes in the final layer. The dip solution of desired particle size is mixed with a binder for easier coating because of its affinity with the porous substrate. The substrate is dipped vertically or tangentially in the desired catalyst solution and dried at a temperature to

evaporate the solvent in the pores [de Lange *et al.*, 1995c,a,b; Lin, 2001; Lin *et al.*, 2002]. The thickness of the coated layer is dependent on the dipping time, viscosity of the solution and the number of dip coatings [Lin *et al.*, 2002].

3.1.3 Sol-gel coating

Sol-gel is coating of sol, followed by controlled hydrolysis and condensation reactions to form the final coating [Lu *et al.*, 2007]. Fist reported by Uhlhorn et al. in [Uhlhorn *et al.*, 1989], has been used by Burggraaf and coworkers to prepare high flux microporous silica membranes. In this method, microporous silica membranes were prepared by dip-coating a polymeric silica solution on a γ-alumina support and reported a pore diameter of 2.5 nm and 50% porosity [Uhlhorn *et al.*, 1989]. Sol-gel method requires, a very smooth substrate with small pores (for uniform coating) and clean-room conditions (to prevent cracks and pinholes on final coating) [Lin, 2001; Lin *et al.*, 2002; de Vos and Verweij, 1998]. A schematic of sol-gel coating process is presented in Figure 3.1.

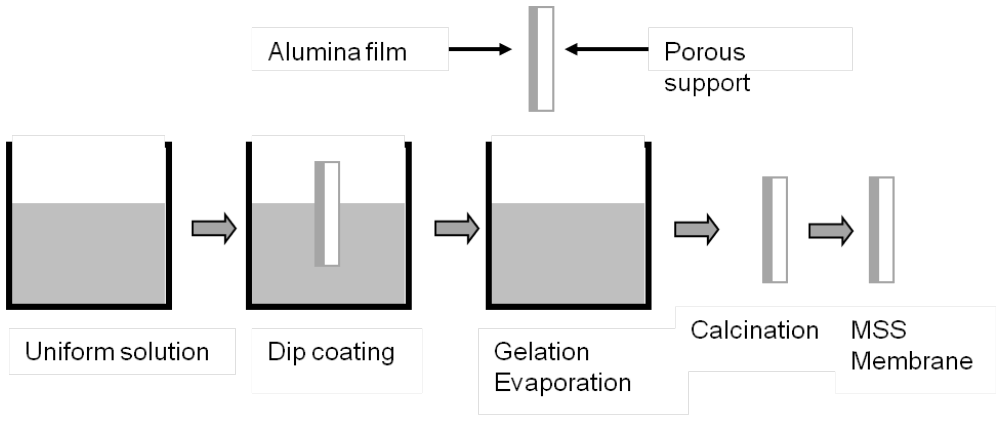

Figure 3.1: Schematic of sol-gel method for preparation of microporous membranes [Lu *et al.*, 2007].

3.1.4 Catalyst impregnation

Catalytic activity may be introduced to inert porous substrate by incipient wetness technique, wherein a catalytic metal salt is impreganted on the internal pore surface and subsequently reduced to form desired metal or oxide phase [Lloyd, 2011a; Thomas and Thomas, 2008]. The impregnation solution is deposited drop wise onto the substrate so as to ensure complete infiltration of substrate pores. For catalytic membranes, a vacuum can also be applied across the film to draw the solution through the porous substrate followed by calcination [Kim *et al.*, 2012; Zaman and Chakma, 1994]. The catalyst-impreganted porous substrate is dried then calcined to decompose metal salts to active oxides or further reduced to form desired metallic phase [Lloyd, 2011a].

The most facile way to make membrane is slurry coating, using commercially available catalysts. This avoids challenges of working out sol chemistries and catalyst synthesis and has previously been shown capable of creating dense catalytic membranes [Kim *et al.*, 2012]. The following section describes the present experimental method, substrate preparation, catalyst coating and characterization.

3.2 Experimental method

3.2.1 Substrate preparation

The porous stainless steel (PSS) tubes are chosen as the substrate owing to their durability, weldability, fittings with regular stainless steel parts, robust physical strength and availability in different sizes for scalability [Wei *et al.*, 2013; Li *et al.*, 2007]. The PSS tubes of 0.5 µm grade and 0.5 inch outer diameter and 2 inch in length were purchased from Mott corporation. The pore diameter of the graded region of the tube was measured to be 500 nm. The PSS tubes were cleaned using a recipe developed by Kim et al. [Kim *et al.*, 2012], which was based upon [Rothenberger *et al.*, 2004]. This procedure was as follows: PSS tubes were cleaned in an ultrasonic bath of alkaline solution (sodium hy-

droxide, sodium carbonate, sodium phosphate, organic detergent) at 50 °C for one hour to remove any dirt or grease. Then, tubes are thoroughly rinsed with deionized (DI) water to remove the alkaline solution. This procedure was followed by flushing the pores using pressurized air while sealing one end of the tube to remove any water present in the pores. In the final step, the tubes were allowed sufficient time to dry at room temperature.

3.2.2 Catalyst coating on PSS support

A commercial Cu(II)O_2 (13%)-Al_2O_3 catalyst, supplied as 3 mm spheres from Sigma-Aldrich, was employed for constructing membrane. This catalyst is active for WGS reaction and has identical composition to that of the catalyst assumed in the theoretical model in Chapter 2. The membrane fabrication procedure was a modified version of the procedure described by Kim et al. in [Kim *et al.*, 2012].

Two grams of catalyst was placed in 0.2 mL of 20% colloidal alumina (Alfa Aesar) and 20 mL of deionized (DI) water and milled in a ball mill (SPEX CertiPrep) for 20 minutes. The resulting catalyst solution was coated on the clean tubes with one end connected to a vacuum pump while the other end was sealed with a Teflon cap and a pressure of 10 psi is applied. The slow addition of catalyst was carried out until a uniform single layer of catalyst was observed on the tubes and then dried at room temperature. This procedure of catalyst application gives a uniform catalyst coating free of visible defects. Then, these tubes are coated uniformly with catalyst solution after placing the tubes horizontally on a rotor at a steady rotation of 10 rpm and dried at ambient temperature. This procedure of uniform catalyst coating on rotor is repeated until a desired thickness is reached, which was determined using a digital vernier caliper. Then, the catalyst coated tubes are cured in a furnace at a temperature of 450 °C for 4 hours at a heating and cooling rate of 1 °C min^{-1}.

The target catalyst thickness of 1.56×10^{-3} m was chosen based upon dimensionless design parameters established in Chapter 2 for achieving optimum H_2:CO apparent perms-

electivities and hydrogen recoveries. A visibly crack-free catalyst coating of desired thickness can be achieved employing the above procedure. An automated mercury intrusion porosimeter (PoreMaster Quantachrome Instruments) was used to measure the pore diameter and tortuosity of the catalyst powder. The analysis shows that a pore diameter of 13 nm, a tortuosity of 2 and porosity of 40%, which are similar to the conditions assumed in the model. However, the gas permeation test (described later) determined that the effective pore diameter of fabricated membrane is approximately 246 nm.

3.3 Results and discussion

3.3.1 Catalyst characterization

Figure 3.2a, b presents the scanning electron microscope (SEM) images of the catalyst coated on the PSS tube before and after the water-gas-shift reaction. The SEM images shows that there is negligible difference in pore diameter and porosity before and after the reaction. SEM-EDS analysis shows that the catalyst coating is of similar composition as that of the fresh powdered catalyst. Figure 3.3 shows the EDS spectrum showing elemental distribution. SEM-EDS analysis before and after the WGS reaction shows that there is no carbon deposition after the reaction and also there is no significant change in catalyst composition. The elemental distribution of catalyst before and after WGS reaction is presented in Table 3.1

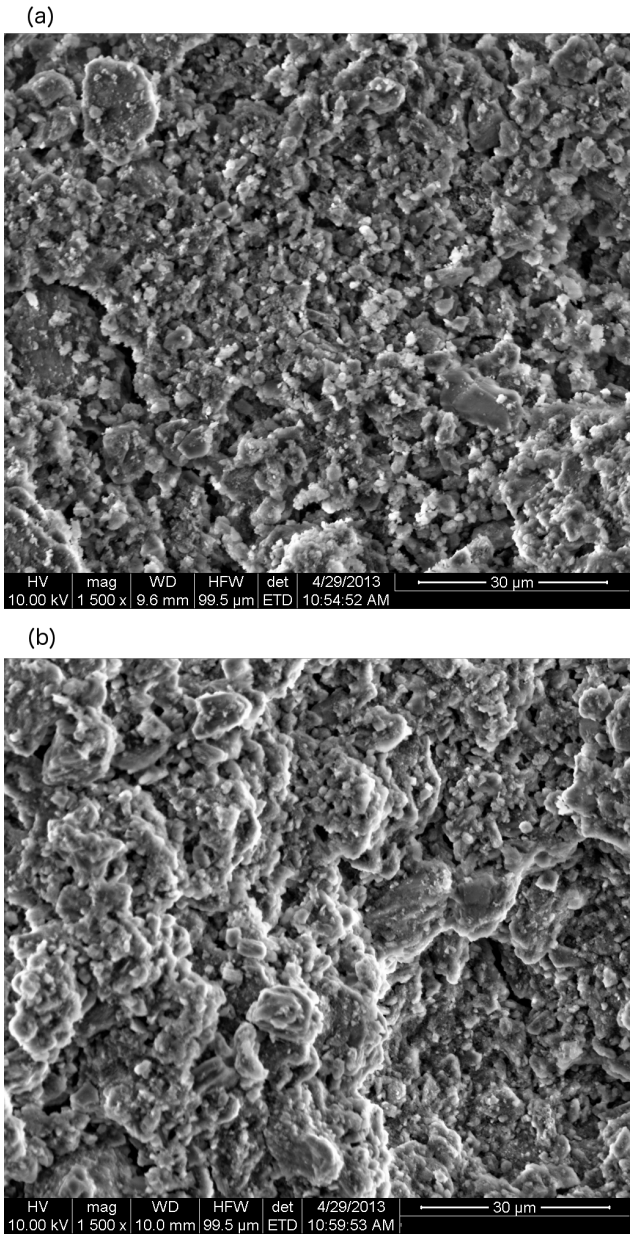

Figure 3.2: SEM image of the porous stainless steel support with a catalyst coating, (a) before, and (b) after WGS reaction.

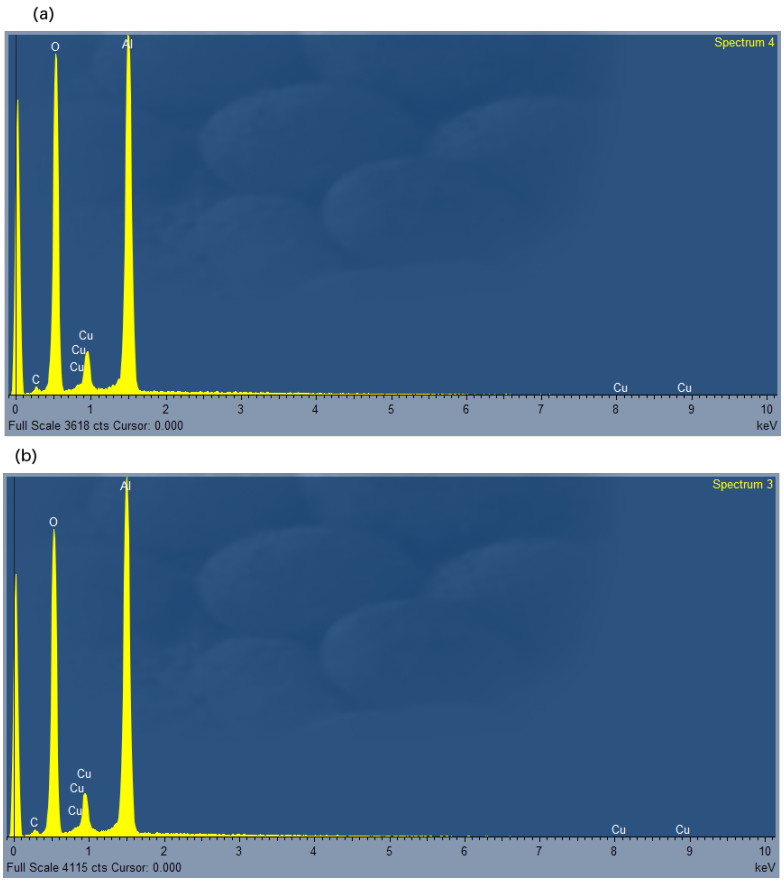

Figure 3.3: Spectrum showing the elemental distribution of the catalyst, (a) before reaction and (b) after reaction

Table 3.1: Summary of elemental distribution of catalyst, (a) before WGS reaction (b) after WGS reaction.

(a)

Element	Weight%	Atomic%
C	2.05	3.56
O	48.18	62.59
Al	39.31	30.33
Cu	10.46	3.43

(b)

Element	Weight%	Atomic%
C	2.37	4.05
O	49.74	63.90
Al	37.79	28.78
Cu	10.11	3.27

3.3.2 Experimental setup

The catalyst coated PSS tubes are packaged into the membrane reactor apparatus and placed in the tube furnace (HST 12/200, Carbolite) and heated at a rate of 3°C/min to 723 K. The feed was a dry gas mixture of CO-4.5 mol%, CO_2-1.5%, H_2-14 mol%; steam was added to dry gas using a gas bubbler which is maintained at constant temperature of 42 °C (water vapor mole percent of 7.5% determined via Antoine equation) using heating tape and a digital temperature controller (Omega). The heating tape is thermally insulated to reduce the fluctuations of the actual temperature of the bubbler. The sweep gas mixture of 50 mole% Argon and 50 mole% of steam was supplied using a gas bubbler maintained at a constant temperature of 82 °C. The gas lines to the reactor were insulated and heated to prevent the condensation of steam. The retentate and permeate outlet were passed through a moisture trap enclosed in a dry-ice to condense the steam. The effluent gas compositions were then analyzed using a GC, which was calibrated prior to the experiment. The

schematic of the gas permeation experimental system is shown in Figure 3.4.

3.3.3 Gas Chromatography (GC) calibration

An Agilent GC 3000a equipped with a thermal conductivity detector (TCD) and a molecular-sieve columns is used to measure the feed and sweep effluent gases. The GC uses argon gas for internal calibration, which was recommended by Agilent technologies. GC is calibrated for a range of gas mole fractions after baking for 12 to 16 hours to remove the adsorbed carbon on the TCD and molecular-sieve columns. The calibration procedure is followed according to the equipment manual provided by Agilent technologies. The mole fraction of each gas is varied by diluting with the carrier gas (Ar) and fed to the inlet of the GC, then the area of signal (μV) is measured. Sufficient number of measurements were taken and an average area is noted. Figure 3.5 shows the GC calibration, the area of signal (μV) is plotted against the mole fraction of each gas species.

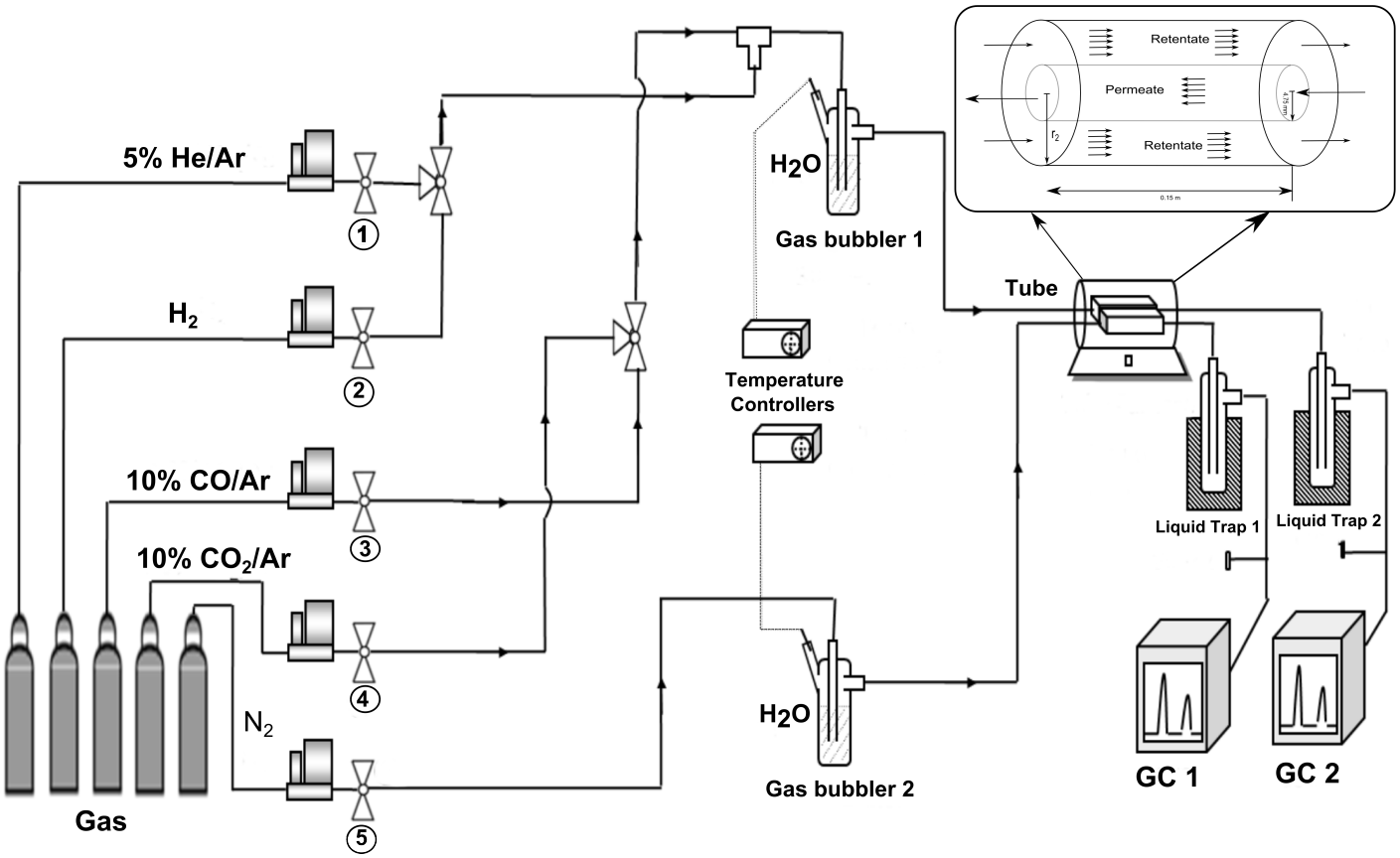

Figure 3.4: Schematic of experimental apparatus for gas permeation experiments.

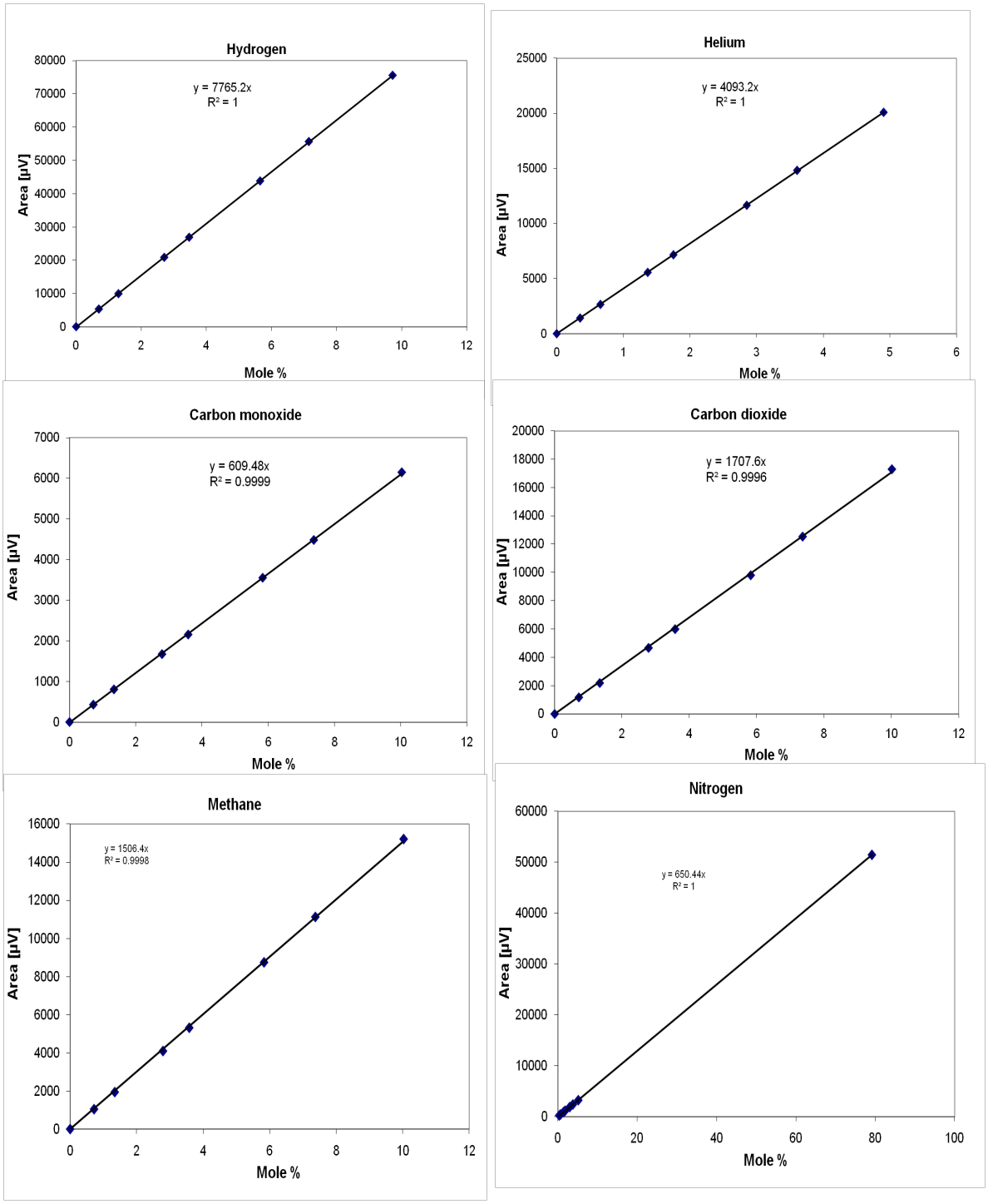

Figure 3.5: GC calibration for hydrogen, carbon monoxide, carbon dioxide, helium, methane and nitrogen

3.3.4 Gas permeation test

A gas permeation test is carried out in order to measure the flux of inert nitrogen across catalyst/membrane for determining nitrogen diffusivity in the catalyst film and characterize the pore diameter assuming Knudsen diffusion. The nitrogen gas is fed to the inner tube and argon gas is fed to the outer shell and both effluent gases are analyzed using the GC, which was calibrated prior to the permeation test. The feed and sweep outlet flow rates are measured using a soap-film bubble meter. Gas inlet flow rates are varied in order to vary the driving force for permeation.

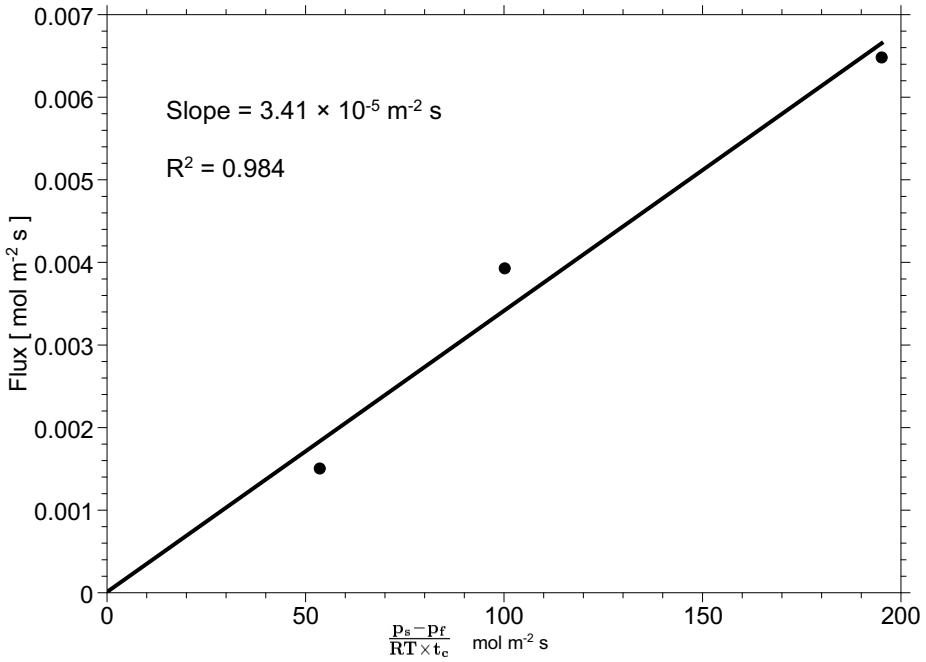

Figure 3.6: Nitrogen gas permeation test to determine the actual pore diameter.

The permeation rate of a gas species across the catalyst/membrane is be given by:

$$J_A = \frac{D}{RTt_c}\left[P_f y_A^f - P_s y_A^s\right] \tag{3.1}$$

where J_A is the flux of gas species A ($\mathrm{mol\,m^{-2}\,s^{-1}}$), D is the effective diffusivity of gas species A in the catalyst ($\mathrm{m^2\,s^{-1}}$), P_f is the total pressure in the feed volume (Pa), P_s is the total pressure in the sweep volume (Pa), y_A^f and y_A^s are the mole fractions of the gas species in the feed and sweep volumes respectively and t_c is the catalyst thickness (m).

Figure 3.6 shows the nitrogen flux and the pressure difference; the slope is the effective diffusivity of $3.41 \times 10^{-5}\,\mathrm{m^2\,s^{-1}}$. Assuming Knudsen diffusion, the pore diameter is determined using the nitrogen flux. The equation to determine the effective Knudsen diffusivity of gas species in porous media is given by:

$$D_{i,K} = \frac{2d_p}{3}\left[\frac{8RT}{\pi M}\right]^{1/2} \tag{3.2}$$

where d_p is the pore diameter (m), R is the universal gas constant ($\mathrm{J\,mol^{-1}K^{-1}}$), T is the temperature (K), and M is the molecular weight of gas species ($\mathrm{g\,mol^{-1}}$). The effective pore diameter of the catalyst coating assuming purely Knudsen diffusion, is calculated as 246 nm.

It should be noted that this pore diameter (246 nm) obtained through catalyst coating is much larger than that assumed (10 nm) in the modeling simulations. The difference between catalyst powder pore diameter (13 nm) and catalyst coating pore diameter (246 nm) may be due to formation of pinholes and cracks. Therefore, the model simulations were performed assuming this pore diameter for aptly comparing with experimental results.

3.3.5 Results and discussion

3.3.5.1 CO conversion

The percentile overall CO conversion is calculated based on the outlet flowrates and mole fraction of carbon monoxide, given by:

$$X_{CO} = \frac{F^F_{CO,o} - \left(F^F_{CO,e} + F^S_{CO,e}\right)}{F^F_{CO,o}} \times 100 \tag{3.3a}$$

Figure 3.7 shows that overall conversion in the catalytic membrane reactor as a function of residence time. The results show that overall CO conversion increases as we increase the residence time owing to increase in residence time for reaction.

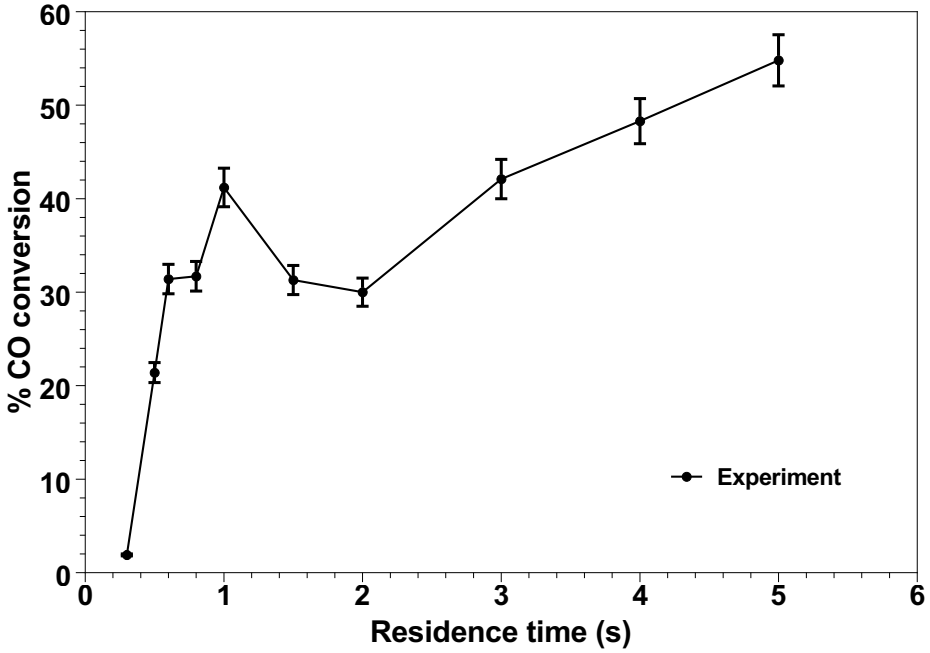

Figure 3.7: Experimental results showing CO conversion versus residence time at isothermal temperature of 773 K.

3.3.5.2 Hydrogen recovery

The percentile hydrogen recovery (HR) is determined based on the outlet flow rates of hydrogen and mole fraction of hydrogen, given by:

$$HR = \frac{F^{S}_{H_2,e}}{F^{F}_{H_2,e} + F^{S}_{H_2,e}} \times 100 \tag{3.3b}$$

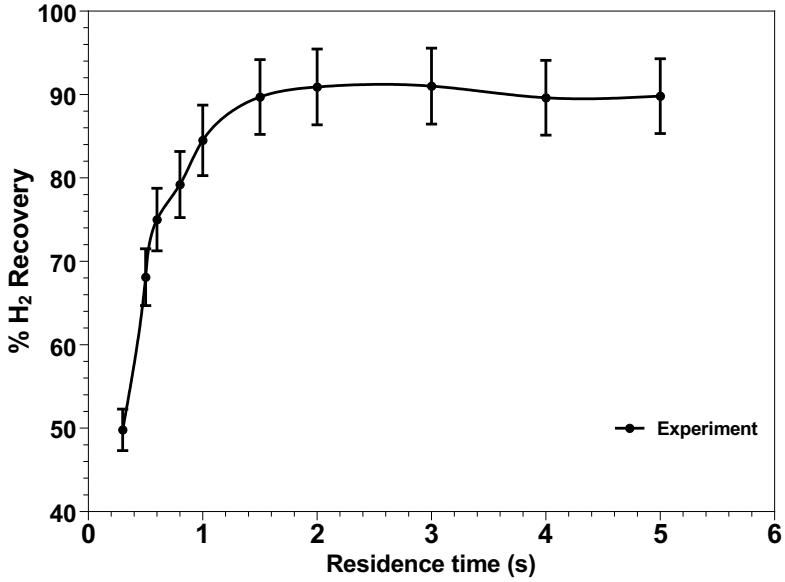

Figure 3.8: Experimental results showing H_2 recovery versus residence time at isothermal temperature of 773 K.

Figure 3.8 shows that the permeate hydrogen recovery in the catalytic membrane reactor as a function of residence time. The results show that hydrogen recovery increases with increase in the residence time, owing to an increase in the CO conversion.

3.3.5.3 H_2/CO permselectivity

The H_2/CO permselectivity is calculated based on the outlet flow rates of the feed and sweep volumes, and the mole fractions of hydrogen and carbon monoxide, given by the equation:

$$S^{GPM}_{H_2/CO} = \left[\frac{F^S_{H_2,e}}{F^S_{CO,e}}\right] / \left[\frac{F^F_{H_2,e}}{F^F_{CO,e}}\right] \tag{3.3c}$$

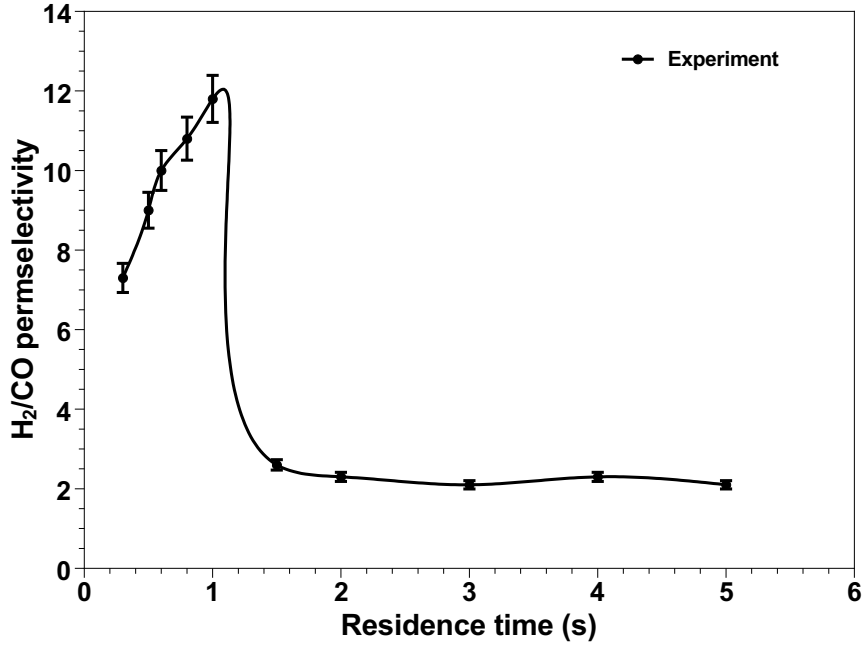

Figure 3.9: Experimental results showing H_2:CO permselectivity versus residence time at isothermal temperature of 773 K.

Figure 3.9 shows H_2/CO permselectivity in the catalytic membrane reactor as a function of residence time. The results show that H_2/CO permselectivity increases at low

residence time and reaches a maxima, with further increase in residence time decreasing permselectivity.

3.3.6 Comparison of the model and experimental results

The isothermal model developed in Chapter 2 was simulated at a temperature of 773 K and a catalyst pore diameter of 246 nm (same as experimental catalyst coating). The modeling results are then compared with experimental results presented in previous section.

Figure 3.10a presents CO conversion as a function of residence time in the reactor for both the experiments and model. It can be observed that both experiments and modeling results comparably follow same trend. Simulations predict a maximum CO conversion of 78%, while the experimental results demonstrate the maximum CO conversion of 55%. Figure 3.10b shows the hydrogen recovery (HR) of experimental and model simulation results as a function of residence time. It can be observed that both experiments and simulation results follow similar trend. Figure 3.10c shows the H_2/CO permselectivity as a function of residence time in the reactor for experiments and model results.

While the experiments confirm quantitative trends, the experimental and modeling results disagree, specifically experiments obtain significantly higher H_2 recoveries, lower conversions. Also, the maxima in H_2 permselectivity was observed to occur at a significantly higher residence time than predicted by theory. It can be observed that both experiments and simulation results follow similar trend, while experimental results show that a maximum H_2/CO permselectivity of 12 with H_2 recovery of 80% can be achieved at a residence time of 1.1 seconds, as compared to simulation value of 6 with hydrogen recovery of 55% at the same residence time. Simulations predict a maximum H_2 permselectivity of 19 with H_2 recovery of $< 15\%$. This shows that the catalyst coating has a larger pore diameter and therefore a higher permeation for both hydrogen and carbon monoxide.

(a) CO conversion

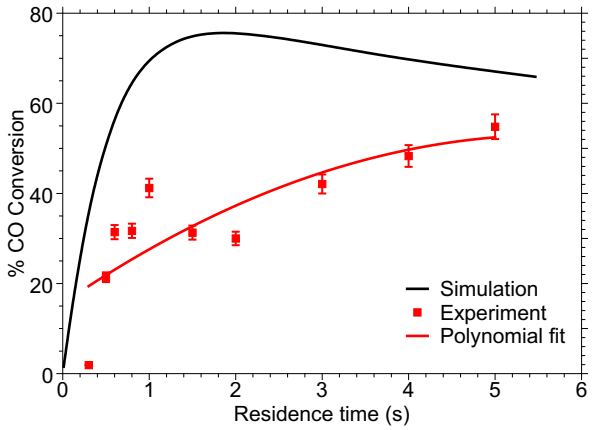

(b) Permeate hydrogen recoveries

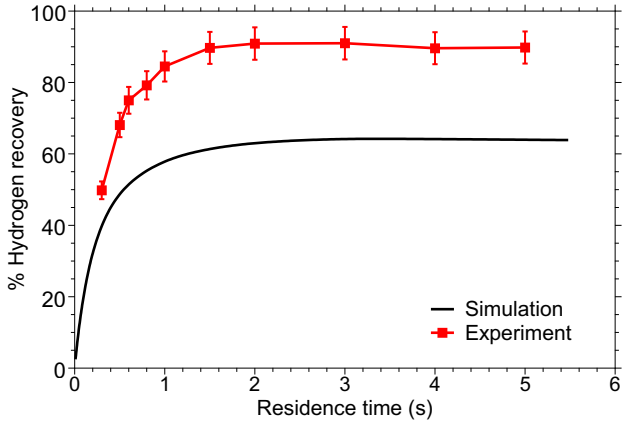

(c) H_2/CO permselectivities

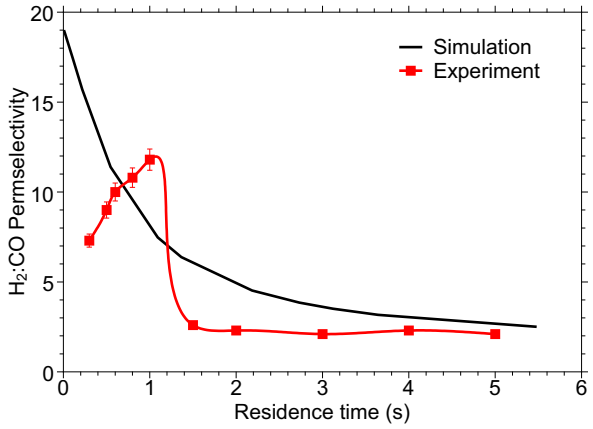

Figure 3.10: Comparison of experimental and modeling results

3.4 Conclusions

This chapter presents the experimental demonstration of a catalytic membrane reactor for hydrogen separation from a diesel reformate gas-mixture (4.5% CO, 1.5% CO_2, 14% H_2, 7.5% H_2O). The gas permeation test has shown that the pore diameter of catalyst coating is determined as 246 nm. Results demonstrate that a mesoporous catalytic membrane is capable of achieving a maximum H_2:CO permselectivity of 12 with a hydrogen recovery of 80%. The experimental results are compared with that of the modeling results for a similar pore diameter it is observed that the trends qualitatively agreed but quantitively disagreed.

4. DESIGN OF COMPOSITE CATALYTIC MEMBRANE REACTOR FOR HYDROGEN EXTRACTION FROM BIOETHANOL REFORMING

4.1 Introduction

In this chapter, a design of composite catalytic membrane reactor for selective hydrogen removal from bioethanol steam reforming without employing any hydrogen permselective material is investigated. A composite catalytic membrane is designed with multiple function-specific catalyst layers to achieve consecutive ethanol pyrolysis, methane steam reforming and water-gas-shift reaction, as well as selective CO combustion to provide reaction heat. Isothermal and non-isothermal models are developed to study the hypothesis that selective hydrogen extraction form bioethanol can be achieved by manipulating reaction-diffusion and thermal gradients without employing any hydrogen permselective materials.

This concept is explored in two parts. First, an isothermal model with two catalyst layers one active for ethanol reforming (pyrolysis and methane steam reforming) and second layer active for water-gas-shift reaction. The water-gas-shift reaction catalyst layer is used as a purification layer, in lieu of a hydrogen permselective membrane. The simulation results from isothermal design is used to identify several design points at which the membrane performance is evaluated. The initial isothermal model is extended to account for heat conduction of the membrane system and adiabatic simulations are carried out and heat duty is identified. Finally, a third catalyst layer active for oxidation reactions is added to counteract the endothermic heat of ethanol reforming and achieve an autothermal operation. The schematic of design concept and ideal concentration profiles of gas species is presented in Figure 4.1.

Results demonstrate the potential of this concept for achieving permselective hydrogen

separation without employing permselective materials. Two-layer isothermal membrane calculations predict a H_2:CO permselectivity of 120:1 at permeate hydrogen recoveries of 20-40% with appropriate designs. Two-layer non-isothermal model simulations show that a reduction in performance of the membrane can occur due to endotherm formation caused by reforming. To resolve this, a three-layer autothermal design employing an additional catalytic combustion layer active for oxidation of all chemical species is explored. Results confirm that appropriate placement of in situ combustion within the membrane can resolve this issue, resulting in predicted H_2:CO permselectivity of 220:1 at H_2 recovery of 25%.

4.2 Theoretical

Figure 4.1 shows the composite catalytic membrane reactor concept, sketches of ideal concentration profiles.

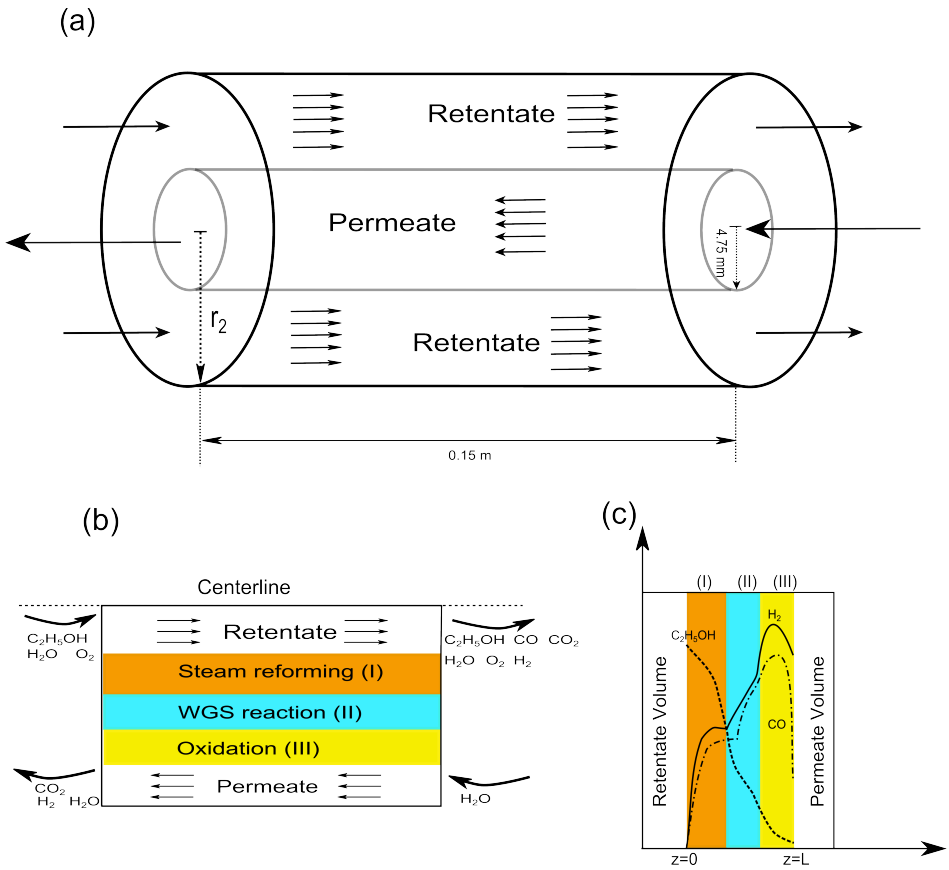

Figure 4.1: (a) Schematic of the shell-tube composite catalytic membrane reactor, (b) The design concept of composite catalytic membrane reactor for ethanol reforming, (c) Sketches of ideal concentration profiles inside the composite catalytic membrane.

4.2.1 Model development & assembly

A steady state two-dimensional model is developed to describe the reaction and diffusion and/or heat conduction in a counter-current shell-and-tube catalytic membrane reactor (Figure 4.1) with an inner or bore radius of 4.75 mm and a shell radius (r_1), calculated based upon the catalyst thickness such that retentate and permeate flow volumes are identical. The reaction and diffusion within the catalytic membrane is described using a single

component Fick's diffusion model assuming Knudsen diffusion regime in nominal pore diameter of 10 nm with negligible trans-membrane pressure drop (i.e., equal retentate and permeate pressures), such that a single component Fick's diffusion model with effective Knudsen diffusivities may be employed:

$$\nabla\left(D_{K,i}^{eff}\nabla C_i\right) = -r_{ij}\delta^i \tag{4.1a}$$

where $C_i = \frac{Px_i}{RT}$

Assuming a porosity of 45% and tortuosity of 2 [Neurock *et al.*, 1993], the effective Knudsen diffusivity is estimated from the kinetic theory of gases [Bird *et al.*, 2007],

$$D_{K,i}^{eff} = \frac{\varepsilon}{\tau}\left[\frac{1}{3}d_p\left(\frac{8RT}{\pi M_i}\right)^{0.5}\right] \tag{4.1b}$$

Retentate and permeate fluid volumes are modeled assuming ideal plug flow behavior with no axial dispersion or back mixing. Both volumes are assumed to be isobaric with uniform outlet pressure of 1 atm (i.e., assuming negligible pressure drop). The resulting one-dimensional equations describing individual species molar flow along the axial length of the membrane assume mass appearance in the bulk fluid volume occurs via gas-solid mass transfer.

This is implemented using the following equations.

$$\frac{1}{A_C^F}\frac{dF_i^F}{dz} = -k_{gs}\tilde{a}^F\left(p_i^F - p_i^{cat}\right) \tag{4.2a}$$

$F_i^F = F_{i,o}^F$ @ z=0

$$\frac{1}{A_C^S}\frac{dF_i^S}{dz} = -k_{gs}\tilde{a}^S\left(p_i^S - p_i^{cat}\right) \tag{4.2b}$$

$F_i^S = F_{i,o}^S$ @ z=0.15

The fluid and catalyst volume models are linked through boundary conditions equating mass fluxes normal to the fluid-catalyst boundary of individual species, which is represented by Eq. 4.2c.

$$\left(\nabla D_{K,i}^{eff} C_i\right) \cdot \tilde{n} = k_{gs}\left(p_i^{F,S} - p_i^{cat}\right) M_i \tag{4.2c}$$

The fluid-wall mass transfer coefficient is estimated from the fluid Schmidt number (Sh) and Reynolds number (Re) between 3-2000, is taken from [Petrovic and Thodos, 1953]

$$Sh = \frac{k_{gs} d_p}{D} = \left(\frac{0.357}{\varepsilon}\right) Re^{0.641} Sc^{1/3} \tag{4.2d}$$

$$Re = \left(\frac{d_t \rho_{mix} u}{\mu_{mix}}\right) \tag{4.2e}$$

$$Sc = \frac{\mu_{mix}}{\rho_{mix} D} \tag{4.2f}$$

Conductive heat transport within the catalytic membrane is described employing an effective thermal conductivity following [Butt, 1965],

$$\nabla\left(k_{cat} \nabla T^{cat}\right) = \left(-\triangle H_j^o\right)\left(-r_{ij}\delta^i\right) \tag{4.3a}$$

where the effective thermal conductivity is defined as

$$k_{cat} = \varepsilon^2 k_{gas} + (1-\varepsilon) k_{solid} \tag{4.3b}$$

Fluid-phase energy balances assuming one-dimensional plug flow with heat appearance in bulk fluid occurring solely via gas-solid heat transfer are employed with initial

conditions corresponding to inlet retentate and sweep temperatures at z = 0 and z = 0.15, respectively.

$$\frac{\left(\sum C_{p,i}F^F_{i,o}\right)}{A^F_C}\frac{dT^F}{dz} = -h^F\tilde{a}^F\left(T^{cat} - T^F\right) \tag{4.4a}$$

with initial condition, $T^F = T^F_o \ @z = 0$

$$\frac{\left(\sum C_{p,i}F^S_{i,o}\right)}{A^S_C}\frac{dT^S}{dz} = -h^S\tilde{a}^S\left(T^{cat} - T^S\right) \tag{4.4b}$$

with initial condition, $T^S = T^S_o \ @z = 0.15$

The fluid-wall heat transfer coefficient for Reynold's number between 40 and 2000 is defined by Eq. 4.5a [Dixon and Cresswell, 1979] in terms of Nusselt number.

$$Nu_{fw} = \frac{h_{fs}d_p}{k_g} = 0.24Pr^{1/3}Re^{0.8} \tag{4.5a}$$

Where the Reyond's number (Re) and Prandtl number (Pr) are defined as

$$Re = \frac{d_t\rho u}{\mu_{mix}} \tag{4.5b}$$

and

$$Pr = \frac{C_{P,mix}\mu_{mix}}{k_{cat}} \tag{4.5c}$$

respectively.

Fluid velocity is calculated from the sum of individual species molar flowrates and assuming ideal gas relationship between molar and volumetric flowrates.

The dynamic viscosity of the gas mixture is evaluated using the semi-empirical formula

developed by C. R. Wilke in [Wilke, 1950].

$$\mu_{mix} = \sum \frac{x_i \mu_i}{x_i + \sum x_j \varphi_{ij}} \tag{4.5d}$$

where

$$\varphi_{ij} = \frac{\left[1 + \left[\frac{\mu_i}{\mu_j}\right]^{\frac{1}{2}} \left[\frac{M_j}{M_i}\right]^{\frac{1}{4}}\right]^2}{\sqrt{8}\left[1 + \frac{M_i}{M_j}\right]^{\frac{1}{2}}} \tag{4.5e}$$

and

$$\mu_i = 2.67 \times 10^{-5} \frac{\sqrt{M_i T}}{\sigma^2 \Omega_\mu} \tag{4.5f}$$

in which Lennard-Jones parameters are taken from [Bird *et al.*, 2007].

4.2.2 Reaction system

A simplified system of six unique chemical reactions is employed to describe the ethanol steam reforming (pyrolysis, methane steam reforming and water-gas shift-reaction) and oxidation reaction (methane, carbon monoxide and hydrogen combustion) in the present modeling study. Rate expressions and parameters are summarized in Table 4.1. The Langmuir-Hinshelwood type rate expressions for ethanol pyrolysis and methane steam reforming on a Nickel based catalyst (Ni/Al_2O_3) are taken from V. Mas et al. [Mas *et al.*, 2008b; Verónica *et al.*, 2008; Mas *et al.*, 2008a] The kinetic expressions and rate parameters for water-gas-shift reaction for a $CuO(II)/Al_2O_3$ (5% Copper on Alumina) catalyst, assuming a catalyst density of $1000\,kg\,m^{-3}$ are modeled as described by Mizsey et al. in [Mizsey *et al.*, 2001]. The partial oxidation reaction of methane, carbon monoxide and hydrogen kinetic data on Pt/Al_2O_3 catalyst is taken from [Aubé and Sapoundjiev, 2000; Maymo and Smith, 1966; Amphlett *et al.*, 1996] respectively. The reforming layer is modeled as being active solely for reactions 1-3, while the preferential oxidation layer is assumed active for reactions 4-6 only. The rate expressions and rate kinetics are presented

in Table 4.1.

4.2.3 Design parameters

A two-dimensional model is developed to describe a counter-current shell-and-tube catalytic membrane reactor (Figure 4.1) with an inner or bore radius of 4.75 mm and shell radius calculated based upon the catalyst thickness such that retentate and permeate flow volume are identical.

The first layer Thiele modulus is determined from Eq.4.6a, a dimensionless ratio of the rate of ethanol pyrolysis reaction within the membrane relative to the permeation of ethanol.

$$\Phi^{I} = t_{cat}^{I} \left[\frac{r_{C_2H_5OH,o}\left(p^{F}_{C_2H_5OH,o}, T\right) RT}{D^{eff}_{K,C_2H_5OH} p^{F}_{C_2H_5OH,o}} \right] \left(\frac{1}{2}\right) \left(\frac{2}{3}\right)^{1/2} \tag{4.6a}$$

The normalized Thiele modulus for the second-layer (active for water-gas-shift reaction) is determined from Eq. 4.6b employing shape- and second-order kinetics normalizations following [Aris, 1975] and accounting for reaction reversibility following [Carberry, 1962]. The resulting design parameter represents a dimensionless ratio of the rate of CO reaction within the membrane relative to the permeation rate of CO (undesired permeate) across the membrane.

$$\Phi^{II} = t_{cat}^{II} \left[\frac{r_{WGS,o}\left(p^{F}_{i,o}, T\right) RT}{D^{eff}_{K,CO} p^{F}_{CO,o}} \right] \left(\frac{1}{2}\right) \left(\frac{2}{3}\right)^{1/2} \left[\frac{K_{eq,WGS}+1}{K_{eq,WGS}} \right]^{1/2} \tag{4.6b}$$

The Thiele modulus of the third catalyst layer active for oxidation reaction is determined from Eq. 4.6c, which is a dimensionless ratio of the rate of oxidation within the

Table 4.1: Summary of reaction system, rate expressions and parameters.

Reaction	Catalyst	Kinetics	Units	Heat of reaction
$C_2H_5OH \longrightarrow CH_4 + CO + H_2$	Ni/Al_2O_3	$r = \frac{k_1 K_E P_E}{1+K_E P_E + K_W P_W + K_M P_M}$ $k_1\,(873K) = 4.833 \times 10^{-4}$ E_a=278.74 kJ mol^{-1} K_M=11.2 $\times 10^{-3}$ Pa^{-1} K_E=6.1 $\times 10^{-4}$ Pa^{-1} K_W=3.7 $\times 10^{-4}$ Pa^{-1}	mol.kg.s^{-1}	49.7 kJ.mol^{-1}
$CH_4 + H_2O \longleftrightarrow CO + 3H_2$	Ni/Al_2O_3	$r = k\left(P_{CH_4}P_{H_2O} - \frac{P_{H_2}^3 P_{CO}}{K_{eq}}\right)$ $k = 1.275 \times 10^6 exp\left(\frac{-16950}{RT}\right)$ $K_{eq,WGS} = exp\left(\frac{-26830}{RT} + 30.114\right)$	mol kg s^{-1}	206 kJ mol^{-1}
$CO + H_2O \longleftrightarrow CO_2 + H_2$	CuO/Al_2O_3	$r = k\left(P_{CO}P_{H_2O} - \frac{P_{H_2}P_{CO_2}}{K_{eq}}\right)$ $k = 2.25 \times 10^{-3} exp\left(\frac{-50000}{RT}\right)$ $K_{eq,WGS} = 9.543 \times 10^{-3} exp\left(\frac{39876}{RT}\right)$	mol m^{-3} s^{-1}	−42 kJ mol^{-1}
$C_2H_5OH + O_2 \longrightarrow CO_2 + 3H_2O$	Pt/Al_2O_3	$r = 6 \times 10^{16} exp\left(\frac{-55400}{RT}\right) C_{C_2H_5OH}$	mol m^{-3} s^{-1}	−1277 kJ mol^{-1}
$CH_4 + 2O_2 \longleftrightarrow CO_2 + 3H_2O$	Pt/Al_2O_3	$r = 1.35 \times 10^4 exp\left(\frac{-54400}{RT}\right) C_{CH_4}$	mol m^{-3} s^{-1}	−815 kJ mol^{-1}
$CO + {}^1/_2O_2 \longrightarrow CO_2$	Pt/Al_2O_3	$r = 6.62 \times 10^6 exp\left(\frac{-21900}{RT}\right) P_{O_2}^{0.8}$	mol kg s^{-1}	−242 kJ mol^{-1}
$H_2 + {}^1/_2O_2 \longrightarrow H_2O$	Pt/Al_2O_3	$r = 0.0226 exp\left(\frac{-1000}{RT}\right) C_{CO}$	mol kg s^{-1}	−283 kJ mol^{-1}

catalyst relative to that of permeation of oxygen.

$$\Phi^{III} = t_{cat}^{III} \left[\frac{r_{Comb,o}\left(p_{i,o}^{F}, T\right) RT}{D_{K,O_2}^{eff} p_{O_2,o}^{F}} \right] \left(\frac{1}{2}\right) \left(\frac{2}{3}\right)^{1/2} \tag{4.6c}$$

A dimensionless separation factor, ζ, is then defined as the ratio of hydrogen (desired permeate) transport across the membrane relative to the rate of CO conversion by water-gas-shift reaction within the membrane, and is defined as:

$$\zeta = \frac{A_{mem}}{V_{mem}} \frac{\left(\frac{D_{K,H_2,K}^{eff}}{t_{mem}^{WGS}}\right)}{\eta_o \delta^{II} r_{WGS,o}\left(p_{i,o}, T\right)}$$

4.2.4 Design specifications

The simulated gas mixture of 16% ethanol, 32% H_2O and 52% N_2 is supplied to the inlet of retentate volume. The permeate gas mixture consist of nitrogen and steam which is calculated such that overall steam to carbon of 3:1 in the membrane system. Steam which is one of the reactant is segregated across the catalytic volume to minimize the "slip" of undesired permeate of CO from the retentate to permeate volume.

The initial isothermal catalyst membrane design consists of two layers; one active for ethanol pyrolysis and methane steam reforming, and a second layer active for water-gas-shift reaction. The water-gas-shift catalytic layer is employed as a "clean-up" layer in lieu of a hydrogen permselective material. In the final design of composite catalytic membrane, an oxidation catalyst layer active for combustion of ethanol, CH_4, CO and H_2 is added. This catalyst layer is used as the point of heat source for the endothermic ethanol pyrolysis to achieve autothermal operation.

The first catalyst layer thickness is determined such that the Thiele modulus is 7.6, at which theoretically the centerline ethanol concentration is reduced to 0.1% of original

concentration. The second layer active for water-gas-shift reaction is designed with a Thiele modulus of 7.6 and separation factor of 0.1. In case of non-isothermal design oxidation layer is selected such that the centerline concentration of oxygen is 1 ppm by choosing a catalyst thickness of 5 μm. The summary of design specifications are presented in Table 4.2.

Table 4.2: Summary of design specifications for ethanol steam reforming.

	First Layer	**Second layer**	**Third layer**
Catalyst	Ni/Al_2O_3	CuO/Al_2O_3	Pt/Al_2O_3
Thickness (mm)	1.33	0.75	-
Catalyst activity factor, δ	1	0.45	1
Thiele modulus, Φ	7.6	7.6	-
Separation factor, ζ	0	0.1	-

4.2.5 Simulation strategy

Simulations are carried out over a range of feed flow rates and assuming equal sweep flow rates. The performance of individual membrane designs is investigated by simulating over a broad span of Damkohler number to evaluate the performance of catalytic membrane, encompassing both high apparent H_2:CO permselectivity and H_2 recovery regimes. The dimensionless Damkohler number is calculated based upon the initial rate of ethanol pyrolysis reaction and residence time as given by Eq. 4.7;

$$Da = \left(\frac{\eta\left(\Phi^I\right)\delta^I r_{C_2H_5OH}\left(p^F_{C_2H_5OH}, T_o\right)RT}{p^F_{C_2H_5OH}} \right) \left(\frac{F^F_{C_2H_5OH}}{V^F}\frac{RT}{P} \right)^{-1} \tag{4.7}$$

4.3 Numerical solution

The steady two-dimensional model developed is solved using the finite element method employing COMSOL Multiphysics v3.5 with chemical engineering module. A separate convection and conduction physics modules in 2-D radial symmetry are used to solve the mass and heat transfer equations. The retentate and permeate plug flow and solid-fluid mass transfer is described using partial differential equations (PDE) coefficient form. The heat transfer in the retentate and permeate volumes is described using weak-form boundary equations. These coupled physics equations are numerically solved using COMSOL Multiphysics with a finite element mesh of 25000 elements, 4.2×10^5 degrees of freedom. The mesh size is refined until the numerical solution met an atomic mass balances within 0.01% error. The present study employs the COMSOL solver prepackaged with a stationary Direct UMFPACK solver (v4.2) written by Timothy A. Davis [Davis, 2004, 1995], which employs an unsymmetric multifrontal method for solving sparse, unsymmetric systems. A Dell Precision WorkStation T7500 with Intel® Xeon® CPU X5670 @2.93GHz equipped with 24GB of RAM is used to solve all numerical simulations, with an approximate solution time of 15 minutes.

4.4 Analysis of simulation results

4.4.1 Catalytic membrane reactor

Individual simulation results are used to calculate several metrics to characterize the performance of the proposed membrane system. The reactor performance is evaluated in terms of an overall ethanol conversion, defined as

$$X_{C_2H_5OH} = \frac{F^F_{C_2H_5OH,o} - \left(F^F_{C_2H_5OH,e} + F^S_{C_2H_5OH,e}\right)}{F^F_{C_2H_5OH,e}} \times 100 \tag{4.8}$$

The performance of the catalytic membrane reactor for selective gas purification is

characterized in terms of hydrogen recovery (HR) and H_2:CO permselectivity.

Apparent H_2:CO permselectivity is defined in terms of molar flows of each species entering the retentate volume and exiting the permeate volume, as a gas purification membrane (GPM),

$$S^{GPM}_{H_2/CO} = \frac{\left(F^S_{H_2,o}/F^S_{CO,o}\right)}{\left(F^F_{H_2,e}/F^F_{CO,e}\right)} \tag{4.9}$$

Lastly, the percentage of total hydrogen recovered is determined from the outlet molar flows of hydrogen, thus accounting for both hydrogen supplied to the membrane for purification and the potential hydrogen to be produced via water-gas-shift,

$$HR = \frac{F^S_{H_2,e}}{F^F_{H_2,e} + F^S_{H_2,e}} \times 100 \tag{4.10}$$

The total percentile yields of hydrogen, methane, carbon monoxide and carbon dioxide are determined from the total outlet molar flows of sweep and feed volumes, defined as

$$Y_{H_2} = \frac{F^F_{H_2,e} + F^S_{H_2,e}}{3F^F_{C_2H_5OH,e}} \times 100 \tag{4.11a}$$

$$Y_{CH_4} = \frac{F^F_{CH_4,e} + F^S_{CH_4,e}}{2F^F_{C_2H_5OH,e}} \times 100 \tag{4.11b}$$

$$Y_{CO} = \frac{F^F_{CO,e} + F^S_{CO,e}}{2F^F_{C_2H_5OH,e}} \times 100 \tag{4.11c}$$

$$Y_{CO_2} = \frac{F^F_{CO_2,e} + F^S_{CO_2,e}}{2F^F_{C_2H_5OH,e}} \times 100 \tag{4.11d}$$

4.4.2 Packed bed reactor (PBR) calculations

The above metrics provide a fair comparison of the present catalytic membrane design to traditional catalytic membrane and packed-bed reactor designs for the purpose of CO removal from reformate mixtures. An analogous infinite packed bed reactor is modeled for reference purposes, and assuming a feed comprised of the feed inlet used for membrane reactor simulations. The ethanol conversion in the pyrolysis reaction is assumed to be 100%, the resultant gas mixture is allowed to react to equilibrium in methane steam reforming. The equilibrium gas mixture from the methane steam reforming is fed as inlet for water-gas-shift reaction and allowed to react at equilibrium conversion. The apparent H_2:CO permselectivity in an infinite packed bed reactor is defined as, $S^{PBR}_{H_2/CO} = \left(F^{PBR}_{H_2,e}/F^{PBR}_{CO,e}\right)$, which is determined as 9.64.

4.5 Results and discussion

4.5.1 Initial isothermal design

An initial isothermal model was simulated over a range of Damkohler number varying a uniform temperature of 873 K. These simulation results were then used to identify several design points and performance regions for guiding subsequent non-isothermal simulations.

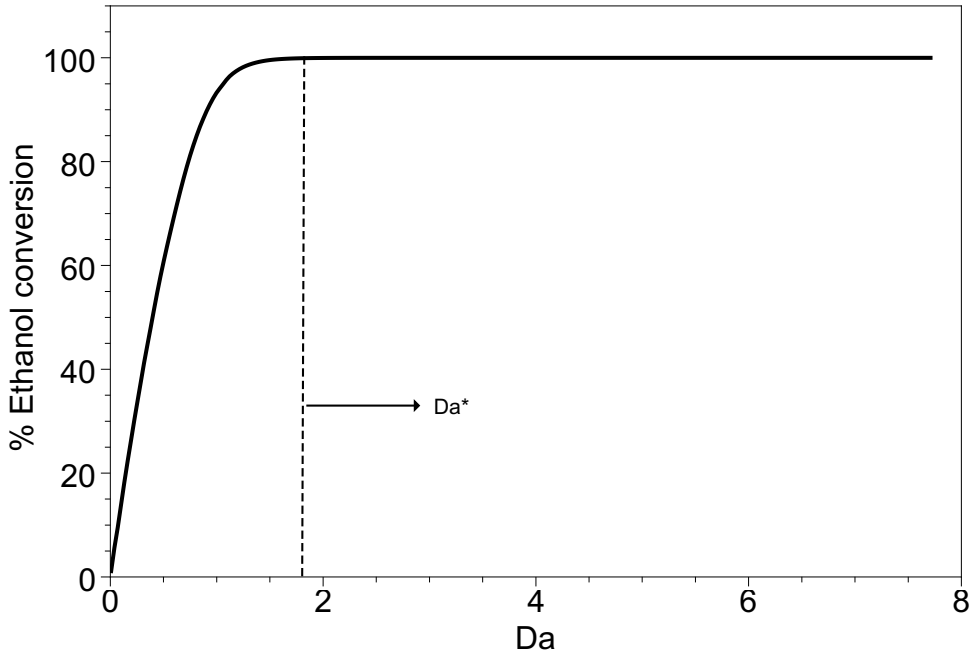

Figure 4.2: The percentile ethanol conversion versus Damkohler number, from isothermal simulations at 873 K.

Figure 4.2 shows the ethanol conversion varying the Damkohler number (Da) for isothermal design of two-layer composite catalytic membrane. The results show that ethanol conversion increases rapidly with increasing Damkohler number, owing to an increase in residence time for ethanol pyrolysis reaction. The figure identifies the first design point (Da*), the Damkohler number at which the ethanol conversion reaches 100% in the reactor.

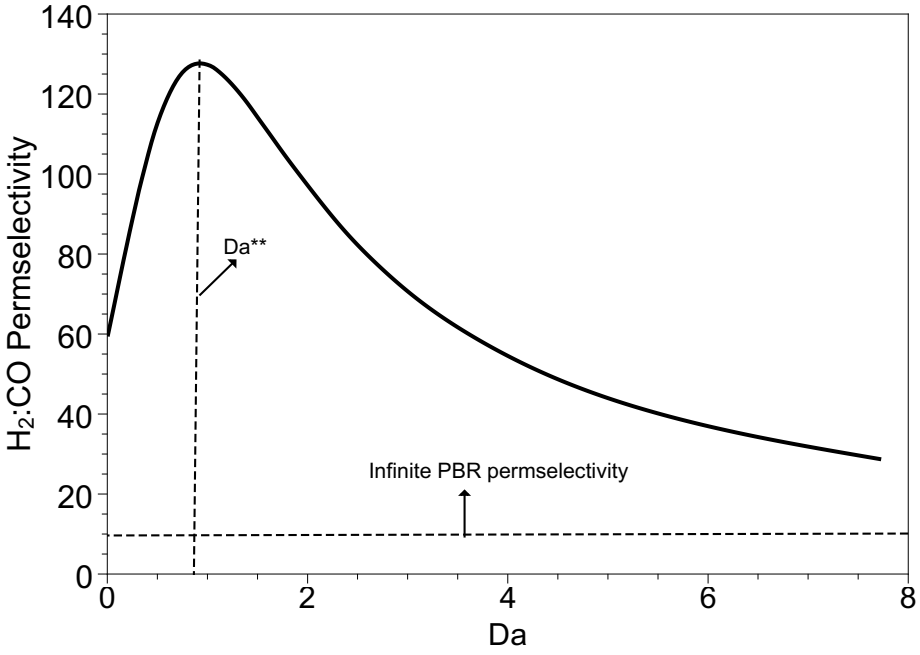

Figure 4.3: The H_2:CO permselectivity versus Damkohler number in isothermal simulations at 873 K.

Figure 4.3 presents the predicted performance of the isothermal, two-layer catalytic membrane in terms of apparent H_2:CO permselectivity while varying Damkohler number. Simulations predict an initial increase in apparent H_2:CO permselectivity to a maximum value of 122, occurring at a second design point (Da** = 1). However, with further increase in Damkohler number decreases the H_2:CO permselectivity. Figure 4.3 also identifies the design point Da***, which is the H_2:CO permselectivity that can be achieved in an infinite packed bed reactor.

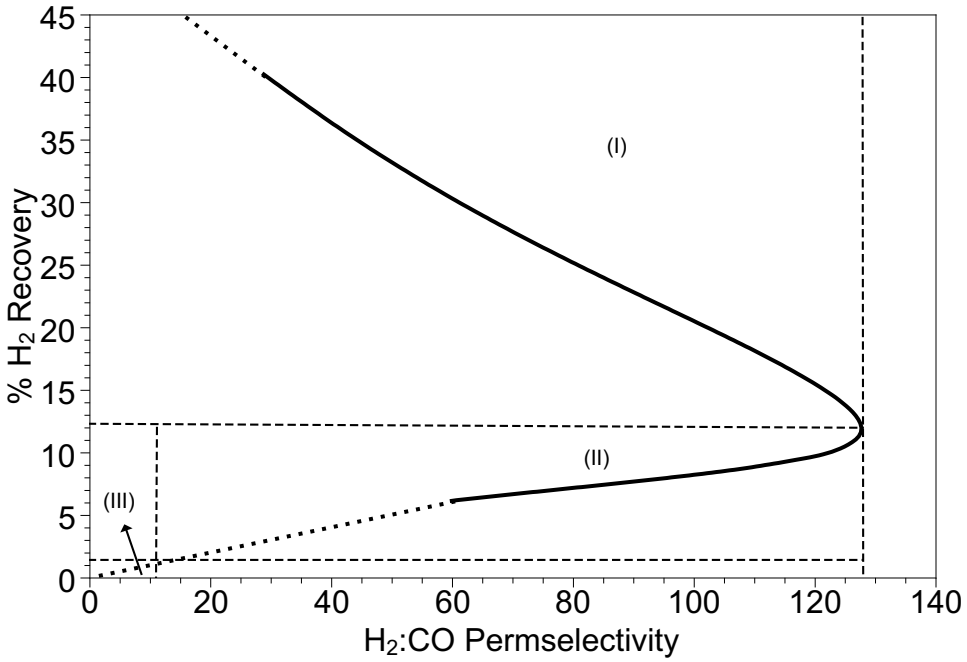

Figure 4.4: H_2:CO permselectivity versus H_2 recovery in isothermal simulations at 873 K.

Figure 4.4 summarizes the performance of the catalytic membrane system for gas purification by directly comparing H_2 recovery and apparent H_2:CO permselectivity. This figure identifies three performance zones showing the “trade-off" between H_2:CO permselectivity and hydrogen recovery varying the Damkohler number. In performance zone I, the results show high hydrogen recovery and also high H_2:CO permselectivity. In the zone II, the results show that optimal performance where there is competitive hydrogen recovery and H_2:CO permselectivity. In zone III, where the H_2:CO permselectivity is equal to that is determined to be obtainable in an infinite packed bed reactor. The results show that at the maximum permselectivity (second design point) the hydrogen recovery is about 12%.

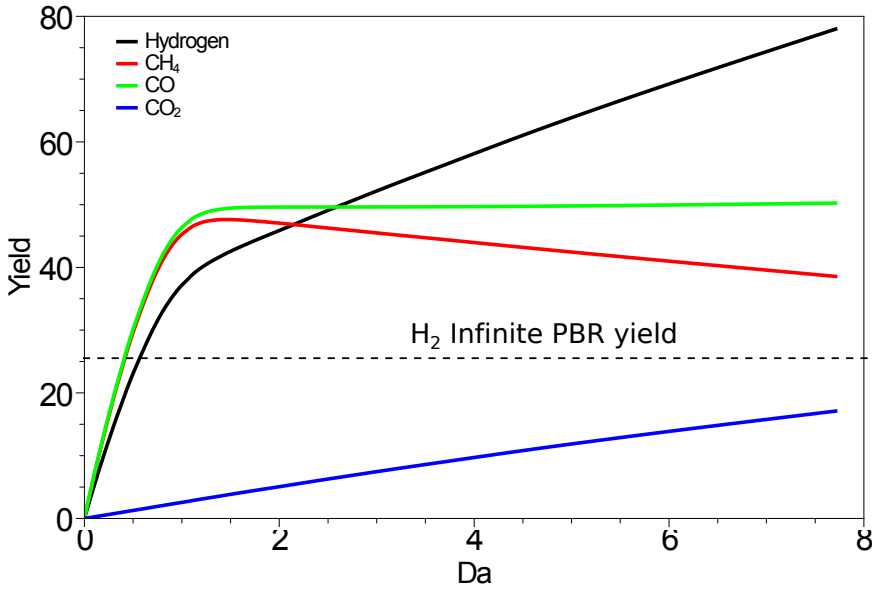

Figure 4.5: The overall yields of gas species for isothermal simulations at 873 K.

Figure 4.5 shows the overall yields of H_2, CO, CO_2 and CH_4 from the simulation results varying the Damkohler number. The results how that all gas species yields increase with increasing Damkohler number. The overall product yield of CO increases with increasing the Damkohler reaching a maximum and further increase of Damkohler number decreases the CO yield.

4.5.2 Non isothermal design

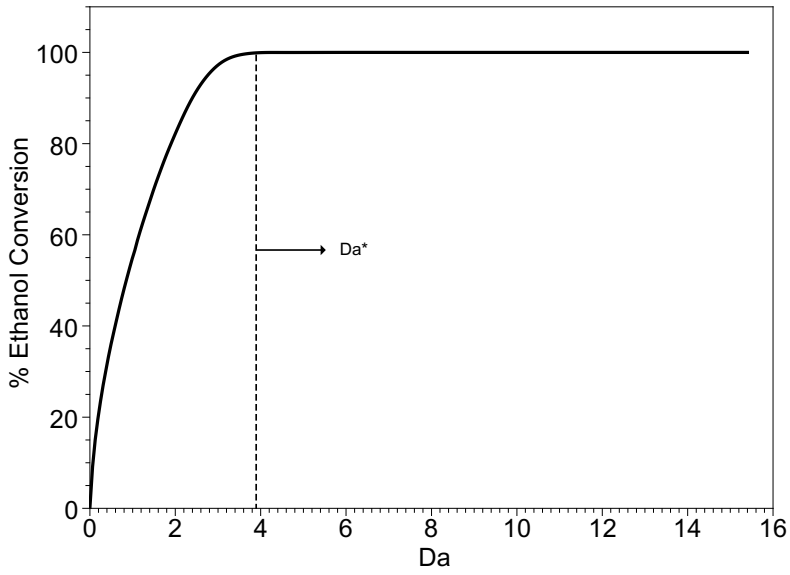

Figure 4.6: The percentile ethanol conversion versus Damkohler number in non isothermal adiabatic simulations, feed and sweep volumes are at 873 K.

Figure 4.6 shows the ethanol conversion varying Damkohler number for non-isothermal adiabatic design of two-layer composite catalytic membrane. Results show that ethanol conversion increases rapidly with increasing the Damkohler number owing to increase in residence time for ethanol pyrolysis reaction. The comparison between isothermal results at 873 K and non-isothermal results show that complete ethanol conversion occurs at a high Damkohler number implying that a high residence time required. Figure 4.6 identifies first design point, Damkohler number at which ethanol conversion reaches 100% in the reactor. This decrease in ethanol conversion is owing to the endothermic affect of

pyrolysis reaction.

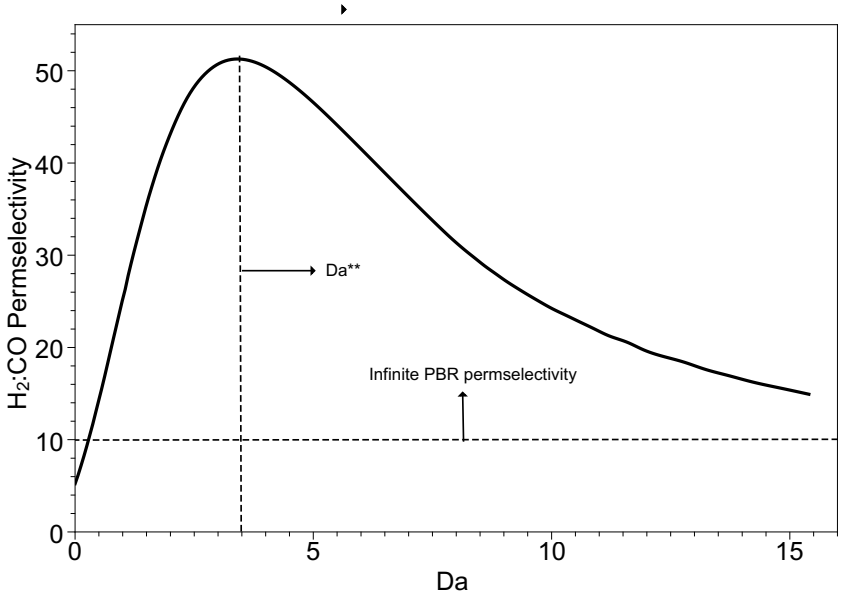

Figure 4.7: The H_2:CO permselectivity versus Damkohler number in non isothermal adiabatic simulations, feed and sweep volumes are at 873 K.

Figure 4.7 presents the performance of catalytic membrane in terms of permeate H_2:CO apparent permselectivity varying the Damkohler number for the non-isothermal design at 873 K. The results show a similar trend observed in isothermal design, permeate H_2:CO apparent permselectivity increases rapidly with increase in the Damkohler number reaching a maxima and further increase in Damkohler number results in decrease of permselectivity. However, the maximum H_2:CO permselectivity is less than that of isothermal design. Figure 4.7 identifies a second design point at which maximum H_2:CO permselectivity occurs. A maximum H_2:CO permselectivity of 43 is observed at a Damkohler number of 5.

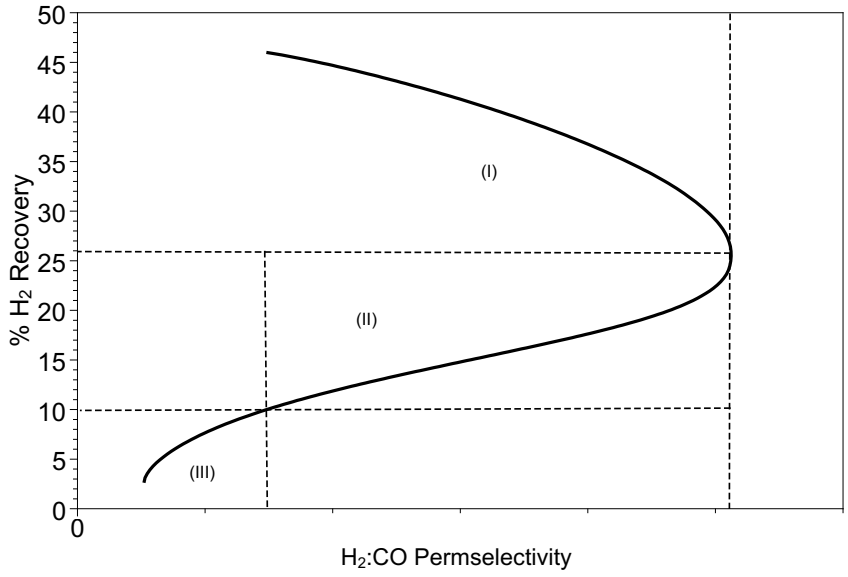

Figure 4.8: H_2:CO permselectivity versus H_2 recovery in non isothermal adiabatic simulations, feed and sweep volumes are at 873 K.

Figure 4.8 summarizes the performance of catalytic membrane system by comparing H_2:CO permselectivity and H_2 recovery for a non-isothermal adiabatic design. The results show a similar trend to that of isothermal design, however, lower permselectivities. The same analysis as in isothermal case shows the three performance zones showing, the "trade-off" between H_2:CO permselectivity and hydrogen recovery. In the performance zone I, the results show that low hydrogen recovery and also low H_2:CO permselectivity. In the zone II, the results show optimal performance where there is competitive hydrogen recovery and H_2:CO permselectivity. The simulations show that maximum H_2:CO permselectivity is observed to be 44 with hydrogen recovery about 35%.

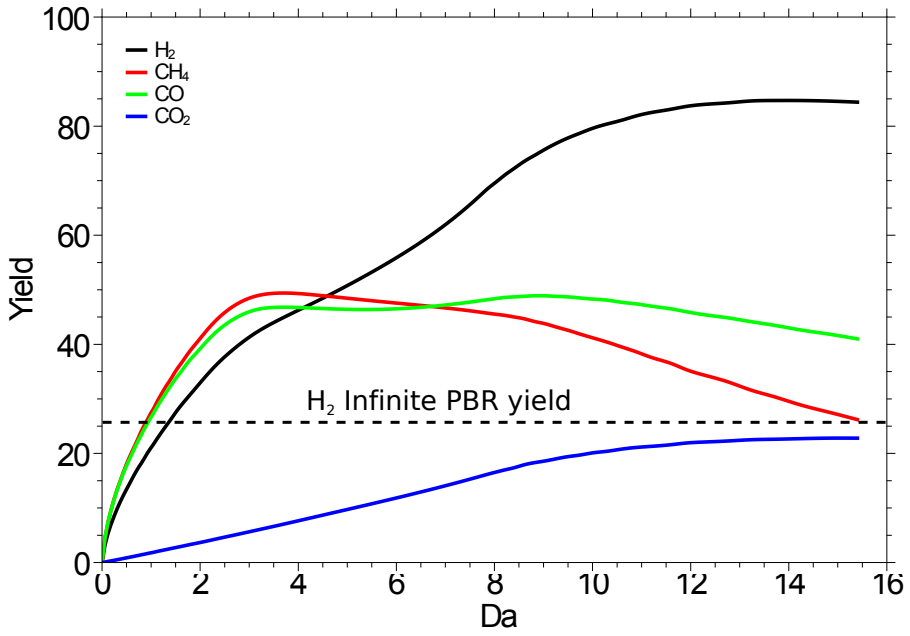

Figure 4.9: The overall yields of gas species in non isothermal adiabatic simulations, feed and sweep volumes are at 873 K.

Figure 4.9 shows the overall yields of H_2, CO, CO_2 and CH_4 from the simulation results varying the Damkohler number. The results how that all gas species yields increase with increase in the Damkohler number. The overall product yield of CO and CO_2 increases with increasing the Damkohler number reaching a maximum and further increase of Damkohler number decreases the CO yield.

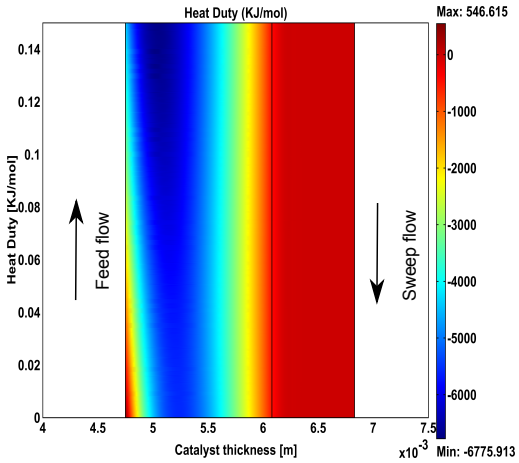

Figure 4.10: Heat duty calculated based on rate of reactions and heat of reactions inside the catalyst.

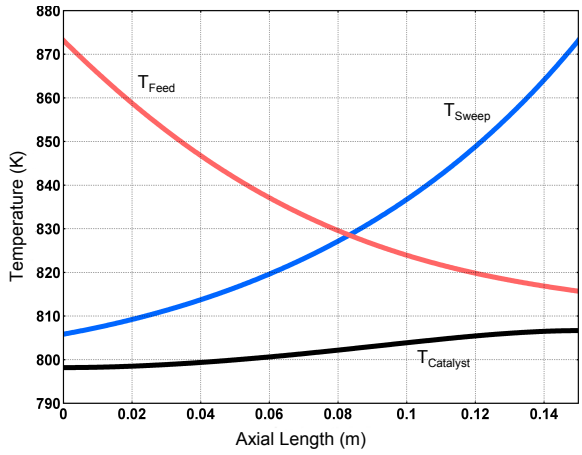

Figure 4.11: Temperature profiles inside the catalyst in non isothermal simulations.

Figure 4.10 shows the heat duty inside the catalyst membrane for two layer non isothermal simulations. The results show the negative heat duty in the first catalyst layer active for ethanol pyrolysis and methane steam reforming. The second catalyst layer active for water-gas-shift reaction shows a positive heat duty due to exothermic nature of the reaction.

Figure 4.11 shows the temperature profiles in the feed, sweep and catalyst layers along the axial length of the reactor. The feed and sweep temperatures decrease along the axial length of the reactor (note that the feed and sweep are in countercurrent flow operation). The temperature inside the catalyst is also decreases to a lower than the initial feed and sweep values.

Figure 4.12a shows the comparison of simulation results predicting percentile ethanol conversion predicted in both isothermal and non-isothermal models. The results predicts a decreased ethanol conversion at lower Damkohler numbers, isothermal model reaches 100% at lower Damkohler number, while at a higher Damkohler number. Figure 4.12b shows the comparison of simulation results predicting H_2:CO permselectivity predicted in both isothermal and non-isothermal models. Both results predict a similar trends, while the isothermal model predicting a higher maxima of H_2:CO permselectivity at lower Damkoher number. Figure 4.12c shows the comparison of simulation results predicting H_2:CO permselectivity versus H_2 predicted in both isothermal and non-isothermal models. The results show similar trend while lower H_2:CO permselectivity and H_2 recoveries.

(a) Ethanol conversion

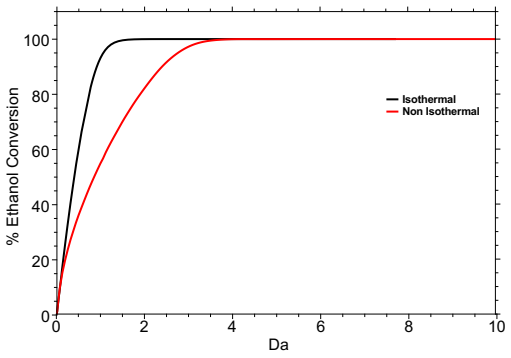

(b) H_2:CO permselectivity

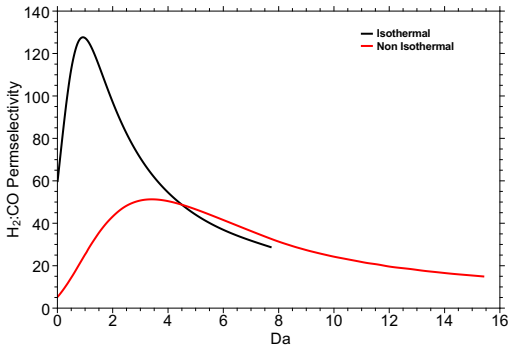

(c) H_2:CO permselectivity versus H_2 recovery

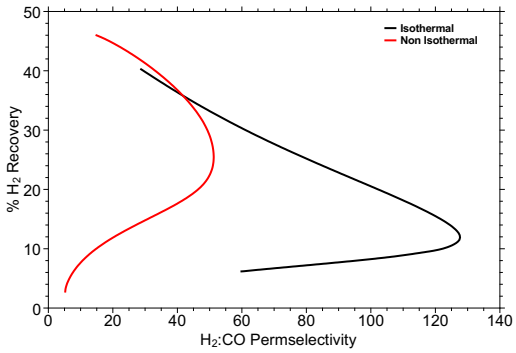

Figure 4.12: Comparison of isothermal and non-isothermal results at varying Damkohler numbers.

4.5.3 Non-isothermal design with addition of combustion

The analysis of results in two-layer non-isothermal model confirms that there is negative heat duty due to ethanol pyrolysis and methane steam reforming reactions. This negative heat duty can be counteracted with an addition of a catalyst layer active for combustion. This catalyst layer (active for combustion of CO, CO_2, CH_4, ethanol, and H_2) is added to counteract the negative heat duty inside the catalyst membrane. It is hypothesized that by controlling the oxygen content in the retentate inlet, an autothermal operation can be achieved. This hypothesis is evaluated using three design configurations (Table 4.3) placing the combustion catalyst at each of the three boundaries of the two-layer model.

Table 4.3: Configuration matrix of autothermal model designs.

Autothermal	Layer 1 (feed side)	Layer 2 (middle)	Layer 3 (sweep side)
Case 1	Combustion	Ethanol Pyrolysis	WGS reaction
Case 2	Ethanol reforming	Combustion	WGS reaction
Case 3	Ethanol reforming	WGS reaction	Combustion

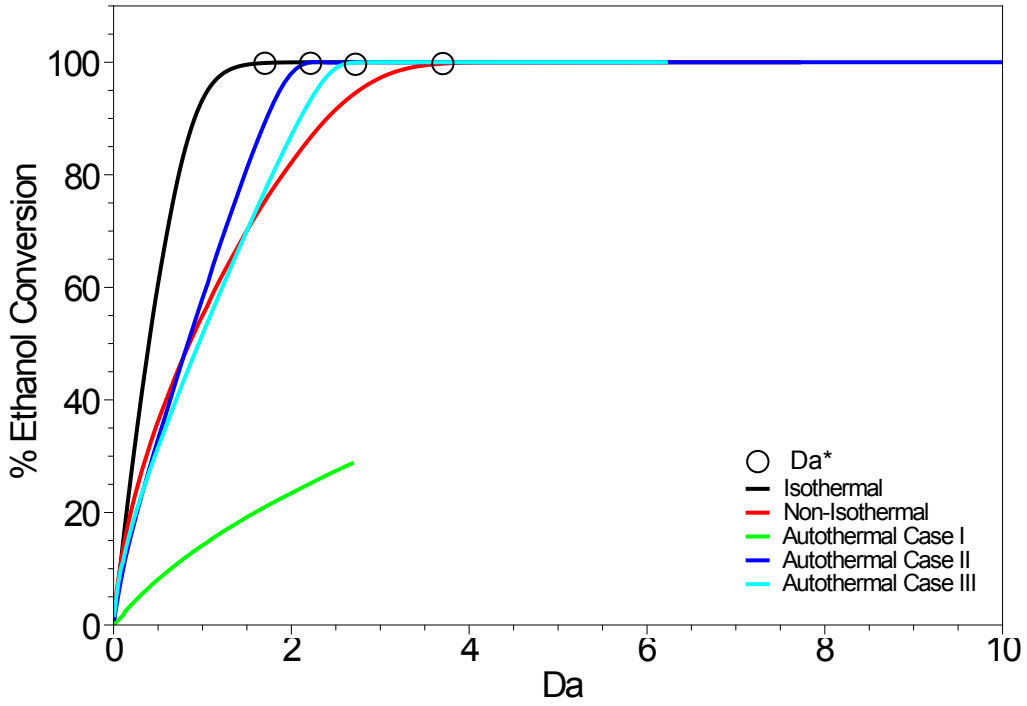

Figure 4.13: Ethanol conversion vs Damkohler number for catalytic membrane reactor for different cases, autothermal, isothermal and non-isothermal.

Figure 4.13 shows the ethanol conversion predicted by simulations in three autothermal cases and compared with two layer isothermal and non-isothermal results. Results show similar trends in each case, the ethanol conversion increases with an increase in Damkohler number. Ethanol conversion reaches 100% in all cases except the autothermal case 3, in which the maximum H_2:CO permselectivity is reached before complete conversion of ethanol.

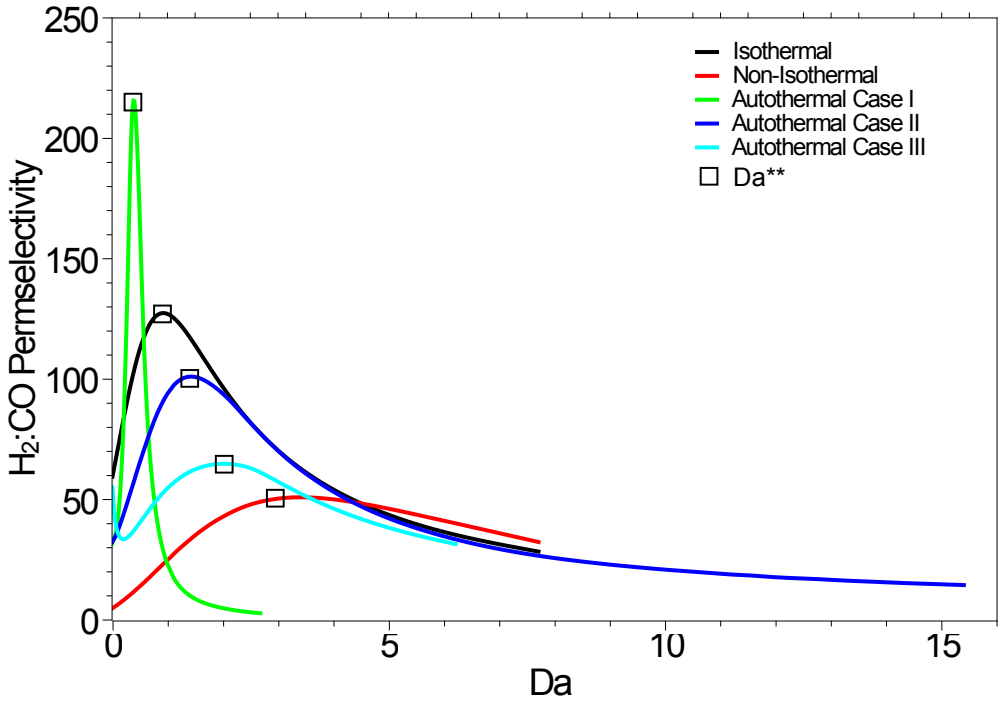

Figure 4.14: H_2:CO apparent permselectivity versus Damkohler number for catalytic membrane reactor for different cases, autothermal, isothermal and non-isothermal.

Figure 4.14 shows the apparent H_2:CO permselectivities obtained in three autothermal cases and comparison with isothermal and non-isothermal cases, while varying the Damkohler number. Results predict similar trends in each case, the H_2:CO permselectivities increases with increasing Damkohler number reaching a maxima (different in each case), then decreases with further increase in Damkohler number.

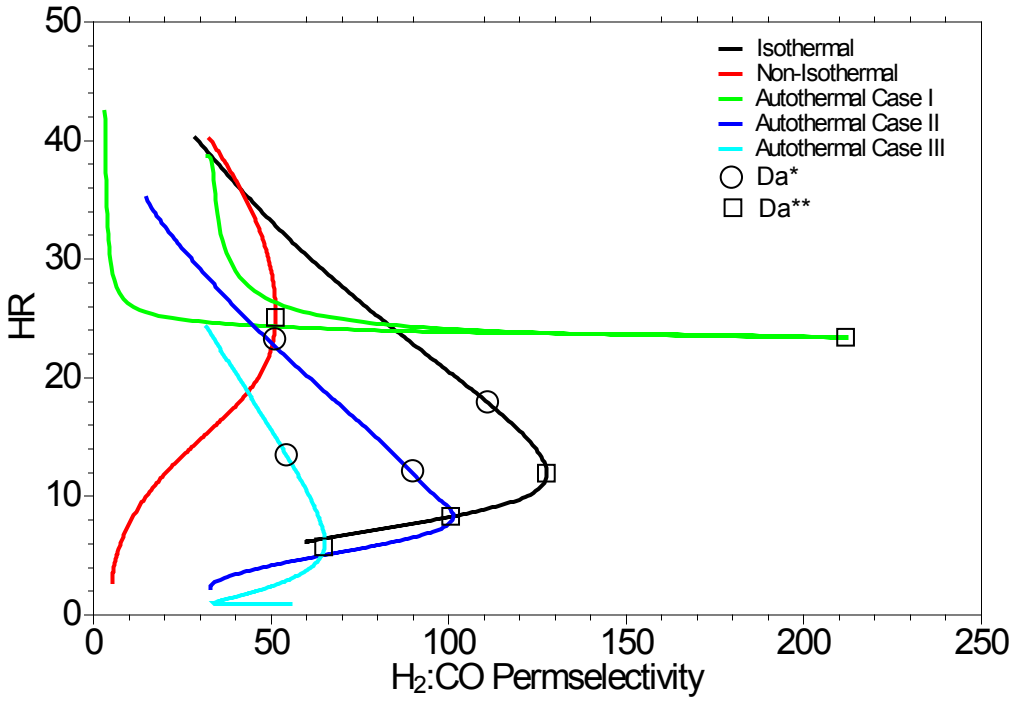

Figure 4.15: H_2:CO apparent permselectivity versus H_2 recovery for catalytic membrane reactor for different cases, autothermal, isothermal and non-isothermal.

Figure 4.15 shows the performance of the catalyst membrane reactor, by directly comparing the H_2:CO permselectivity with percentile hydrogen recovery for different autothermal cases, isothermal and non-isothermal models. Results show similar performance zones identified in the initial isothermal case. Case 1 gives the best performance with maximum H_2:CO permselectivity $>$ 200:1 at 25% H_2 recovery. Case 2 gives the closest performance, with maximum H_2:CO permselectivity of 100:1 at 8% recovery. Finally, the case 3 gives the worst performance, maximum H_2:CO permselectivity of 60:1 at 6% recovery. The above analysis shows that addition of combustion catalyst, the endothermic effect of endothermic ethanol pyrolysis and methane steam reforming reaction can be

mitigated and an autothermal performance can be achieved.

4.6 Conclusions

A composite catalytic membrane with multiple catalyst layers active for one or more reactions were investigated for selective hydrogen extraction from bioethanol steam reforming. Isothermal and non-isothermal models were developed and numerically solved to evaluate the hypothesis that reaction, diffusion and thermal gradients can be manipulated to achieve hydrogen purification without any hydrogen permselective materials. Results show the potential of this concept for cost-effective hydrogen separation. A two layer isothermal model results show that promising apparent H_2:CO permselectivities around 100 can be achieved at a permeate hydrogen recovery about 15% at appropriate design conditions. Two layer non-isothermal results show a reduction in the performance of the catalyst membrane owing to endothermal reaction. A preliminary study of autothermal model is also investigated employing an additional combustion catalyst layer active for oxidation of all chemical species. Three design configuration varying the location of combustion catalyst is investigated, results show the potential of achieving autothermal operation with performance similar to isothermal design.

5. CONCLUSIONS AND RECOMMENDATIONS

5.1 Conclusions

A novel application to designing catalytic membranes for high-purity hydrogen extraction from bioethanol reforming was investigated. The hypothesis that high-purity hydrogen purification can be achieved by manipulating reaction-diffusion phenomena and thermal gradients inside a catalyst without employing any hydrogen permselective materials was demonstrated using a catalytic membrane reactor with segregated reactants. This hypothesis was investigated in two parts: (1) a water-gas-shift catalytic membrane reactor for purification of a reformate mixture, (2) hydrogen extraction from bioethanol reforming.

In chapter 2, a two dimensional steady state model was developed to describe a water-gas-shift catalytic membrane reactor for a feed of typical diesel reformate gas mixture (9 mol% CO, 3 mol%CO_2, 28 mol% H_2 and 15 mol% H_2O) employing a shell-tube configuration. Isothermal results at 773 K show apparent CO:H_2 permselectivities of 90:1 to >200:1 at permeate H_2 recoveries of 20% up to 40% can be achieved at appropriate design and operating conditions. A parametric analysis is performed varying two parameters, Thiele modulus (Φ) and separation factor (ζ) and two design criteria are identified for achieving an optimum membrane performance at $\Phi = 7.6$ and $\zeta < 0.4$. Non-isothermal adiabatic simulations indicate that accumulation of reaction heat reduces the membrane performance; however this can be mitigated by external imposition of counter thermal gradient.

In chapter 3, an experimental demonstration of a catalytic membrane reactor for hydrogen separation from a diesel reformate gas-mixture (4.5 mol% CO, 1.5 mol%, CO_2, 7.5 mol% H_2, 14 mol% H_2O). The gas permeation test has shown that the pore diameter of catalyst coating is 246 nm. Results demonstrate that a microporous catalytic membrane

is capable of achieving a maximum H_2:CO permselectivity of 12 with a hydrogen recovery above 50%. The experimental results were compared with modeling results of similar pore diameter, it is observed that the trends qualitatively and quantitatively with an error.

In chapter 4, a composite catalytic membrane with multiple catalyst layers active for one or more reactions were investigated for selective hydrogen extraction from (16 mol%) bioethanol reforming. The simulation results show the potential of this concept for cost-effective hydrogen separation. A two-layer isothermal simulation results at 873 K show that promising apparent H_2:CO permselectivities around 100 can be achieved at a permeate hydrogen recovery about 15% at appropriate design conditions. Two layer non-isothermal adiabatic simulation results have shown a reduction in the performance of the catalyst membrane owing to endothermic reaction. A preliminary study of autothermal model is also investigated employing an additional combustion catalyst layer active for oxidation of all chemical species. Three design configuration varying the location of combustion catalyst is investigated, results show the potential of achieving autothermal operation with performance similar to isothermal design.

The successful demonstration of this composite catalytic membrane concept paves a path for cost-effective hydrogen purification from not only bioethanol, but also from a variety of other reforming fuels. This represents a potential breakthrough in gas separation technology, which may be extended to other gas separation applications currently limited by permselective materials. This research also provides fundamental insights into the design of multilayer catalysts for autothermal operation or manipulation of reaction selectivity.

5.2 Recommendations

This research demonstrated the hypothesis that hydrogen purification can be achieved without employing any permselective material. Further work is recommended for extend-

ing this concept to other reforming fuels (methanol, glycerol, diesel or natural gas), as well as providing an improved experimental demonstration of this new technology.

- The thesis hypothesis was demonstrated using a catalytic membrane reactor employing Fick's single component model for describing the reaction and diffusion in the catalyst.

- Addition of a multicomponent diffusion model in the catalyst either Stefan-Maxwell expressions, or Dusty-Gas-Model) would allow accounting for complex diffusional effects and allow inclusion of externally-applied pressure differentials across the catalyst membrane.

- A comparison of isothermal simulation results predicted using Fick's diffusion model and Stefan-Maxwell multicomponent diffusion model is presented in Appendix A. The model presented in Appendix A can be extended to include non-isothermal affects, external pressure gradients and external thermal gradients varying the catalyst pore diameter.

- An optimization to determine the optimal distribution of combustion catalyst layer and extent of oxidation reaction for autothermal operation of composite catalytic membrane reactor. In this Thesis, it is shown that for three cases the combustion catalyst layer is placed at three logical boundaries of the catalyst (at the feed side, in the middle, and at the sweep side). However, the combustion catalyst layer can be distributed between the catalyst layer, for example, it can be placed in the middle of ethanol pyrolysis catalyst layer. A mathematical code may be developed to optimize this location as a function of autothermal operation, or other parameter such as H_2 permselectivity and H_2 recovery.

- Study the affect of concentration polarization, axial mixing in the retentate and permeate volumes (in lieu of assuming plug flow) by extending the 2-D model presented in this Thesis.

- Develop a 3 dimensional computation fluid dynamics (CFD) model to describe the affects of axial mixing in the retentate and permeate volumes.

- Experimentally demonstrate the composite catalytic membrane reactor for bioethanol by refining the catalyst coating techniques developed in Chapter 3 for water-gas-shift catalytic membrane reactor. The catalyst coating can be refined by dip-coating by using a porous stainless steel substrate (PSS) with a lower pore diameter and smoother surface than the one employed in this Thesis, thus reducing the formation of pin holes or cracks.

NOMENCLATURE

$\tilde{a}^{F,S}$	Ratio of membrane surface area to fluid volume, m^{-1}
$\tilde{n}$	Normal surface vector, dimensionless
$A_C^{F,S}$	Cross sectional area for flow, m^2
A_{mem}	Membrane surface area, m^2
C_i	Molar concentration of species i, $\mathrm{mol\,m}^{-3}$
$C_{p,i}$	Specific heat capacity of gas species i, $\mathrm{J\,mol}^{-1}\,\mathrm{K}^{-1}$
$C_{P,mix}$	Specific heat capacity of gas mixture, $\mathrm{J\,mol}^{-1}\,\mathrm{K}^{-1}$
D	Diffusivity of gas mixture, $\mathrm{m}^2\,\mathrm{s}^{-1}$
d_p	Catalyst pore diameter, m
d_t	Diameter of tube/annulus, m
$D_{K,i}^{eff}$	Effective Knudsen diffusivity of gas species i, $\mathrm{m}^2\,\mathrm{s}^{-1}$
$F_i^{F,S}$	Feed/Sweep molar flow rate of species i, $\mathrm{mol\,s}^{-1}$
h^F	Fluid-wall heat transfer coefficient at retentate-catalyst boundary, $\mathrm{J\,m}^{-2}\,\mathrm{K}^{-1}\,\mathrm{s}^{-1}$
h^S	Fluid-wall heat transfer coefficient at permeate-catalyst boundary, $\mathrm{J\,m}^{-2}\,\mathrm{K}^{-1}\,\mathrm{s}^{-1}$
k_{cat}	Effective thermal conductivity of catalyst, $\mathrm{J\,m}^{-1}\,\mathrm{s}^{-1}\,\mathrm{K}^{-1}$
k_{gas}	Thermal conductivity of gas mixture, $\mathrm{J\,m}^{-1}\,\mathrm{s}^{-1}\,\mathrm{K}^{-1}$
k_{gs}	Mass transfer coefficient at gas-solid interface, $\mathrm{mol\,m}^2\,\mathrm{s}^{-1}$

k_{solid}	Thermal conductivity of solid, $\mathrm{J\,m^{-1}\,s^{-1}\,K^{-1}}$
M_i	Molecular weight of species i, $\mathrm{kg\,mol^{-1}}$
P	Total pressure within the catalytic membrane system, Pa
p_i	Partial pressure of species i, Pa
R	Universal gas constant, $\mathrm{J\,mol^{-1}\,K^{-1}}$
$r_{C_2H_5OH,o}$	Initial rate of reaction of ethanol, $\mathrm{mol\,m^{-3}\,s^{-1}}$
r_{ij}	Net rate of reaction of species i in catalyst layer j, $\mathrm{mol\,m^{-3}\,s^{-1}}$
$r_{WGS,o}\left(p_{i,o},T\right)$	Initial rate of reaction of water-gas-shift reaction, $\mathrm{mol\,m^{-3}\,s^{-1}}$
T	Temperature of the catalytic membrane system, K
t_{mem}^{WGS}	Thickness of WGS catalyst layer, m
u	Velocity of fluid mixture, $\mathrm{m\,s^{-1}}$
V^F	Retentate volume, $\mathrm{m^3}$
V_{mem}	Membrane volume, $\mathrm{m^3}$
x_i	Mole fraction of species i, dimensionless
z	Catalyst length in z direction, m

Greek Letters

δ^i	Catalyst activity factor of catalyst layer i, dimensionless
$\eta\left(\Phi^{II}\right)$	Catalyst effectiveness factor, dimensionless
μ_i	Viscosity of pure gas species i, Pa s

μ_{mix}	Viscosity of gas mixture, Pa s
Ω_{μ}	Lennard-Jones parameter for determining gas viscosity
Φ^{III}	Thiele modulus of catalyst layer 3, dimensionless
Φ^{II}	Thiele modulus of catalyst layer 2, dimensionless
Φ^{I}	Thiele modulus of catalyst layer 1, dimensionless
ρ	Density of the gas mixture, kg m^{-3}
σ	Lennard-Jones parameter for determining gas viscosity
τ	Catalyst tortuosity, dimensionless
$\triangle H_j^o$	Net heat of reaction in catalyst layer j, J mol^{-1}
ε	Catalyst porosity, dimensionless
ζ	Separation factor, dimensionless

Subscripts/Superscripts

cat	Catalyst volume
e	outlet/exit
F	Feed volume
o	Inlet
S	Sweep volume

REFERENCES

Adhikari, S. and S. Fernando. Hydrogen membrane separation techniques. *Ind. Eng. Chem. Res.*, 45(3):875–881, 2006.

Alexander Stern, S. Polymers for gas separations: the next decade. *J. Memb. Sci.Mem. Sci.*, 94(1):1–65, 1994.

Alves, J. J. and G. P. Towler. Analysis of refinery hydrogen distribution systems. *Ind. Eng. Chem. Res.*, 41(23):5759–5769, 2002.

Amphlett, J., R. Mann, and B. Peppley. On board hydrogen purification for steam reformation/PEM fuel cell vehicle power plants. *Int. J. Hydrogen Energy*, 21(8):673–678, 1996.

Aris, R. The mathematical theory of diffusion and reaction in permeable catalysts, volume I. Clarendon Press, London, 1975.

Armaroli, N. and V. Balzani. The hydrogen issue. *ChemSusChem*, 4(1):21–36, 2011.

Aubé, F. and H. Sapoundjiev. Mathematical model and numerical simulations of catalytic flow reversal reactors for industrial applications. *Comput. Chem. Eng.*, 24(12):2623–2632, 2000.

Baade, W. F., U. N. Parekh, and V. S. Raman. Hydrogen. In Kirk-Othmer Encycl. Chem. Technol., volume 13. John Wiley & Sons, Inc., 2001.

Bagotsky, V. S. Alkaline fuel cell. In Fuel Cells Probl. Solut., chapter 6, pages 109–124. John Wiley & Sons, Inc., Hoboken, NJ, USA, 1997.

Balat, H. and E. Kırtay. Hydrogen from biomass – Present scenario and future prospects. *Int. J. Hydrogen Energy*, 35(14):7416–7426, 2010.

Ball, M., W. Weindorf, and U. Bunger. Hydrogen production. In Ball, M. and M. Wietschel, editors, A Hydrog. Econ. Oppor. challenges, chapter 10, pages 303–334. Cambridge University Press, New York, 2005.

Baschuk, J. J. and X. Li. Carbon monoxide poisoning of proton exchange membrane fuel cells. *Int. J. Energy Res.*, 25(8):695–713, 2001.

Bernardo, P., E. Drioli, and G. Golemme. Membrane gas separation: A review/state of the art. *Ind. Eng. Chem. Res.*, 48(10):4638–4663, 2009.

Biegler, L. T., L. Jiang, and V. G. Fox. Recent advances in simulation and optimal design of pressure swing adsorption systems. *Sep. Purif. Rev.*, 33(1):1–39, 2004.

Bird, R., W. Stewart, and E. Lightfoot. Transport phenomena. Wiley, New York, second edition, 2007.

Bruijn, F. D. and D. Papageorgopoulos. The influence of carbon dioxide on PEM fuel cell anodes. *J. Power Sources*, 110(1):117–124, 2002.

Butt, J. B. Thermal conductivity of porous catalysts. *AIChE J.*, 11(1):106–112, 1965.

Carberry, J. J. The micro-macro effectiveness factor for the reversible catalytic reaction. *AIChE J.*, 8(4):557–558, 1962.

Champagnie, A. M., T. T. Tsotsis, R. G. Minet, and E. Wagner. The study of ethane dehydrogenation in a catalytic membrane reactor. *J. Catal.*, 134(2):713–730, 1992.

Champagnie, A., T. T. Tsotsis, R. Minet, and A. Webster. A high temperature catalytic membrane reactor for ethane dehydrogenation. *Chem. Eng. Sci.*, 45(8):2423–2429, 1990.

Chaubey, R., S. Sahu, O. O. James, and S. Maity. A review on development of industrial processes and emerging techniques for production of hydrogen from renewable and sustainable sources. *Renew. Sustain. Energy Rev.*, 23:443–462, 2013.

Cheng, X., Z. Shi, N. Glass, L. Zhang, J. Zhang, D. Song, Z.-S. Liu, H. Wang, and J. Shen. A review of PEM hydrogen fuel cell contamination: Impacts, mechanisms, and mitigation. *J. Power Sources*, 165(2):739–756, 2007.

Courty, P. and A. Chauvel. Catalysis, the turntable for a clean future. *Catal. today*, 29 (1–4):3–15, 1996.

Curtiss, C. F. and R. B. Bird. Multicomponent diffusion. *Ind. Eng. Chem. Res.*, 38(7): 2515–2522, 1999.

Davis, T. A. Umfpack user guide. *Website: http://www. cise. ufl. edu/research/sparse/umfpack/(1994–2009)*, 1995.

Davis, T. A. A column pre-ordering strategy for the unsymmetric-pattern multifrontal method. *ACM Trans. Math. Softw.*, 30(2):165–195, 2004.

de Lange, R., J. Hekkink, K. Keizer, and A. Burggraaf. Formation and characterization of supported microporous ceramic membranes prepared by sol-gel modification techniques. *J. Memb. Sci.*, 99(1):57–75, 1995.

de Lange, R., J. Hekkink, K. Keizer, and A. Burggraaf. Permeation and separation studies on microporous sol-gel modified ceramic membranes. *Microporous Mater.*, 4(2-3):169–186, 1995.

de Lange, R., K. Keizer, and A. Burggraaf. Analysis and theory of gas transport in microporous sol-gel derived ceramic membranes. *J. Memb. Sci.*, 104(1–2):81–100, 1995.

de Vos, R. M. and H. Verweij. High-selectivity, high-flux silica membranes for gas separation. *Science*, 279(5357):1710–1711, 1998.

Department of Energy, Hydrogen and our energy future. Technical report, U.S. Department of Energy Hydrogen Program, 2009.

Dicks, A. L. Molten carbonate fuel cells. *Curr. Opin. Solid State Mater. Sci.*, 8(5):379–383, 2004.

Dixon, A. G. Membrane reactors. *Catalysis*, 14:40–92, 1999.

Dixon, A. G. and D. L. Cresswell. Theoretical prediction of effective heat transfer parameters in packed beds. *AIChE J.*, 25(4):663–676, 1979.

Dutta, S. A review on production, storage of hydrogen and its utilization as an energy resource. *J. Ind. Eng. Chem.*, In Press(-):n/a–n/a, 2013.

EG&G Technical Services, Fuel cell handbook. Technical Report November, U.S. Department of Energy, Morgantown, West Virginia, 2004.

Erisman, J. W., M. A. Sutton, J. Galloway, Z. Klimont, and W. Winiwarter. How a century of ammonia synthesis changed the world. *Nature Geoscience*, 1(10):636–639, 2008.

Fairbanks, D. F. and C. R. Wilke. Diffusion coefficients in multicomponent gas mixtures. *Ind. Eng. Chem.*, 42(3):471–475, 1950.

Fick, A. Ueber diffusion. *Ann. Phys.*, 170(1):59–86, 1855.

Forsberg, C. Future hydrogen markets for large-scale hydrogen production systems. *Int. J. Hydrogen Energy*, 32(4):431–439, 2007.

Friedrich, K. A., F. N. Büchi, Z. P. Li, G. Kiesgen, D. C. Leinhos, H. S. Rottengruber, R. C. B. Jr., and B. V. Ratnakumar. Applications. In Züttel, A., A. Borgschulte, and L. Schlapbach, editors, Hydrog. as a Futur. Energy Carr., chapter 8. 2008.

Fuelcells.org, Fuel cell vehicles (from auto manufacturers) url: http://www.fuelcells.org/uploads/carchart.pdf. 2013.

Fuller, N. E., P. D. Schettler, and C. J. Giddings. A new method for prediction of binary gas-phase diffusion coefficients. *Ind. Eng. Chem.*, 58(5):19–27, 1966.

Funk, J. E. and R. M. Reinstrom. Energy requirements in production of hydrogen from water. *Ind. Eng. Chem. Process Des. Dev.*, 5(3):336–342, 1966.

Galbe, M. and G. Zacchi. A review of the production of ethanol from softwood. *Appl. Microbiol. Biotechnol.*, 59(6):618–628, 2002.

Gallucci, F., E. Fernandez, P. Corengia, and M. van Sint Annaland. Recent advances on membranes and membrane reactors for hydrogen production. *Chem. Eng. Sci.*, 92(0): 40–66, 2013.

Geankoplis, C. Transport processes and unit operations. Prentice-Hall International, Inc., Englewood Cliffs, New Jersy, third edition, 1993.

Goldemberg, J. Ethanol for a sustainable energy future. *Science*, 315(5813):808–10, 2007.

Grande, C. a. Advances in pressure swing adsorption for gas separation. *ISRN Chem. Eng.*, 2012:1–13, 2012.

Gulzow, E. Alkaline fuel cells. *Fuel Cells*, 4(4):251–255, 2004.

Habashi, F. Recent trends in extractive metallurgy. *J. Min. Metall. Sect. B Metall.*, 45(1): 1–13, 2009.

Haber, F. The synthesis of ammonia from its elements. *Resonance*, 2002.

Hallale, N. and F. Liu. Refinery hydrogen management for clean fuels production. *Adv. Environ. Res.*, 6(1):81–98, 2001.

Hallale, N., I. Moore, and D. Vauk. Hydrogen: Liability or asset? *Chem. Eng. Prog.*, 98 (2):66–75, 2002.

Harold, M. P., V. T. Zaspalis, K. Keizer, and A. J. Burggraaf. Intermediate product yield enhancement with analytical model for the case of isothermal and differential operation. *Chem. Eng. Sci.*, 48(15):2705–2725, 1993.

Harold, M. P. and C. Lee. Intermediate product yield enhancement with a catalytic inorganic membrane II. Nonisothermal and integral operation in a back-mixed reactor. *Chem. Eng. Sci.*, 52(12):1923–1939, 1997.

Haryanto, A., S. Fernando, N. Murali, and S. Adhikari. Current status of hydrogen production techniques by steam reforming of ethanol: a review. *Energy & Fuels*, 19(5): 2098–2106, 2005.

Hinchliffe, A. and K. Porter. A comparison of membrane separation and distillation. *Chem. Eng. Res. Des.*, 78(2), 2000.

Hoff, K. and J. Poplsteinova. Modeling of membrane reactor. In Seidel-Morgenstern, A., editor, Membr. React. Distrib. Reactants to Improv. Sel. Yield, pages 29–62. Wiley-VCH Verlag GmbH & Co. KGaA, Weinheim, 2002.

Holladay, J. D. D., J. Hu, D. L. L. King, and Y. Wang. An overview of hydrogen production technologies. *Catal. Today*, 139(4):244–260, 2009.

Hsieh, H., R. Bhave, and H. Fleming. Microporous alumina membranes. *J. Memb. Sci.*, 39(3):221–241, 1988.

Hsu, C. S. and P. R. Robinson, editors. Petroleum processing practical advances in petroleum processing, volume 1. Springer New York, 2006.

Ismail, A. and L. David. A review on the latest development of carbon membranes for gas separation. *J. Memb. Sci.*, 193(1):1–18, 2001.

Itoh, N. Simulation of bifunctional palladium membrane reactor. *J. Chem. Eng. Japan*, 23 (1):81–87, 1990.

Itoh, N., Y. Shindo, K. Haraya, and T. Hakuta. A membrane reactor using microporous glass for shifting equilibrium of cyclohexane dehydrogenation. *J. Chem. Eng. Japan*, 21(4):399–404, 1988.

Itoh, N., W. Tian-Hua, and K. Haraya. Two- and three-dimensional analysis of diffusion through a dense membrane supported on a porous material. *Journal of Membrane Science*, 99(2):175 – 183, 1995.

Jackson, R. Transport in porous catalysts. Elsevier Scientific Pub. Co., New York, 1977.

Kim, D., K. Barnett, and B. A. Wilhite. Experimental demonstration of enhanced hydrogen permeation in palladium via a composite catalytic permselective membrane. *AIChE J.*, 59(5):1627–1634, 2012.

Kirubakaran, A., S. Jain, and R. Nema. A review on fuel cell technologies and power electronic interface. *Renew. Sustain. Energy Rev.*, 13(9):2430–2440, 2009.

Kluiters, S. C. A. Status review on membrane systems for hydrogen separation. *Intermed. Rep. EU Proj. MIGREYD NNE5-2001*, (December), 2004.

Koros, W. J. and R. Mahajan. Pushing the limits on possibilities for large scale gas separation: which strategies? *J. Memb. Sci.*, 175(2):181–196, 2000.

Koros, W. J. J. and G. K. K. Fleming. Membrane-based gas separation. *J. Memb. Sci.*, 83 (1):1–80, 1993.

Krishna, R. and J. A. Wesselingh. The Maxwell-Stefan approach to mass transfer. *Chem. Eng. Sci.*, 52(6):861–911, 1997.

Lakeman, J. and D. Browning. Global status of hydrogen research. Harwell Laboratory, Energy Technology Support Unit, Fuel Cells Programme, 2001.

Lan, R., J. T. Irvine, and S. Tao. Ammonia and related chemicals as potential indirect hydrogen storage materials. *Int. J. Hydrogen Energy*, 37(2):1482–1494, 2012.

Larmine, J. and A. Dicks. Fuel cell systems Explained. John Wiley and Sons Ltd, New Jersy, 2000.

Li, A., J. R. Grace, and C. J. Lim. Preparation of thin Pd-based composite membrane on planar metallic substrate. *J. Memb. Sci.*, 298(1–2):175–181, 2007.

Liao, Z., J. Wang, Y. Yang, and G. Rong. Integrating purifiers in refinery hydrogen networks: a retrofit case study. *J. Clean. Prod.*, 18(3):233–241, 2010.

Lin, Y. S., I. Kumakiri, B. N. Nair, and H. Alsyouri. Microporous inorganic membranes. *Sep. Purif. Rev.*, 31(2):229–379, 2002.

Lin, Y. and S. Tanaka. Ethanol fermentation from biomass resources: current state and prospects. *Appl. Microbiol. Biotechnol.*, 69(6):627–642, 2006.

Lin, Y. Microporous and dense inorganic membranes: current status and prospective. *Sep. Purif. Technol.*, 25(1-3):39–55, 2001.

Liu, F. and N. Zhang. Strategy of purifier selection and integration in hydrogen networks. *Chem. Eng. Res. Des.*, 82(10):1315–1330, 2004.

Lloyd, L. Handbook of industrial catalysts. Fundamental and Applied Catalysis. Springer US, Boston, MA, 2011.

Lloyd, L. Ammonia and methanol synthesis. In Handb. Ind. Catal., Fundamental and Applied Catalysis, chapter 10. Springer US, Boston, MA, 2011.

Long, R., K. Picioccio, and A. Zagoria. Optimizing hydrogen production and use. *digital-refining.com*, pages 1–11, 2011.

Lu, G. Q., J. C. Diniz da Costa, M. Duke, S. Giessler, R. Socolow, R. H. Williams, and T. Kreutz. Inorganic membranes for hydrogen production and purification: A critical review and perspective. *J. Colloid Interface Sci.*, 314(2):589–603, 2007.

Mapiour, M., V. Sundaramurthy, a. K. Dalai, and J. Adjaye. Effect of hydrogen purity on hydroprocessing of heavy gas oil derived from oil-sands bitumen. *Energy & Fuels*, 23 (4):2129–2135, 2009.

Marcano, J. G. S. and T. T. Tsotsis. Catalytic Membranes and Membrane Reactors. Wiley-VCH Verlag GmbH, 2002.

Mas, V., M. L. Bergamini, G. Baronetti, N. Amadeo, and M. Laborde. A kinetic Study of ethanol steam reforming using a Nickel based catalyst. *Top. Catal.*, 51(1–4):39–48, 2008.

Mas, V., M. L. Dieuzeide, M. Jobbágy, G. Baronetti, N. Amadeo, and M. Laborde. Ni(II)-Al(III) layered double hydroxide as catalyst precursor for ethanol steam reforming: Activation treatments and kinetic studies. *Catal. Today*, 133-135:319–323, 2008.

Mason, E. and A. Malinauskas. Gas transport in porous media: the dusty-gas model, volume v. 17 of Chem. Eng. Monogr. Elsevier, 1983.

Maxwell, J. C. On the dynamical theory of gases. *Proc. R. Soc. London*, 15:167–171, 1866.

Maymo, J. A. and J. M. Smith. Catalytic oxidation of hydrogen – intrapellet heat and mass transfer. *AIChE J.*, 12(5):845–854, 1966.

Mazloomi, K. and C. Gomes. Hydrogen as an energy carrier: Prospects and challenges. *Renew. Sustain. Energy Rev.*, 16(5):3024–3033, 2012.

McLean, G. and T. Niet. An assessment of alkaline fuel cell technology. *Int. J. Hydrogen Energy*, 27:507–526, 2002.

Miller, G. Q. and J. Stöcker. Selection of a hydrogen separation process, pages 1–27. 1989.

Minh, N. Solid oxide fuel cell technology features and applications. *Solid State Ionics*, 174(1-4):271–277, 2004.

Mizsey, P., E. Newson, T.-b. Truong, and P. Hottinger. The kinetics of methanol decomposition: a part of autothermal partial oxidation to produce hydrogen for fuel cells. *Appl. Catal. A Gen.*, 213(2):233–237, 2001.

Mohanty, S., D. Kunzru, and D. Saraf. Hydrocracking: a review. *Fuel*, 69(12):1467 – 1473, 1990.

Moreno, A. M. Thermally integrated ceramic microreactors for hydrogen production. PhD thesis, University of Connecticut, Storrs, 2010.

Nagamoto, H. Fuel cells : Electrochemical reactions. *Encycl. Mater. Sci. Technol.*, pages 3359–3367, 2001.

Neurock, M., S. M. Stark, and M. T. Klein. Molecular simulation of kinetic interactions in complex mixtures. In Becker, E. and C. J.Pereira, editors, Comput. Des. Catal. Marcel Dekker, Inc., 1993.

Ni, M., D. Y. C. Leung, and M. K. H. Leung. A review on reforming bio-ethanol for hydrogen production. *Int. J. Hydrogen Energy*, 32(15):3238–3247, 2007.

Ockwig, N. W. and T. M. Nenoff. Membranes for hydrogen separation. *Chem. Rev.*, 107 (10):4078–110, 2007.

Oetjen, H. F. and V. M. Schmidt. Performance data of a proton exchange membrane fuel cell using H2/CO as fuel gas. *J. Electrochem. Soc.*, 143(12):3838–3842, 1996.

Paglieri, S. N. and J. D. Way. Innovations in palladium membrane research. *Sep. Purif. Rev.*, 31(1):1–169, 2002.

Petrovic, L. J. and G. Thodos. Mass transfer in the flow of gases through packed beds. *I EC Fundam.*, 7(2):274–280, 1953.

Rajalakshmi, N., T. Jayanth, and K. Dhathathreyan. Effect of carbon dioxide and ammonia on polymer electrolyte membrane fuel cell stack performance. *Fuel Cells*, 3(4):177–180, 2003.

Ramachandran, R. An overview of industrial uses of hydrogen. *Int. J. Hydrogen Energy*, 23(7):593–598, 1998.

Roh, H. S., M. S. Park, I. S. Chang, Y. K. Park, and S. E. Park'r. Dehydrogenation of propane over Pd-composite membrane. *J. Ind. Eng. Chem.*, 5(3):198–203, 1999.

Romero, E. L. and B. A. Wilhite. Composite catalytic-permselective membranes: Modeling analysis for H_2 purification assisted by water–gas-shift reaction. *Chem. Eng. J.*, 207–208(0):552–563, 2012.

Rothenberger, K., A. Cugini, B. Howard, R. Killmeyer, M. Ciocco, B. Morreale, R. Enick, F. Bustamante, I. Mardilovich, and Y. Ma. High pressure hydrogen permeance of porous stainless steel coated with a thin palladium film via electroless plating. *J. Memb. Sci.*, 244(1–2):55–68, 2004.

Sánchez, O. J. and C. a. Cardona. Trends in biotechnological production of fuel ethanol from different feedstocks. *Bioresour. Technol.*, 99(13):5270–5295, 2008.

Saracco, G. and J. Veldsink. Catalytic combustion of propane in a membrane reactor with separate feed of reactants—I. Operation in absence of trans-membrane pressure gradients. *Chem. Eng. Sci.*, 50(12):2005–2015, 1995.

Saracco, G. and J. W. Veldsink. Catalytic combustion of propane in a membrane reactor with separate feed of reactants—II. Operation in presence of trans-membrane pressure gradients. *Chem. Eng. Sci.*, 50(12):2833–2841, 1995.

Scherzer, J. and A. Gruia. Hydrocracking science and Technology. Chemical Industries. Taylor & Francis, 1996.

Shao, L., B. T. Low, T.-S. Chung, and A. R. Greenberg. Polymeric membranes for the hydrogen economy: Contemporary approaches and prospects for the future. *J. Memb. Sci.*, 327(1–2):18–31, 2009.

Sherif, S., F. Barbir, and T. Veziroglu. Wind energy and the hydrogen economy-review of the technology. *Sol. Energy*, 78(5):647–660, 2005.

Shoko, E., B. McLellan, Dicksa.L. , and J. D. Costada . Hydrogen from coal: Production and utilisation technologies. *Int. J. Coal Geol.*, 65(3–4):213–222, 2006.

Sircar, S. and T. C. Golden. Purification of hydrogen by pressure swing adsorption. *Sep. Sci. Technol.*, (5):37–41, 2000.

Sloot, H. Development of a non-permselective membrane reactor for catalytic gas phase reactions. PhD thesis, University of Twente, 1991.

Sloot, H., G. Versteeg, and W. P. M. Van Swaaij. A non-permselective membrane reactor for chemical processes normally requiring strict stoichiometric feed rates of reactants. *Chem. Eng. Sci.*, 45(8):2415–2421, 1990.

Smitha, B., S. Sridhar, and A. Khan. Solid polymer electrolyte membranes for fuel cell applications—a review. *J. Memb. Sci.*, 259(1–2):10–26, 2005.

Speight, J. G. The chemistry and technology of petroleum. CRC Press, 2010.

Stefan, J. Über das Gleichgewicht und die Bewegung, insbesondere die Diffusion von Gasgemengen. *Sitzber. Akad. Wiss. Wien*, 1871.

Sun, Y. M. and S. J. Khang. Catalytic membrane for simultaneous chemical reaction and separation applied to a dehydrogenation reaction. *Ind. Eng. Chem. Res.*, 27(7):1136–1142, 1988.

Sun, Y. M. and S. J. Khang. A catalytic membrane reactor: its performance in comparison with other types of reactors. *Industrial & engineering chemistry research*, 29(2):232–238, 1990.

Taylor, R. and R. Krishna. Multicomponent mass transfer. John Wiley & Sons, Inc., New York, 1993.

Thomas, J. and W. Thomas. Principles and practice of heterogeneous catalysis. Wiley, Weinheim VCH, 2008.

Topsoe, H., B. S. Clausen, and F. E. Massoth. Hydrotreating catalysis. In Anderson, J. R. and M. Boudard, editors, Catal. Technol., volume 36, page 344. Springer Berlin Heidelberg, 1996.

Tsuru, T., T. Tsuge, S. Kubota, K. Yoshida, T. Yoshioka, and M. Asaeda. Catalytic Membrane Reaction for Methane Steam Reforming Using Porous Silica Membranes. *Sep. Sci. Technol.*, 36(16):3721–3736, 2001.

Turner, J., G. Sverdrup, M. K. Mann, P.-C. Maness, B. Kroposki, M. Ghirardi, R. J. Evans, and D. Blake. Renewable hydrogen production. *Int. J. Energy Res.*, 32(5):379–407, 2008.

Turner, J. A. Sustainable hydrogen production. *Science*, 305(5686):972–4, 2004.

Uhlhorn, R., M. Huis In't Veld, K. Keizer, and A. Burggraaf. High permselectivities of microporous silica-modifiedγ-alumina membranes. *Journal of materials science letters*, 8(10):1135–1138, 1989.

Veldsink, J. W., R. M. J. Dammevan , G. F. Versteeg, and W. P. M. Swaaijvan . A catalytically active membrane reactor for fast, exothermic, heterogeneously catalysed reactions. *Chem. Eng. Sci.*, 47(9–11):2939–2944, 1992.

Veldsink, J. W. and R. M. J. V. Damme. The use of the dusty-gas model for the description of mass transport with chemical reaction in porous media. *Chem. Eng. J.*, 57(2):115–125, 1995.

Verónica, M., B. Graciela, A. Norma, and L. Miguel. Ethanol steam reforming using Ni(II)-Al(III) layered double hydroxide as catalyst precursor. *Chem. Eng. J.*, 138(1-3): 602–607, 2008.

Wade, R., J. Vislocky, T. Maesen, and D. Torchia. Hydrocracking catalyst and processing developments. *Petroleum Technology Quarterly*, (3):81, 2009.

Wang, Y., K. S. Chen, J. Mishler, S. C. Cho, and X. C. Adroher. A review of polymer

electrolyte membrane fuel cells: Technology, applications, and needs on fundamental research. *Appl. Energy*, 88(4):981–1007, 2011.

Ward, J. W. Hydrocracking processes and catalysts. *Fuel Process. Technol.*, 35(1–2): 55–85, 1993.

Wei, L., J. Yu, and Y. Huang. Silver coating on porous stainless steel substrate and preparation of H_2-permeable palladium membranes. *Int. J. Hydrogen Energy*, 38(25):10833–10838, 2013.

Wei, Q., F. Wang, Z.-R. Nie, C.-L. Song, Y.-L. Wang, and Q.-Y. Li. Highly hydrothermally stable microporous silica membranes for hydrogen separation. *J. Phys. Chem. B*, 112 (31):9354–9, 2008.

Weitkamp, J. Catalytic hydrocracking-mechanisms and versatility of the process. *ChemCatChem*, 4(3):292–306, 2012.

Wilhite, B. A. Composite Catalytic-Permselective Membranes: A Strategy for Enhancing Selectivity and Permeation Rates via Reaction and Diffusion. *Ind. Eng. Chem. Res.*, 50 (17):10185–10193, 2011.

Wilhite, B. A., M. A. Schmidt, and K. F. Jensen. Palladium-based micromembranes for hydrogen separation: device performance and chemical stability. *Ind. Eng. Chem. Res.*, 43(22):7083–7091, 2004.

Wilhite, B. A., S. E. Weiss, J. Y. Ying, M. A. Schmidt, and K. F. Jensen. High-purity hydrogen generation in a microfabricated 23 wt% ag–pd membrane device integrated with 8:1 $lani_{0.95}co_{0.05}o_3/al_2o_3$ catalyst. *Advanced Materials*, 18(13):1701–1704, 2006.

Wilke, C. R. A viscosity equation for gas mixtures. *J. Chem. Phys.*, 18(4):517–519, 1950.

Winter, C.-J. Hydrogen energy — Abundant, efficient, clean: A debate over the energy-system-of-change. *Int. J. Hydrogen Energy*, 34(14):S1–S52, 2009.

Zaman, J. and A. Chakma. Inorganic membrane reactors. *J. Memb. Sci.*, 92(1):1–28, 1994.

Zaspalis, V. and A. Burggraaf. Inorganic membrane reactors to enhance the productivity of chemical processes. In Bhave, R. R., editor, Inorg. Membr. Synth. Charact. Appl., chapter 7. Van Nostrand Reinhold, 1992.

Zaspalis, V., W. Praagvan , K. Keizer, J. Ommenvan , J. Ross, and A. Burggraaf. Reactor studies using alumina separation membranes for the dehydrogenation of methanol and n-butane. *Appl. Catal.*, 72(2):223–234, 1991.

Zhu, X.-j. and B. Huang. Molten Carbonate Fuel Cells. In Liu, R.-S., L. Zhang, X. Sun, H. Liu, and J. Zhang, editors, Electrochem. Technol. Energy Storage Convers., chapter 16. Wiley-VCH Verlag GmbH & Co. KGaA., first edition, 2012.

APPENDIX A

Introduction

This chapter presents the comparison between the simulation results obtained in Maxwell-Stefan model and Fick's model for water-gas-shift catalytic membrane reactor (Chapter 2).

Maxwell-Stefan multicomponent diffusion model

The following sections describes the Maxwell-Stefan diffusion model equations to describe the multicomponent diffusion in catalyst volume, combined with Darcy's law to describe pressure difference within the catalyst membrane (no external pressure difference), and combined with plug-flow equations to describe mass transport in feed and sweep volume.

Catalyst Volume

Diffusive transport and catalytic reaction within the membrane is described using an isothermal, steady-state Maxwell-Stefan multicomponent diffusion equation for gases, casting mass flux in terms of mole and weight fractions following methods outlined by Curtiss and Bird in [Curtiss and Bird, 1999],

$$\nabla \cdot \left(-\rho w_i \sum_k D_{ik} \left(\nabla x_k + (x_k - w_k) \frac{\nabla p}{p} \right) - D^T \frac{\nabla T}{T} \right) = R - \rho u \cdot \nabla w_i$$

where

$$\rho = \frac{P \sum_{i=1}^{k} x_i M_i}{RT}$$

The above equation employs a matrix of effective Maxwell-Stefan binary diffusivities, each estimated from a combination of Knudsen and molecular diffusion contributions via

the Wilke-Bosanquet equation [Bird *et al.*, 2007],

$$\frac{1}{D_{ik}^{eff}} = \frac{1}{\frac{\varepsilon}{\tau}D_{ik}} + \frac{1}{\frac{\varepsilon}{\tau}D_{ik}^{eff}}$$

where Knudsen diffusivities are obtained from kinetic theory of gasses,

$$D_{i,K} = \frac{1}{3}d_p\left(\frac{8RT}{\pi M_i}\right)^{1/2}$$

$$D_{ij} = \frac{1\times10^{-7}T^{1.75}\left(1/M_i + 1/M_j\right)}{P\left(\upsilon_i^{1/3} + \upsilon_j^{1/3}\right)}$$

and binary diffusion coefficients are estimated using the method of Fuller, Schettler and Giddings method Fuller1966, where empirical values for diffusion volume (υ) are employed for CO (18.9), CO_2 (26.9), H_2 (7.07), H_2O (12.7) and N_2 (17.9) [Geankoplis, 1993]. A porosity of 45% is assumed for the present study, with a corresponding tortuosity factor of 2 based upon correlations by Neurock et al. in [Neurock *et al.*, 1993].

Reaction system

Water-gas-shift reaction is modeled using the power-law rate expression described by Mizsey et al. [Mizsey *et al.*, 2001] for a CuO/Al_2O_3 (5% Copper on Alumina) catalyst, assuming a catalyst density of $1000\,\mathrm{kg\,m^{-3}}$.

$$r_{CO} = \delta k_f\left(p_{CO}^{cat}p_{H_2O}^{cat} - \frac{p_{CO_2}^{cat}p_{H_2}^{cat}}{K_{eq}}\right)$$

where δ represents an arbitrary catalyst dilution factor and the rate constant and equilibrium constants are defined as

$$k_f = 2.25\times10^{-3}exp\left(\frac{-50,000}{RT}\right)$$

$$K_{eq} = 9.543 \times 10^{-3} exp\left(\frac{39,876}{RT}\right)$$

Pressure gradient

Convective transport of gas through the catalyst model volume is described by Darcy's Law for gas permeation through porous media,

$$\nabla\left(\rho\left(\frac{-\kappa}{\mu}\nabla P\right)\right) = 0$$

where the permeability of the catalyst membrane is determined using the method of Mason and coworkers,

$$\kappa = \frac{\varepsilon d_p^2}{8\tau}$$

and the dynamic viscosity of the gas mixture is evaluated using the semi-empirical formula developed by C.R.Wilke [Wilke, 1950],

$$\mu = \sum \frac{x_i \mu_i}{x_i + \sum x_j \varphi_{ij}}$$

where

$$\varphi = \frac{\left[1 + \left[\frac{\mu_i}{\mu_j}\right]^{\frac{1}{2}} \left[\frac{M_j}{M_i}\right]^{\frac{1}{4}}\right]^2}{\sqrt{8}\left[1 + \frac{M_i}{M_j}\right]^{\frac{1}{2}}}$$

and

$$\mu_i = 2.67 \times 10^{-5} \frac{\sqrt{M_i T}}{\sigma^2 \Omega_\mu}$$

where Lennard-Jones parameters are taken from [Bird *et al.*, 2007].

Solution of Darcy's Law in tandem with the conservation of mass law allows descrip-

tion of the evolution of local pressure gradients within the catalytic membrane owing to changes in gas density upon reaction, and pressure-driven velocities arising either from internally-developed pressure gradients or externally-applied pressure gradients. The values for the local gas total pressure (P) and two-dimensional gas velocity ($\tilde{u}$) are then employed by the Maxwell-Stefan model to account for convective transport of mass. Retentate and permeate fluid volumes are modeled assuming perfect plug-flow behavior, i.e., no backmixing or fluid-phase dispersion. Both volumes are assumed to be isobaric and isothermal, maintained at a uniform total pressure of 1 bar and 773 K, unless otherwise noted.

Retentate and Permeate volumes

One-dimensional plug-flow models describing individual species molar flow along the axial length of the membrane are employed, assuming mass appearance in the bulk fluid volume occurs via gas-solid mass transfer, i.e.,

$$\frac{1}{A_C^F}\frac{dF_i^F}{dz} = -k_{gs}\tilde{a}\left(p_i^F - p_i^{cat}\right)$$

and

$$\frac{1}{A_C^S}\frac{dF_i^S}{dz} = -k_{gs}\tilde{a}\left(p_i^S - p_i^{cat}\right)$$

The fluid and catalyst volume models are linked through boundary conditions equating individual species mass fluxes normal to the the fluid-catalyst boundary, and equating overall mass fluxes normal to the fluid-catalyst boundary i.e.,

$$\left(-\rho w_i \sum_k D_{ik}\left(\nabla x_k + (x_k - w_k)\frac{\nabla p}{p}\right) - D^T\frac{\nabla T}{T}\right)\cdot\tilde{n} = k_{gs}\left(p_i^{F,S} - p_i^{cat}\right)M_i$$

and equating overall mass fluxes normal to the fluid-catalyst boundary, i.e.,

$$\tilde{u} \cdot \tilde{n} = \frac{\sum k_{gs} \left(p_i^{F,S} - p_i^{cat} \right) M_i}{\rho}$$

Numerical solution

The resulting two-dimensional model was implemented using the commercial COMSOL Multiphysics V3.5 environment equipped with the Chemical Engineering Module, employing Maxwell-Stefan and Darcy's Law physics modules in 2-D radial symmetry mode to describe the catalyst volume and separate coefficient form PDE modules to describe the retentate and permeate volumes. Finite element meshes employed in the present work consisted of approximately 8,000 triangular elements, resulting in $\sim 10^5$ degrees of freedom. Solutions were obtained using the prepackaged stationary Direct UMFPACK solver (v4.2) written by Timothy A. Davis, which employs an unsymmetric multifrontral method for solving sparse, unsymmetric linear systems [Davis, 2004, 1995]. All simulations were carried out on a Dell Precision Workstation T7500 with Intel® Xeon®CPU X5670 @2.93GHz equipped with 24GB of RAM, with a typical solution time of 600 seconds.

Results and discussion

The isothermal Fick's diffusion model presented in Chapter 2 and Maxwell-stefan multicomponent diffusion model described above is simulated for a range of Damkohler number (varying the feed flow rates). The details of simulation strategy is same as described in Chapter 2 and Chapter 4. Thus, predicted results are compared with each other to justify the use of Fick's model for describing the catalyst volume with pore diameter of 10 nm described in Chapter 2 and Chapter 4.

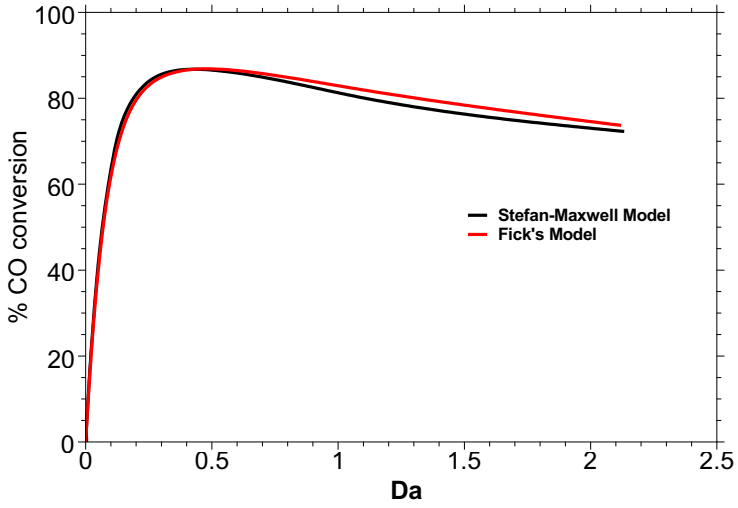
% CO conversion
Da
Stefan-Maxwell Model
Fick's Model
0
20
40
60
80
100
0
0.5
1
1.5
2
2.5

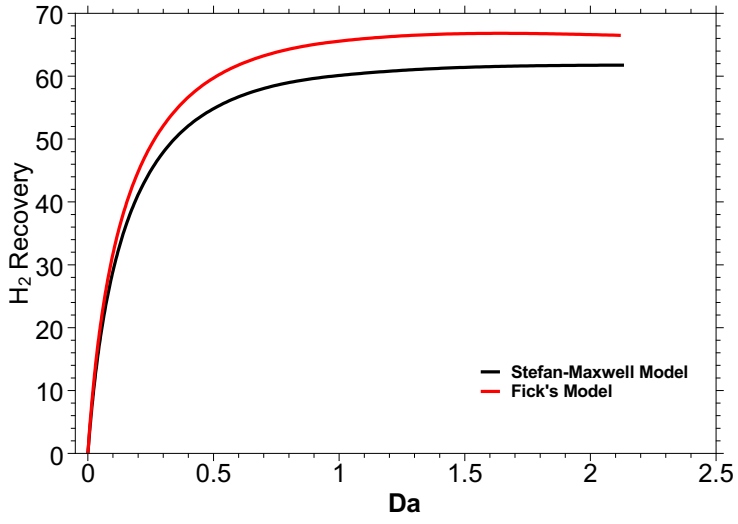
H2 Recovery
Da
Stefan-Maxwell Model
Fick's Model
0
10
20
30
40
50
60
70
0
0.5
1
1.5
2
2.5

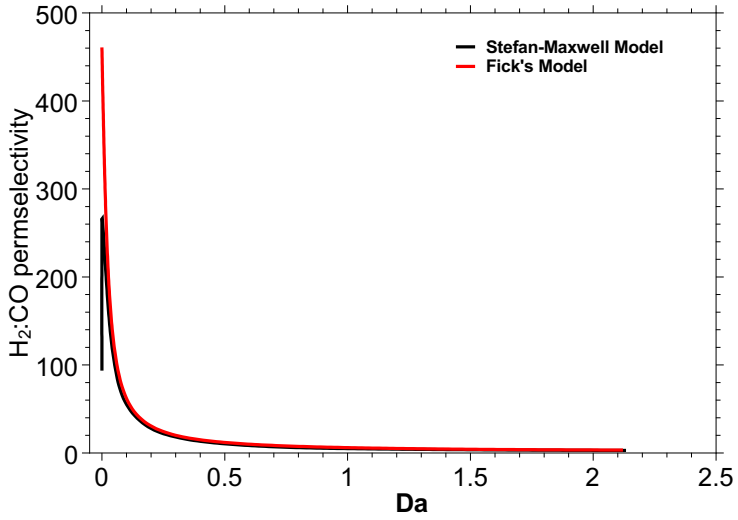

The simulation results from two models employing a catalyst membrane with pore diameter of 10 nm, are compared in the above Figures. Isothermal simulation results employing Stefan-Maxwell diffusion model and Fick's model with a catalyst pore diameter of 10 nm predicts identical results. The model presented above can be employed to simulate varying the catalyst membrane pore diameter, as discussed in Chapter 1, the quantitative agreement between the two models may be different depending on the mechanism of gas transport.

APPENDIX B

Introduction

This chapter presents a COMSOL Multiphysics model for obtaining numerical solution of water-gas-shift catalytic membrane reactor model developed in Chapter 2. This represents a typical model used to solve a system of mass and energy balance equations using predefined application modes of the Chemical Engineering Module.

The COMSOL Multiphysics model is categorized into different subsections to setup the model and define various parameters (constants and expressions) requisite for solving the final model.

Constants

Name	Expression	Description
Pf	1*101325 [Pa]	membrane pressure, Pa
To	500+273.15 [K]	Temperature, K
MWCO	28e-3 [kg/mol]	molecular weight of CO, kg/mol
MWCO2	44e-3 [kg/mol]	molecular weight of CO2, kg/mol
MWH2	2e-3 [kg/mol]	molecular weight of H2, kg/mol
MWH2O	18e-3 [kg/mol]	molecular weight of H2O, kg/mol
MWAr	40e-3 [kg/mol]	molecular weight of Ar, kg/mol
D	1000 [m]	radial mass dispersion coefficient, units m.
NTFO	3.4e-4 [mol/s]	total molar flowrate in feed volume, mol/sec
FTFO	NTFO/width_f	feed total inlet 2-D molar superficial velocity, mol/m/sec
yCOfo	0.09	feed mole fraction of CO

yCO2fo	0.03	feed mole fraction of CO2
yH2fo	0.28	feed mole fraction of H2
yH2Ofo	0.15	feed mole fraction of H2O
yArfo	0	feed mole fraction of Ar
yN2fo	1-yCOfo-yCO2fo -yH2fo-yH2Ofo-yArfo	feed mole fraction of N2
FCOfo	FTFO*yCOfo	feed inlet CO molar 2-D superficial velocity (mol/s/m)
FCO2fo	FTFO*yCO2fo	feed inlet CO2 molar 2-D superficial velocity, mol/m/s
FH2fo	FTFO*yH2fo	feed inlet H2 molar 2-D superficial velocity, mol/m/s
FH2Ofo	FTFO*yH2Ofo	feed inlet H2O molar 2-D superficial velocity, mol/m/s
FArfo	FTFO*yArfo	feed inlet Ar molar 2-D superficial velocity, mol/m/s
FN2fo	FTFO*yN2fo	feed inlet N2 molar 2-D superficial velocity, mol/m/s
MCOfo	FCOfo*MWCO	feed inlet CO mass 2-D superficial velocity, kg/m/s
MCO2fo	FCO2fo*MWCO2	feed inlet CO2 mass 2-D superficial velocity, kg/m/s
MH2fo	FH2fo*MWH2	feed inlet H2 mass 2-D superficial velocity, kg/m/s
MH2Ofo	FH2Ofo*MWH2O	feed inlet H2O mass 2-D superficial velocity, kg/m/s
MArfo	FArfo*MWAr	feed inlet Ar mass 2-D superficial velocity, kg/m/s
MN2fo	FN2fo*MWN2	feed inlet N2 mass 2-D superficial velocity, kg/m/s
MTFO	MCOfo+MCO2fo+MH2fo+ MH2Ofo+MArfo+MN2fo	total mass 2-D superficial velocity, kg/m/sec average
MWavefo	yCOfo*MWCO+yCO2fo *MWCO2+yH2fo*MWH2 +yH2Ofo*MWH2O+yArfo *MWAr+yN2fo*MWN2	feed molecular weight, from composition
MWavefo_2	MTFO/FTFO	CHECKER
NTSO	0.6600000*NTFO	total molar flowrate into sweep volume, mol/sec

FTSO	NTSO/width_s	sweep total inlet molar superficial velocity, mol/m/sec
yCOso	0	sweep inlet mole fraction of CO
yCO2so	0	sweep inlet mole fraction of CO2
yH2so	0	sweep inlet mole fraction of H2
yH2Oso	1	sweep inlet mole fraction of H2O
yArso	1e-12	sweep inlet mole fraction of Ar
yN2so	1-yCOso-yCO2so -yH2so-yH2Oso-yArso	sweep inlet mole fraction of N2
FCOso	FTSO*yCOso	sweep inlet CO molar superficial velocity, mol/m/s
FCO2so	FTSO*yCO2so	sweep inlet CO2 molar superficial velocity, mol/m/s
FH2so	FTSO*yH2so	sweep inlet H2 molar superficial velocity, mol/m/s
FH2Oso	FTSO*yH2Oso	sweep inlet H2O molar superficial velocity, mol/m/s
FArso	FTSO*yArso	sweep inlet Ar molar superficial velocity, mol/m/s
FN2so	FTSO*yN2so	sweep inlet N2 molar superficial velocity, mol/m/s
MCOso	FCOso*MWCO	sweep inlet CO mass superficial velocity, mol/m/s
MCO2so	FCO2so*MWCO2	sweep inlet CO2 mass superficial velocity, mol/m/s
MH2so	FH2so*MWH2	sweep inlet H2 mass superficial velocity, mol/m/s
MH2Oso	FH2Oso*MWH2O	sweep inlet H2O mass superficial velocity, mol/m/s
MArso	FArso*MWAr	sweep inlet Ar mass superficial velocity, mol/m/s
MN2so	FN2so*MWN2	sweep inlet N2 mass superficial velocity, mol/m/s

MTSO	MCOso+MCO2so +MH2so+MH2Oso +MArso+MN2so	sweep total inlet mass superficial velocity, kg/m/sec
MWaveso	yCOso*MWCO+yCO2so *MWCO2+yH2so*MWH2 +yH2Oso*MWH2O +yArso*MWAr +yN2so*MWN2	average sweep inlet molecular weight, from composition.
MWaveso_2	MTSO/FTSO	average sweep inlet molecular weight, from composition.
R	8.314 [m^3*Pa/mol/K]	ideal gas constant, m3*Pa/mol/K
haf	1 [mol/(m^2*s*Pa)]	feed side mass transfer coefficient, mol/m2/s/Pa
has	1 [mol/(m^2*s*Pa)]	sweep side mass transfer coefficient, mol/m2/s/Pa
SACAs	Acs*ams	geometry factor
SACAf	Acf*amf pi*2*1e-2*0.15 [m^2]	membrane surface area, feed-side (2*r*Pi*L)
mSAf	pi*(1e-2)^2 [m^2]	cross-sectional area of feed-side volume (r^2*Pi)
CAf	pi*2*(1e-2+1e-3)*0.15 [m^2]	membrane surface area, sweep-side (2*(r+tc)*Pi*L)
mSAs	((1e-2+1e-3+0.00387)^2 - (1e-2+1e-3)^2)*pi 4.75e-3 [m]	cross-sectional area of sweep-side volume
CAs	((1e-2+1e-3+0.00387)^2 - (1e-2+1e-3)^2)*pi	width of feed flow model volume, m
width_f	4.75e-3 [m]	width of sweep flow model volume, m
width_s	1.59e-3 [m]	width of sweep flow model volume, m
Acf	pi*(width_f)^2 pi*2*width_f/Acf	feed-side cross-sectional area for flow, m2
Acs	pi*((width_s+tcat+width_f)^2 -(width_f+tcat)^2)	sweep-side cross-sectional area for flow, m2
amf	pi*2*width_f/Acf	membrane-side surface area-to-volume ratio, 1/m
ams	pi*2*(width_f+tcat)/Acs	membrane-side surface area-to-volume ratio, 1/m

EA	50000 [J/mol]	activation energy of WGS reaction
k0	2.225e-3[mol/(m^3*s*Pa^2)]	forward rate coefficient for WGS
kgm2s_f	MTFO*width_f /(amf*Acf*(0.15e-2 [m]))	feed-side total mass flow per unit membrane area
kgm2s_s	MTSO*width_s/ (ams*Acs*(0.15e-2 [m]))	sweep-side total mass flow per unit membrane area
SCrat	(FH2Oso*width_s + FH2Ofo*width_f)/(FCOfo*width_f)	
kineticsscale	0.23	Catalyst activation factor
checker	Acf/Acs	
tcat	1.56e-3 [m]	width of catalyst layer
Ps	101325	Total pressure of sweep volume

Scalar expressions

Name	Expression	Description
rho	P_membrane/To/R*MWave	density of gas in catalyst volume, kg/m3
MWave	x_wCO_membrane*MWCO +x_wCO2_membrane*MWCO2 +x_wH2_membrane*MWH2+ x_wH2O_membrane*MWH2O +x_wAr_membrane*MWAr+ x_wN2_membrane*MWN2	average molecular weight of gas in catalyst
FTF	FCOf+FCO2f+FH2f +FH2Of+FArf+FN2f	total molar superficial velocity in feed
yCOf	FCOf/FTF	mole fraction of CO, feed volume
yCO2f	FCO2f/FTF	mole fraction of CO2, feed volume
yH2f	FH2f/FTF	mole fraction of H2, feed
yH2Of	FH2Of/FTF	mole fraction of H2O, feed
yArf	FArf/FTF	mole fraction of Ar, feed
pCOf	Pf*yCOf	feed side CO partial pressure, Pa
pCO2f	Pf*yCO2f	feed side CO2 partial pressure, Pa
pH2f	Pf*yH2f	feed side H2 partial pressure, Pa
pH2Of	Pf*yH2Of	feed side H2O partial pressure, Pa
pArf	Pf*yArf	feed side Ar partial pressure, Pa

pN2f	Pf*yN2f	feed side N2 partial pressure, Pa
pCO	cCO*R*To	partial pressure of CO in catalytst
pCO2	cCO2*R*To	partial pressure of CO2 in catalytst
pH2	cH2*R*To	partial pressure of H2 in catalytst
pH2O	cH2O*R*To	partial pressure of H2O in catalytst
pAr	cAr*R*To	partial pressure of Ar in catalytst
pN2	cN2*R*To	partial pressure of N2 in catalytst
FTS	FCOs+FCO2s+FH2s +FH2Os+FArs+FN2s	total molar superficial velocity, sweep side, mol/m2/sec
yCOs	FCOs/FTS	mole fraction of CO, sweep volume
yCO2s	FCO2s/FTS	mole fraction of CO2, sweep side
yH2s	FH2s/FTS	mole fraction of H2, sweep volume
yH2Os	FH2Os/FTS	mole fraction of H2O, sweep volume
yArs	FArs/FTS	mole fraction of Ar, sweep volume
yN2s	FN2s/FTS	mole fraction of N2, sweep volume
pCOs	Ps*yCOs	sweep side CO partial pressure, Pa
pCO2s	Ps*yCO2s	sweep side CO2 partial pressure, Pa
pH2s	Ps*yH2s	sweep side H2 partial pressure, Pa
pH2Os	Ps*yH2Os	sweep side H2O partial pressure, Pa
pArs	Ps*yArs	sweep side Ar partial pressure, Pa
pN2s	Ps*yN2s	sweep side N2 partial pressure, Pa

Global expressions

Name	**Expression**	**Description**
m_co	3.4915e-5[Pa*s]	Viscosity of CO
m_co2	3.1786e-5[Pa*s]	Viscosity of CO2
m_h2	1.6599e-5[Pa*s]	Viscosity of H2
m_h2o	2.8575e-5[Pa*s]	Viscosity of H2O
m_n2	3.4077e-5[Pa*s]	Viscosity of N2
m_ar	4.5283e-5[Pa*s]	Viscosity of Ar
X_co_co	1 [1]	
X_co_co2	1.3056 [1]	
X_co_h2	0.2795 [1]	
X_co_h2o	0.87565 [1]	
X_co_n2	1.01226 [1]	
X_co_ar	1.041678 [1]	

X_co2_co2	1 [1]
X_co2_co	0.7564 [1]
X_co2_h2	0.19802 [1]
X_co2_h2o	0.6474 [1]
X_co2_n2	0.7649 [1]
X_co2_ar	0.8064 [1]
X_h2_co	1.8603 [1]
X_h2_co2	2.2751 [1]
X_h2_h2	1 [1]
X_h2_h2o	1.8055 [1]
X_h2_n2	1.88634 [1]
X_h2_ar	1.7942 [1]
X_h2o_co	1.1148 [1]
X_h2o_co2	1.4227 [1]
X_h2o_h2	0.3453 [1]
X_h2o_h2o	1 [1]
X_h2o_n2	1.1285 [1]
X_h2o_ar	1.13933 [1]
X_n2_co	0.98796 [1]
X_n2_co2	1.2886 [1]
X_n2_h2	0.2766 [1]
X_n2_h2o	0.86516 [1]
X_n2_n2	1 [1]
X_n2_ar	1.029396 [1]
X_ar_co	0.9457 [1]
X_ar_co2	1.2637 [1]
X_ar_h2	0.2447 [1]
X_ar_h2o	0.8125 [1]
X_ar_n2	0.9575 [1]
X_ar_ar	1 [1]
Xco_m	$x\_wCO\_membrane + x\_wCO2\_membrane$ $*X\_co\_co2 + x\_wH2\_membrane$ $*X\_co\_h2 + x\_wH2O\_membrane$ $*X\_co\_h2o + x\_wN2\_membrane$ $*X\_co\_n2 + x\_wAr\_membrane$ $*X\_co\_ar$

Xco2_m	$x\_wCO2\_membrane+$ $x\_wCO\_membrane$ $*X\_co2\_co+x\_wH2\_membrane$ $*X\_co2\_h2+x\_wH2O\_membrane$ $*X\_co2\_h2o+x\_wN2\_membrane$ $*X\_co2\_n2+x\_wAr\_membrane$ $*X\_co2\_ar$	
Xh2_m	$x\_wCO\_membrane*X\_h2\_co$ $+x\_wCO2\_membrane*X\_h2\_co2$ $+x\_wH2\_membrane*X\_h2\_h2$ $+x\_wH2O\_membrane*X\_h2\_h2o$ $+x\_wN2\_membrane*X\_h2\_n2$ $+x\_wAr\_membrane$ $*X\_h2\_ar$	
Xh2o_m	$x\_wCO\_membrane*X\_h2o\_co$ $+x\_wCO2\_membrane*X\_h2o\_co2$ $+x\_wH2\_membrane*X\_h2o\_h2$ $+x\_wH2O\_membrane*X\_h2o\_h2o$ $+x\_wN2\_membrane*X\_h2o\_n2$ $+x\_wAr\_membrane*X\_h2o\_ar$	
Xn2_m	$x\_wCO\_membrane*X\_n2\_co+$ $x\_wCO2\_membrane*X\_n2\_co2$ $+x\_wH2\_membrane*X\_n2\_h2$ $+x\_wH2O\_membrane*X\_n2\_h2o$ $+x\_wN2\_membrane*X\_n2\_n2$ $+x\_wAr\_membrane*X\_n2\_ar$	
Xar_m	$x\_wCO\_membrane*X\_ar\_co$ $+x\_wCO2\_membrane*X\_ar\_co2$ $+x\_wH2\_membrane*X\_ar\_h2$ $+x\_wH2O\_membrane$ $*X\_ar\_h2o+x\_wN2\_membrane$ $*X\_ar\_n2+x\_wAr\_membrane$ $*X\_ar\_ar$	
X_num	$x\_wCO\_membrane*m\_co+x\_wCO2\_membrane*m\_co2$ $+x\_wH2\_membrane$ $*m\_h2+x\_wH2O\_membrane$ $*m\_h2o+x\_wN2\_membrane$ $*m\_n2+x\_wAr\_membrane*m\_ar$	
mu_mix	$(X\_num)/(Xco\_m*$ $x\_wCO\_membrane$ $+Xco2\_m*x\_wCO2\_membrane$ $+Xh2\_m*x\_wH2\_membrane$ $+Xh2o\_m*x\_wH2O\_membrane$ $+Xn2\_m*x\_wN2\_membrane$ $+Xar\_m*x\_wAr\_membrane)$	Dynamic viscosity of gas mixture

Geometry modeling

- Space dimensions: 2D

- Independent variables: r, z, phi

Geometry

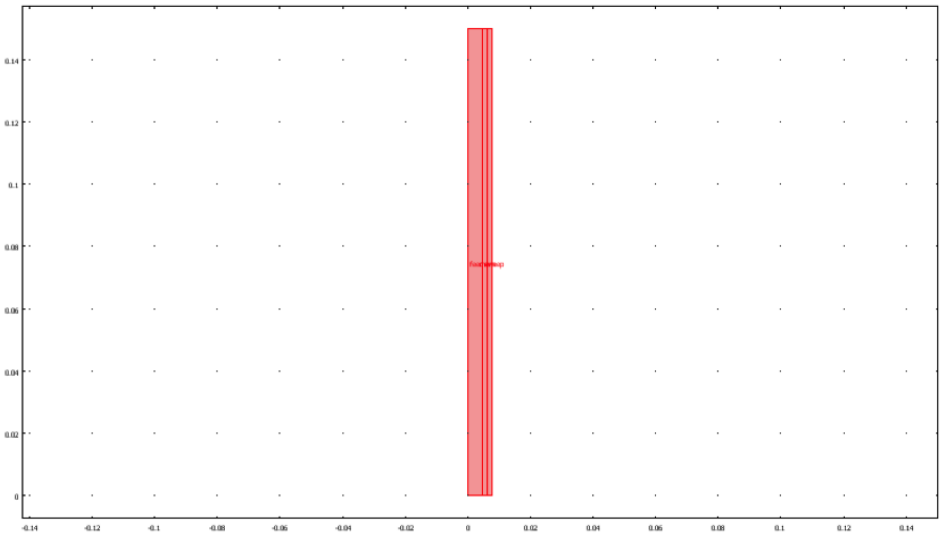

Point mode

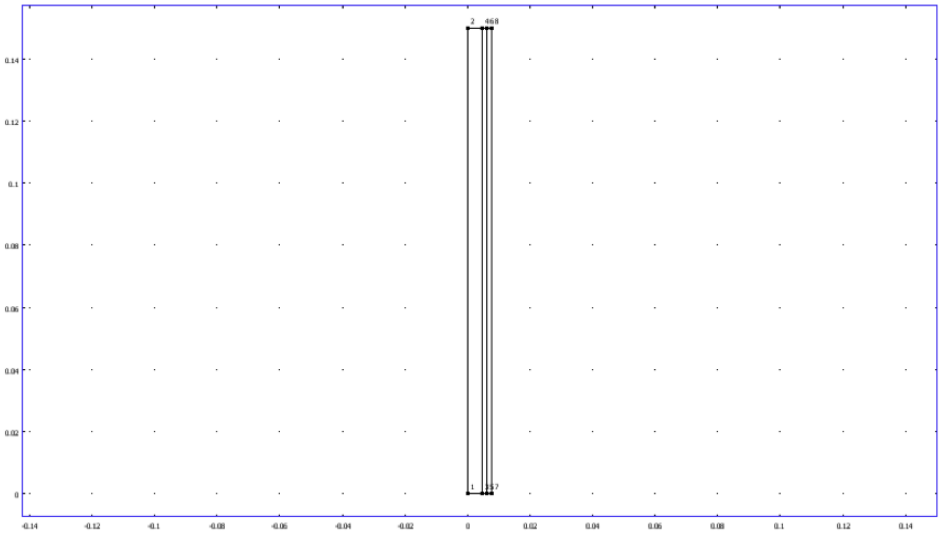
2
4 6 8
1
3 5 7
0.14
0.12
0.1
0.08
0.06
0.04
0.02
0
-0.14
-0.12
-0.1
-0.08
-0.06
-0.04
-0.02
0
0.02
0.04
0.06
0.08
0.1
0.12
0.14

Boundary mode

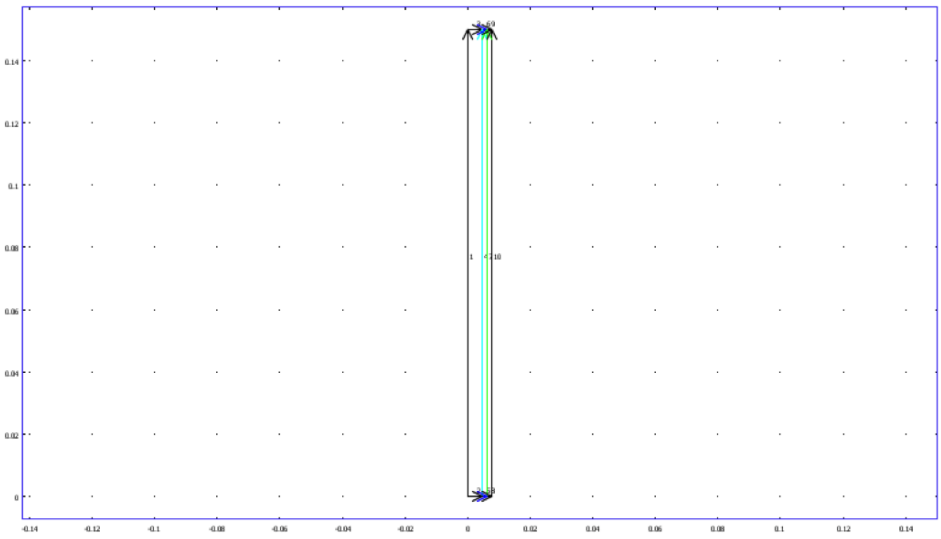

Subdomain mode

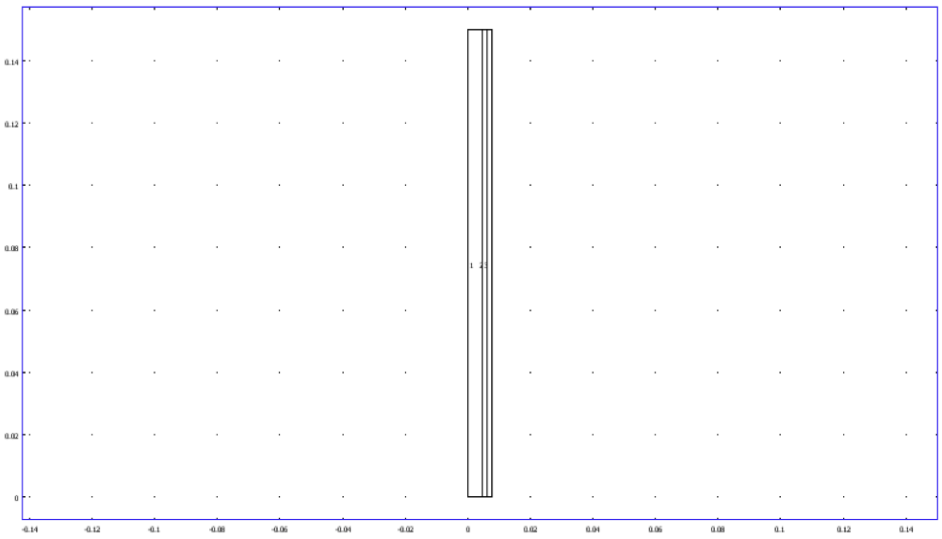

Mesh

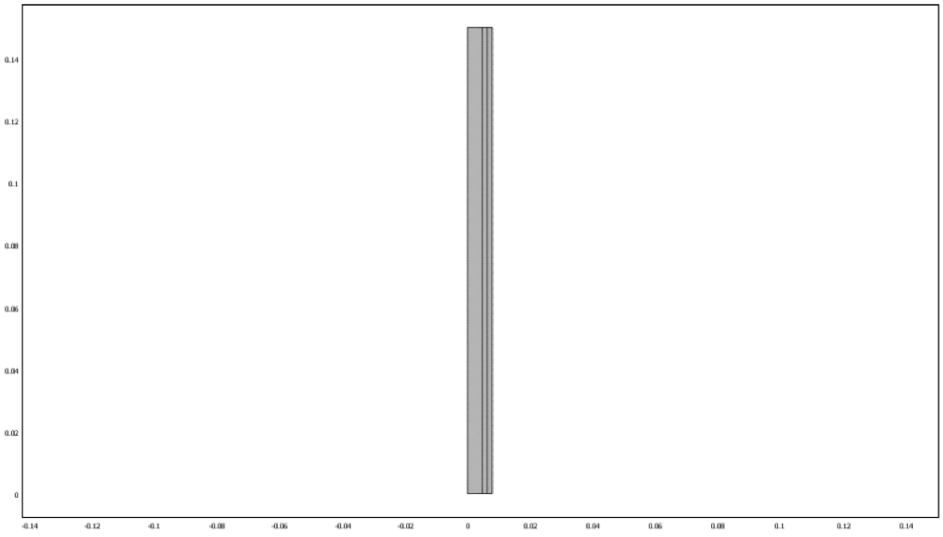

Mesh Statistics

Number of degrees of freedom	389874
Number of mesh points	15889
Number of elements	30976
Triangular	30976
Quadrilateral	0
Number of boundary elements	1912
Number of vertex elements	8
Minimum element quality	0.682
Element area ratio	0.049

Application mode: PDE, Coefficient Form (feed)

- Application mode type: PDE, Coefficient Form

- Application mode name: feed

Property	Value
Default element type	Lagrange - Quadratic
Wave extension	Off
Frame	Frame (ref)
Weak constraints	Off

Variables

- Dependent variables: FCOf, FCO2f, FH2f, FH2Of, FArf, FN2f, FCOf_t, FCO2f_t, FH2f_t, FH2Of_t, FArf_t, FN2f_t
- Shape functions: shlag(2,'FCOf'), shlag(2,'FCO2f'), shlag(2,'FH2f'), shlag(2,'FH2Of'), shlag(2,'FArf'), shlag(2,'FN2f')
- Interior boundaries not active

Boundary Settings

Boundary	**1,3**	**2**	**4**
Type	Neumann boundary condition	Neumann boundary condition	Neumann boundary condition
(g)	{0;0;0;0;0;0}	$\{FCOf - FCOfo$; $FCO2f - FCO2fo$; $FH2f - FH2fo$; $FH2Of - FH2Ofo$; $FArf - FArfo$; $FN2f - FN2fo\}$	$\{-haf*(pCOf - pCO)*SACAf$; $-haf*(pCO2f - pCO2)*SACAf$; $-haf*(pH2f - pH2)*SACAf$; $-haf*(pH2Of - pH2O)*SACAf$; $-haf*(pArf - pAr)*SACAf$; $-haf*(pN2f - pN2)*SACAf\}$

Subdomain Settings

Subdomain	1
Diffusion coefficient (c)	{{D;0},0,0,0,0,0;0,{D;0},0,0,0,0;0,0, {D;0},0,0,0;0,0,0,{D;0},0,0;0,0,0,0, {D;0},0;0,0,0,0,0,0,{D;0}}
Source term (f)	{0;0;0;0;0;0}
Convection coefficient (be)	{{0;1},{0;0},{0;0},{0;0},{0;0},{0;0}; {0;0},{0;1},{0;0},{0;0},{0;0},{0;0};{0;0}, {0;0},{0;1},{0;0},{0;0},{0;0};{0;0},{0;0}, {0;0},{0;1},{0;0},{0;0};{0;0},{0;0}, {0;0},{0;0},{0;1},{0;0};{0;0}, {0;0},{0;0},{0;0},{0;0},{0;1}}

Initial values

Subdomain initial value	1
FCOf	FCOfo
FCO2f	FCO2fo
FH2f	FH2fo
FH2Of	FH2Ofo
FArf	FArfo
FN2f	FN2fo

Application mode: PDE, Coefficient Form (sweep)

- Application mode type: PDE, Coefficient Form
- Application mode name: sweep

Property	Value
Default element type	Lagrange - Quadratic
Wave extension	Off
Frame	Frame (ref)
Weak constraints	Off

Variables

- Dependent variables: FCOs, FCO2s, FH2s, FH2Os, FArs, FN2s, FCOs_t, FCO2s_t, FH2s_t, FH2Os_t, FArs_t, FN2s_t
- Shape functions: shlag(2,'FCOs'), shlag(2,'FCO2s'), shlag(2,'FH2s'), shlag(2,'FH2Os'), shlag(2,'FArs'), shlag(2,'FN2s')
- Interior boundaries not active

Boundary Settings

Boundary	8, 10	9	7
Type	Neumann boundary condition	Neumann boundary condition	Neumann boundary condition
(g)	{0;0;0;0;0;0}	$-(FCOs-FCOso)$; $-(FCO2s-FCO2so)$; $-(FH2s-FH2so)$; $-(FH2Os-FH2Oso)$; $-(FArs-FArso)$; $-(FN2s-FN2so)\}$	$has*(pCO-pCOs)*SACAs$; $has*(pCO2-pCO2s)*SACAs$; $has*(pH2-pH2s)*SACAs$; $has*(pH2O-pH2Os)*SACAs$; $has*(pAr-pArs)*SACAs$; $has*(pN2-pN2s)*SACAs$

Subdomain Settings

Subdomain	3
Diffusion coefficient (c)	$\{D;0\},0,0,0,0,0;$ $0,\{D;0\},0,0,0,0;$ $0,0,\{D;0\},0,0,0;$ $0,0,0,\{D;0\},0,0;$ $0,0,0,0,\{D;0\},0;$ $0,0,0,0,0,\{D;0\}$
Source term (f)	{0;0;0;0;0;0}
Convection coefficient (be)	$\{0;-1\},\{0;0\},\{0;0\},\{0;0\},\{0;0\},\{0;0\}$ $\{0;0\},\{0;-1\},\{0;0\},\{0;0\},\{0;0\},\{0;0\}$ $\{0;0\},\{0;0\},\{0;-1\},\{0;0\},\{0;0\},\{0;0\}$ $\{0;0\},\{0;0\},\{0;0\},\{0;-1\},\{0;0\},\{0;0\}$ $\{0;0\},\{0;0\},\{0;0\},\{0;0\},\{0;-1\},\{0;0\}$ $\{0;0\},\{0;0\},\{0;0\},\{0;0\},\{0;0\},\{0;-1\}$

Initial values

Subdomain initial value	3
FCOs	FCOso
FCO2s	FCO2so
FH2s	FH2so
FH2Os	FH2Oso
FArs	FArso
FN2s	FN2so

Application mode: PDE, Diffusion (chdi)

- Application mode type: Diffusion (Chemical Engineering Module)
- Application mode name: chdi

Property	Value
Default element type	Lagrange - Quadratic
Wave extension	Off
Frame	Frame (ref)
Weak constraints	Off

Variables

- Dependent variables: cCO, cCO2, cH2, cH2O, cAr, cN2
- Shape functions: shlag(2,'cCO'), shlag(2,'cCO2'), shlag(2,'cH2'), shlag(2,'cH2O'), shlag(2,'cAr'), shlag(2,'cN2')
- Interior boundaries not active

Boundary Settings

Boundary	5, 6	7	4
Type	Insulation/Symmetry	Flux	Flux
Inward flux (N)	{0;0;0;0;0;0}	$has*(pCOs-pCO)$; $has*(pCO2s-pCO2)$; $has*(pH2s-pH2)$; $has*(pH2Os-pH2O)$; $has*(pArs-pAr)$; $has*(pN2s-pN2)$	{$haf*(pCOf-pCO)$; $haf*(pCO2f-pCO2)$; $haf*(pH2f-pH2)$; $haf*(pH2Of-pH2O)$; $haf*(pArf-pAr)$; $haf*(pN2f-pN2)$

Subdomain Settings

Subdomain		2
Diffusion coefficient (c)	m^2/s	{DCOk;DCO2k;DH2k;DH2Ok;DArk;DN2k}
Source term (f)	$mol/m^3.s$	{-rate;rate;rate;-rate;0;0}

Initial values

Subdomain initial value		2
Concentration, cCO (cCO)	mol/m^3	FCOso
Concentration, cCO2 (cCO2)	mol/m^3	FCO2so
Concentration, cH2 (cH2)	mol/m^3	FH2so
Concentration, cH2O (cH2O)	mol/m^3	FH2Oso
Concentration, cAr (cAr)	mol/m^3	FArso
Concentration, cN2 (cN2)	mol/m^3	FN2so

Solver settings

Auto select solver	On
Solver	Stationary
Solution form	Automatic
Symmetric	auto
Adaptive mesh refinement	Off
Optimization/Sensitivity	Off
Plot while solving	Off

Direct (UMFPACK)

- Solver type: Linear system solver

Parameter	Value
Pivot threshold	0.1
Memory allocation factor	0.7

Stationary

Parameter	Value
Linearity	Automatic
Relative tolerance	1.0E-6
Maximum number of iterations	50
Manual tuning of damping parameters	Off
Highly nonlinear problem	Off
Initial damping factor	1.0
Minimum damping factor	1e-4
Restriction for step size update	10.0
Augmentation components	
Augmentation tolerance	0.001
Maximum number of augmented iterations	50
Augmented solver	UMFPACK

Advanced

Parameter	Value
Constraint handling method	Elimination
Null-space function	Automatic
Automatic assembly block size	On
Assembly block size	1000
Use Hermitian transpose of constraint matrix and in symmetry detection	Off
Use complex functions with real input	Off
Stop if error due to undefined operation	On
Store solution on file	Off
Type of scaling	Automatic
Manual scaling	
Row equilibration	On
Manual control of reassembly	On
Load constant	On
Constraint constant	On
Mass constant	On
Damping (mass) constant	On
Jacobian constant	On
Constraint Jacobian constant	On

Postprocessing

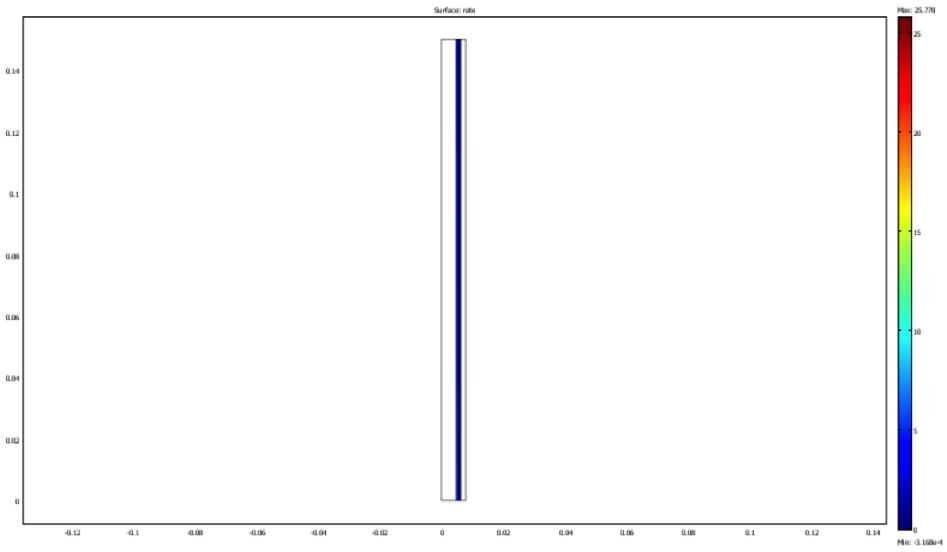

Benchmark

All simulations were carried out on a Dell Precision WorkStation T7500 with Intel Xeon CPU X5670 @2.93GHz equipped with 24GB of RAM, with a typical solution time of 1200 seconds.